Investigating Charge Order in $Pb_3Rh_7O_{15}$

by

Monika Azmanska

Submitted to the Department of Physics and Astronomy
in partial fulfillment of the requirements for the degree of

MASTER OF SCIENCE IN PHYSICS

at

MCMASTER UNIVERSITY

December 2024

Authored by:	Monika Azmanska Department of Physics and Astronomy December 6th, 2024
Certified by:	Patrick Clancy Assistant Professor, Thesis Supervisor Department of Physics and Astronomy
Accepted by:	School of Graduate Studies McMaster University

Investigating Charge Order in $Pb_3Rh_7O_{15}$

by

Monika Azmanska

Submitted to the Department of Physics and Astronomy
on December 6th, 2024 in partial fulfillment of the requirements for the degree of

MASTER OF SCIENCE IN PHYSICS

ABSTRACT

$Pb_3Rh_7O_{15}$ is a mixed-valent compound containing both Rh^{3+} and Rh^{4+} cations. This material undergoes a conductor-to-insulator transition at approximately 180 K. It is considered the first $4d$ transition metal compound to potentially exhibit a Verwey transition. Above the transition temperature, the Rh^{3+} and Rh^{4+} cations are expected to have an equal probability of occupying the same crystallographic site in the structure, resulting in conducting behaviour. Below this characteristic temperature, it is believed that these cations separate and arrange in a specific charge ordering scheme, causing the resistivity to increase abruptly. Despite the high-temperature structure of $Pb_3Rh_7O_{15}$ being reported in 1978, its low-temperature structure remains unsolved. In this work, we investigate whether charge order is indeed the driving mechanism of this transition.

We begin with reviewing essential background theory on metal-to-insulator transitions and transition metal oxides. We then identify the experimental signatures of charge order observed in other Verwey compounds. After establishing previously reported characterizations of $Pb_3Rh_7O_{15}$, we present our own temperature-dependent comparisons of the average crystal structure obtained via single crystal X-ray diffraction (XRD) refinement, which we use for subsequent symmetry and bond valence sum (BVS) analyses. We then investigate the local structural environment of the Rh cations and their short-range correlations through the search for diffuse scattering, by means of reciprocal space viewing of single crystal diffraction measurements, as well as synchrotron-based techniques such as High Dynamic Range Reciprocal Space Mapping (HDRM) and 3D-Δ PDF analysis. Finally, we consider the electronic environment of the Rh cations at different temperatures using X-ray absorption spectroscopy (XAS) and FDMNES modeling. Across all analyses, the results consistently show no evidence of charge order.

Thesis supervisor: Patrick Clancy
Title: Assistant Professor
Department: Department of Physics and Astronomy

Acknowledgments

This thesis would not exist without the invaluable contributions of numerous remarkable individuals, whom I would like to personally acknowledge. First and foremost, I would like to thank my supervisor, Pat Clancy, for his unwavering guidance and support throughout every stage of my Master's degree. I am grateful for the privilege of learning from your knowledge and experience. Thank you for believing in my abilities and for providing me with the opportunity to grow as an experimentalist. I would like to thank the instrument scientists responsible for my experiments - Suchismita Sarker, Chris Pollock, and Jim Britten (who came out of retirement to train me). Thank you for supporting me and our experimental team with your expertise, for setting up my experiments and providing me with the foundation of this thesis. I would also like to thank the members of our experimental team - Yijia Zi, Daniel Dobrowolski, Aileen Shanzeela, Justine Meriel, and Sebastian Wright - for their hard work and patience. I truly appreciate your dedication to ensuring the success of my experiments. Additionally, I would like to acknowledge Victoria Jarvis and Ning Chen for sharing their advice and technical proficiency, which proved crucial during the data analysis stage. Thank you to the crystal grower, Jiaqiang Yan, for the beautiful $Pb_3Rh_7O_{15}$ crystals, which were used for all measurements described in this work. Finally, I would like to express my appreciation to the members of my emotional support system - my roommate Tina Podinić, who took care of me when I was sick and tired and writing, and my parents, Temenoujka Azmanska and Dimitre Azmanski, who have always inspired me and to whom I owe everything.

Contents

List of Figures

List of Tables

Chapter 1

Background Theory

This thesis examines the conductor-to-insulator transition in $Pb_3Rh_7O_{15}$ and its driving mechanism. To contextualize this topic, we begin with an overview of some background theory on metal-to-insulator transitions.

1.1 Band Theory: Fundamental Description of Metals and Insulators

Metals and insulators are primarily distinguished by the temperature dependence of their electrical resistivity ρ. For most metals, ρ increases with temperature, while for insulators, it decreases as temperature rises. Additionally, metals typically exhibit high electrical DC conductivity $\sigma = 1/\rho$, with pure metals like Cu reaching values on the order of $10^9\ \Omega^{-1}\ \mathrm{cm}^{-1}$ at liquid helium temperatures [1]. Meanwhile, insulators show significantly lower conductivity, on the order of $10^{-22}\ \Omega^{-1}\ \mathrm{cm}^{-1}$ [1] at the same temperature. Classically, high conductivity in metals arises from the presence of charge carriers, which are delocalized electrons within the system, while insulating properties result from the absence of such itinerant behaviour, as electrons are bound to the ionic cores.

An initial quantum description explaining this difference in behaviour was provided in the form of band theory (also known as Bloch theory), developed by Bethe and Sommerfeld in 1928 and Bloch in 1929 [2]. It states that in a crystal lattice, the periodic arrangement of atoms introduces a periodic potential (Bloch potential), giving rise to an electronic band structure that encompasses all electronic states of the system. The highest energy state occupied by the electrons is defined as the Fermi energy, ϵ_F. In this picture, metals have partially filled bands, and the Fermi energy ϵ_F lies within the highest occupied energy band. Therefore, there are available states close to the Fermi energy which electrons can access by gaining a small amount of kinetic energy. As a result, electrons are free to move within the band, allowing for electrical conduction. On the other hand, insulators have filled electronic bands and the Fermi level is located in the energy band gap between the valence and conduction bands [3]. Under these conditions, thermal excitations do not supply enough energy for electrons to overcome the band gap. Electrons do not have access to other states and cannot move freely, leading to low electrical conductivity in the system. Materials that follow this model are known as "band insulators".

1.2 Breakdown of Band Theory

Band theory provides a solid preliminary description of standard metals and insulators; however, it has limitations that become apparent when considering certain materials exhibiting metal-to-insulator, or more generally conductor-to-insulator transitions. The theory does not account for the possibility of moving from one state to another when the energy gap between the valence and conduction bands is large, as this would require changes to the band structure of the system. Moreover, de Boer and Verwey [4] noted the existence of materials with partially filled bands that behaved as insulators, contradicting band theory predictions and adding to the argument for its incompleteness.

1.3 Metal to Insulator Transitions

A metal-to-insulator transition (MIT) occurs when a material shifts from metallic to insulating behaviour as a specific parameter is tuned. Conductor-to-insulator transitions refer to phenomena where the high temperature phase presents conducting behaviour, without necessarily being fully metallic, encompassing metals, semi-metals and semiconductors. Since the basic mechanisms driving metal-to-insulator transitions are also applicable to conductor-to-insulator transitions, we focus on metal-to-insulator transitions in this section. Many models have been proposed based on the diverse mechanisms and competing interactions observed to drive this type of transition [1]. MITs can be categorized by effects on structural properties (such as the presence or absence of symmetry breaking), spin and orbital degrees of freedom, dimensionality, and nature of transition (first or second order) [2].

The only type of metal-to-insulator transition permitted by band theory involves insulators with small energy band gaps, also known as semiconductors. In this case, thermal excitations can provide enough energy for electrons in the valence band near the Fermi energy to cross the band gap and move to the conduction band [2]. Once promoted, electrons gain access to more states and become mobile within the band, causing a metal-to-insulator transition in the material without a change in band structure.

Most types of MITs exhibit an opening of a band gap, and thus a change in band structure, which can arise from the emergence of long-range order in moments, observed in Mott-Heisenberg insulators, or from a quantum phase transition originating from charge or spin correlations, which is the case for Mott-Hubbard and charge transfer insulators [3]. In the following subsections, we review theoretical models that consider these more complex MITs, which lie beyond the scope of classical band theory.

1.3.1 Non-Interacting Models

MITs have attracted considerable interest since the early 20th century. Initial attempts to explain these transitions were based on non-interacting systems, treating electrons as independent of one another. These models provided only partial descriptions of MITs, as they first approached the transition in only one direction— from insulator to metal.

In 1927, Goldhammer and Herzfeld hypothesized a liquid-to-metal phase transition in hydrogen when subjected to high temperature and pressure. This insulator-to-metal transition was described as a 'density-induced transition' [4]. In the Claussius-Mossoti equation, which relates the polarizability and index of refraction of an element, given by $(n^2-1)/(n^2+2) = R/V$, where n is the index of refraction, R is the molar refractivity and V is the molar volume, the ratio R/V increases during the transition from liquid to solid phase until it reaches the value 1. In this limit, $(n^2-1) = (n^2+2)$, and the dielectric constant n diverges to infinity, which is deemed the 'polarization or dielectric catastrophe'. The valence electrons are 'freed' from the ionic cores, introducing mobile charge carriers into the system and resulting in high electrical conductivity. Therefore, if the ratio R/V of a chemical element is close to 1, the theory predicts metallic behaviour: this is defined as the "Herzfeld criterion". In 1983, Pauling [4] expanded on this model by showing that R^{-3} corresponds to the approximate radius of the valence electrons. Therefore, when $R \approx V$, the outer electron orbitals overlap and form covalent bonds.

The index of refraction n is related to the dielectric constant ε by $n^2 = \varepsilon$, the molar refractivity is given by $R = (4\pi N_A \alpha)/3$, where N_A is Avogadro's number, α is the polarizability, and the volume V per mole can be written as $V = N_A/N$, where N is the number density. Using these relations, the Clausius-Mossotti equation can be rewritten as $(\varepsilon - 1)/(\varepsilon + 2) = (4\pi N\alpha)/3$. For the critical density $N_c = 3/(4\pi\alpha)$, the dielectric constant ε diverges to infinity. Given that the Coulomb potential is related to the dielectric constant by $V(r) = -e^2/(\varepsilon r)$, $V(r)$ approaches zero as ε diverges. Mott coined this phenomenon as the "polarization catastrophe of carrier density" [4]: as material density increases, so does electron density, which screens out the Coulomb potential and causes it to approach zero. The highest energy bound electrons are freed and the system undergoes an insulator-to-metal transition. Mott proposed that the critical distance for these screening effects can be expressed through electron density, defined by the Mott criterion $N_c^{1/3} a_H^* \approx 0.25$, where a_H^* is the Bohr radius of the electron.

Building on this picture, the transition from metal to insulator was later considered. In this scenario, the material begins in a conducting state. As the electron carrier density decreases, the Thomas-Fermi screening of the Coulomb potential becomes insufficient, leading to electron localization at the same critical carrier density, N_c.

In 1958, Anderson [4] proposed that the metal-to-insulator transition is an order-disorder transition, offering a different mechanism for the phenomenon. Disorder creates irregularities in the crystal potential, which can prevent itinerant electrons from moving freely. Within the band, the conducting and localized electronic states are separated by a threshold energy defined as the mobility edge. As disorder increases, the mobility edge shifts closer to the Fermi energy. If the mobility edge crosses the Fermi energy, all accessible states become localized and no longer contribute to conductivity, resulting in a metal-to-insulator transition.

1.3.2 Electron-Electron Correlation Models

The independent electron model falls short when considering more complicated chemical elements; electron correlations must be included.

Electron interactions that can drive a metal-to-insulator transition fall into three main categories: electron-lattice, spin-orbit coupling, and electron-electron. Electron-lattice correlations refer to changes in the crystal lattice structure, such as site periodicity in Peierls insulators [5], which alter the electronic band structure and lead to the opening of an energy band gap. Spin-orbit coupling [6] describes the interaction between an electron's spin and the magnetic field created by its orbital motion. This type of interaction is found to be significant in heavier transition metals, such as in $5d$ materials, where the spin-orbit coupling can cause the splitting of d levels, thus introducing an energy band gap, such as in spin-orbital Mott insulators. Electron-electron interactions refer to the Coulomb repulsion between electrons and can be grouped in intrasite and intersite subtypes.

Mott argued that intrasite, or on-site, electron-electron correlation effects should be considered when two electrons with opposite spins occupy the same atomic orbital, as they experience Coulomb repulsion that depends on the spatial extent of the orbitals [2]. Revisiting the hydrogen example, Mott also highlighted the significance of intersite electron-electron correlations [3], which describe the Coulomb interactions between electrons at different sites. Here, he considered a lattice of atoms arranged in a 1D array. If the interatomic distances are small, the electron tunneling probability increases, resulting in metallic behaviour. Since the electrons move fast, the Coulomb interaction U between them is averaged and the Hartree-Fock approximation can be applied. Therefore, the electronic states are represented by products of single electron wavefunctions that are symmetric under electron exchange. Assuming each energy level is nondegenerate, a lattice with N sites will have N electronic states per band. According to the Pauli exclusion principle, each state can hold two electrons (one spin-up and one spin-down) and thus each band can accommodate 2N electrons. Since hydrogen has one electron (an odd number), each site will contain one electron, resulting in a half-filled band. If the distances between the lattice sites are increased, the electronic bandwidths become narrower and, the density of states (DOS) for each site increases as well. Mott noted that for a critical electron bandwidth, the Coulomb interaction can no longer be averaged and the electrons become bound to the closest site, leading to a metal-to-insulator transition. In the zero bandwidth limit, electrons are no longer described by extended Bloch wavefunctions but instead by localized atomic wavefunctions [4]. In this framework, intersite electron-electron repulsion, which promotes electron localization, competes with the kinetic energy that drives electron delocalization across the lattice.

It is proposed that the most relevant electron correlations in the material studied in this thesis are electron-electron interactions [7]. In the following subsections, we discuss Mott-Hubbard and charge transfer insulators, driven by intrasite and intersite electron-electron correlations, respectively.

Mott-Hubbard Insulators

In 1963, Hubbard discovered insulating rather than conducting behaviour in materials with partially filled bands, such as NiO and $LaCuO_4$ [4]. This led him to define the on-site (or intrasite) Coulomb interaction U for narrow-band systems, representing the energy cost of placing two electrons on a single atomic site [3]. This term is now known as the Mott-Hubbard correlation energy, given by $U = I - EA$, where I is the intra-atomic ionization energy, and EA is the electron affinity, corresponding to the energy required, respectively, to remove or add an electron to the orbital. In this model, U/t denotes the electron correlation strength, with t the hopping or kinetic term which indicates the probability of tunneling to neighbouring sites. When the ratio $U/t < 1$, the kinetic term t dominates, thus promoting electron intersite hopping. This is typically the case for crystal lattices with small lattice constants, since the intersite distances are small enough for the orbitals to overlap. This results in the broadening of the electron bandwidth W, allowing for electrons to spread across the lattice, and thus resulting in conductive behaviour. When $U/t > 1$, typical for materials with larger lattice constants, the on-site electron-electron interaction U dominates, leading to insulating behaviour. Here, the interaction U causes the partially filled band to split into a lower and upper Hubbard band. The lower Hubbard band (LH) describes individual, unpaired electrons, whereas the upper Hubbard band (UH) corresponds to paired electrons, where each pair is formed by one spin-up and one spin-down electron. The UH band is higher in energy than the LH band, as it requires more energy to place two electrons on the same site due to Coulomb repulsion. The system exhibits insulating behaviour because of the energy band gap between the upper and lower Hubbard bands: this scenario is known as the Mott-Hubbard insulator, shown in Fig. 1.1.

Charge Transfer Insulators

To reiterate, in Mott-Hubbard insulators, the band gap arises from the splitting of the partially filled d-band into an upper and lower Hubbard band, caused by Coulomb interactions between electrons occupying the same site. This model does not account for the presence of ligand atoms, which are important in systems like transition metal oxides. In 1985, Zaanen et al. [8] introduced the concept of the charge transfer (CT) insulator - a new type of insulator describing compounds where the metal-to-insulator transition is primarily driven by intersite electron-electron interactions.

In these materials, p-bands from ligand atoms, such as oxygen, must be considered. Denoting the p_σ energy level as ε_p and the center of the metal d-orbital energy level as ε_d, the parameter $\Delta = |\varepsilon_d - \varepsilon_p|$ is defined as the "charge transfer energy". This quantity corresponds to the energy needed to shift an electron from an oxygen p-band to an unoccupied metal d-band. If intrasite electron interactions are present as well, then comparing the energy scales of U and Δ helps determine whether the system behaves as a Mott-Hubbard or charge transfer insulator. If $U < \Delta$, then the energy difference between the oxygen p-band and the unoccupied metal d-band is greater than the band gap between the two Hubbard bands. Therefore, the system will be a Mott-Hubbard insulator. Conversely, if $U > \Delta$, then the oxygen p-band will lie between the two Hubbard d-bands. In this case, the minimum charge excitation gap will be the energy difference between the oxygen p-band and the upper Hubbard d-band. Therefore, the minimum charge excitation energy is given by the charge transfer energy Δ instead of the on-site Coulomb repulsion U, and the system will behave as a charge transfer insulator, as shown in the bottom half of Fig. 1.1.

Generally, transition metal oxides beyond FeO are classified as charge transfer insulators.

Comparison Between Mott-Hubbard and Charge Transfer Insulators.

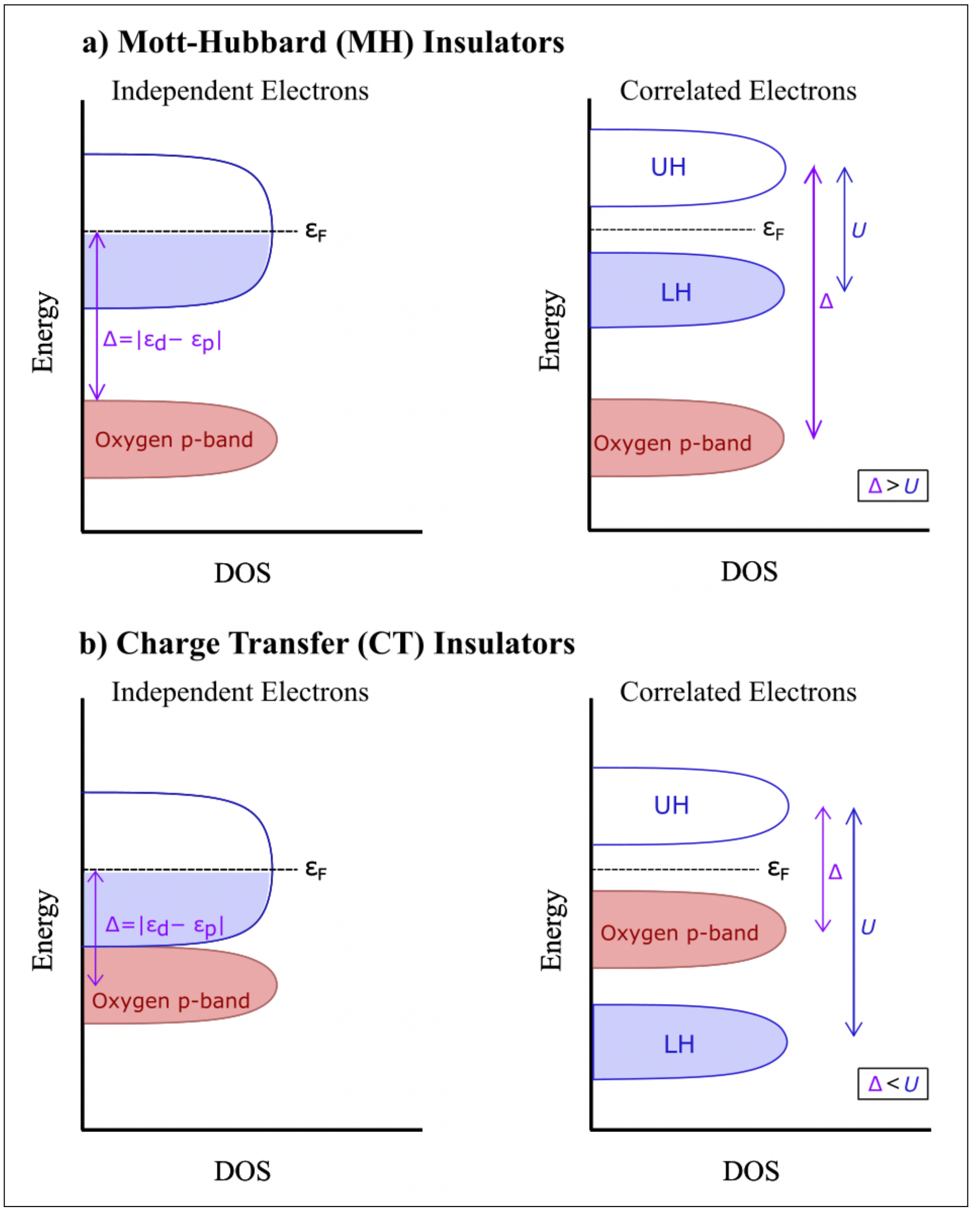

Figure 1.1: When the Hubbard energy is less than the charge transfer energy ($U < \Delta$), the bandgap is determined by the energy difference between the upper Hubbard band (UH) and the lower Hubbard band (LH), characteristic of a Mott-Hubbard insulator, as shown in (a). However, in a charge transfer insulator (b), the O p-bands lie in between the upper and lower Hubbard d bands, with $\Delta < U$. Thus, the bandgap is determined by the energy required to transfer an electron from the LH to p-band or p to UH band, depending on whether the Fermi level lies within or above the p-band.

1.4 Charge Order in Transition Metal Oxides

1.4.1 Transition Metal Oxides

Some of the most prominent examples of Mott-Hubbard and charge transfer insulators are found among the class of materials known as transition metal oxides, first brought to attention by de Boer and Verwey in 1937 [9]. They considered $3d$ metals with partially filled bands and noticed insulating, rather than metallic behaviour, contradicting predictions made by Bloch theory. Some examples of materials they studied included NiO, CoO, MnO, Fe_2O_3, Fe_3O_4, Mn_3O_4, and Co_3O_4.

In transition metal compounds, metal ions form covalent bonds with surrounding ligand atoms, such as oxygen in oxides or chlorine and bromine in halides, which increases the cohesive energy of the system. These negatively charged ligand atoms often arrange into octahedral or tetrahedral cages around the metal cations, creating an asymmetric electric field known as the crystal field. When only subjected to the spherical potential of the transition metal ion, the electron d eigenstates present fivefold orbital degeneracy, as the angular momentum of a d-type orbital is given by the quantum number $l = 2$, leading to 5 possible values for l_z: (2,1,0,-1,-2). In the presence of a crystal field, this fivefold degeneracy is lifted, causing the d-orbitals to split into two sets of energy levels: the e_g doublet, containing two orbitals, and the t_{2g} triplet, containing three orbitals [3]. The arrangement of these levels depends on the geometry of the crystal field: for a tetrahedral field, the t_{2g} levels are higher in energy, while for an octahedral field, the e_g levels are higher. Therefore, the crystal field shifts the d-orbital energy levels relative to each other and to the ligand p-bands, which affects the onsite Coulomb interaction U and the charge transfer energy Δ. If the crystal field shifts the d-levels such that the energy gap between the resulting upper and lower Hubbard bands is smaller than the gap between the metal d-bands and ligand p-bands, then $U < \Delta$ and the energy gap is determined by U. The system exhibits Mott-Hubbard type behaviour, since the electron excitations are more likely to occur between the d-orbitals rather than between the d and p-orbitals. Conversely, if the crystal field places unoccupied t_{2g} or e_g levels closer to the p-orbitals, thus reducing the energy gap between the p and d-bands, the likelihood of $\Delta < U$ increases. In this case, the energy required to promote an electron from an oxygen p-orbital to a metal d-orbital is lower than the energy required to overcome the repulsion between two electrons at the same site. Therefore, it would be energetically more favourable to open a hole in the oxygen p-band than to add an electron to upper Hubbard metal d-band, resulting in charge transfer behaviour of the system.

Mott-Hubbard insulating behaviour tends to be more common in earlier $3d$ transition metal oxides, such as in compounds involving Ti, V and Cr [10]. The insulating nature of these materials arises from the strong intrasite electron-electron repulsion within the partially filled d-orbitals. In $4d$ and $3d$ transition metal oxides beyond FeO, charge transfer insulating behaviour becomes more prevalent [11]. In these materials, the spatial overlap between the metal d and ligand p-orbitals is increased due to the larger spatial extent of the d-orbitals. This promotes stronger hybridization between the metal d and oxygen p-orbitals, resulting in a smaller charge transfer energy Δ relative to the Coulomb repulsion U. Another important factor influencing p-d hybridization is the electron occupancy of the d-orbitals, particularly whether the Fermi energy lies within the t_{2g} or e_g levels [2].

Examples of Interactions Between d and p-type Orbitals.

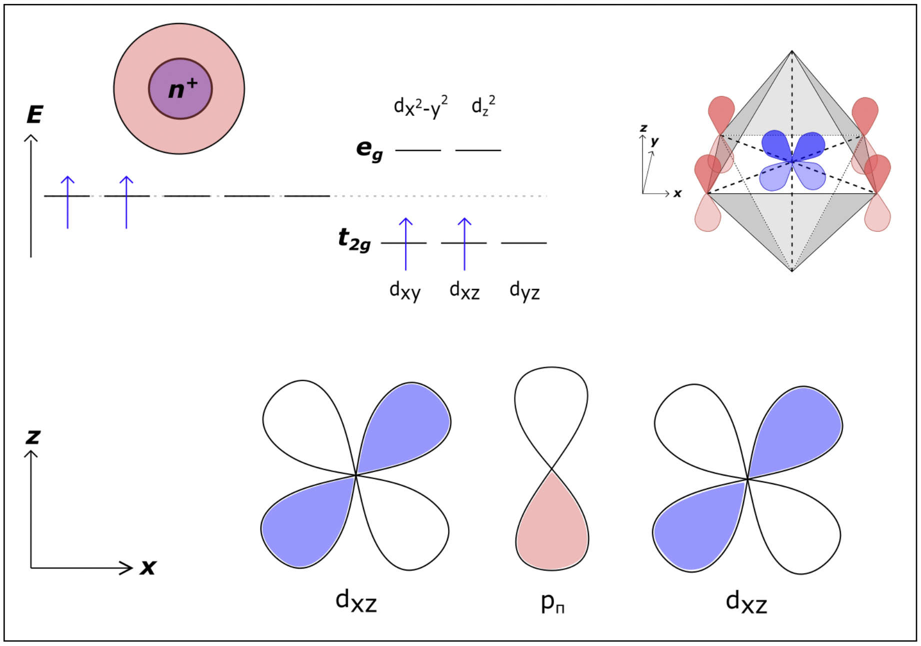

(a) Interaction between t_{2g} d-orbital and ligand p_{π} orbitals.

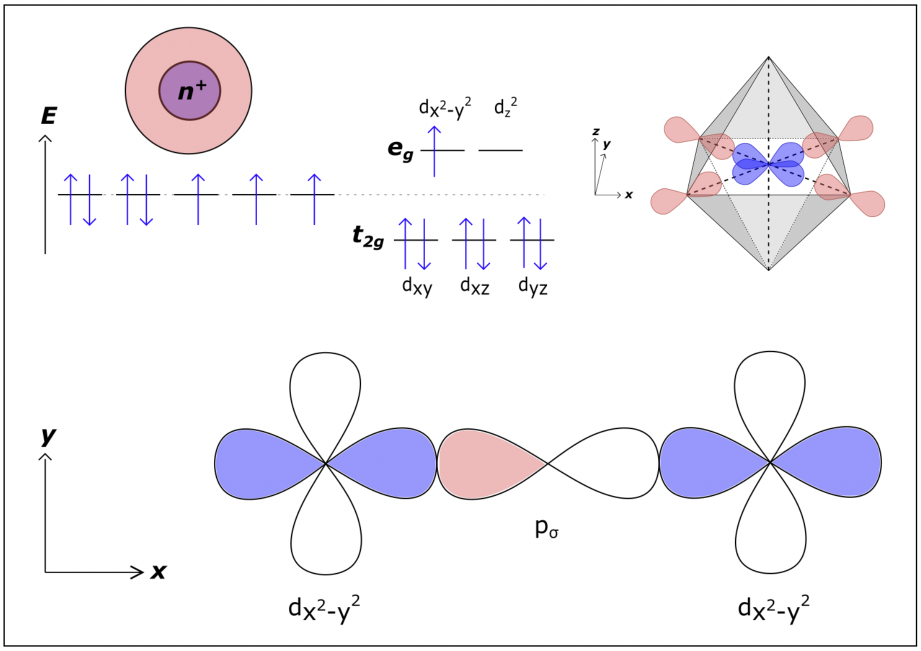

(b) Interaction between e_g d-orbital and ligand p_{σ} orbitals.

Figure 1.2: In the upper half of both images, the metal cation n^+ is surrounded by a uniformly distributed charge over the surface of a sphere, leading to five degenerate d-orbitals. In the presence of a crystal field, the d-orbitals split into two e_g and three t_{2g} orbitals. When this crystal field is formed by an octahedral arrangement of negative charges, the e_g orbitals are higher in energy than the t_{2g} orbitals. Spins are depicted as arrows, representing the occupied states according to Hund's rules.

Let's consider the scenario where the metal cations are surrounded by an octahedral crystal field, as illustrated in Fig. 1.2. If the Fermi energy lies within the t_{2g} levels, then the next unoccupied d-orbitals will also have t_{2g} symmetry. The spatial orientation of the t_{2g} d-orbitals is such that their lobes point between the axes of the octahedra formed by the crystal field. In this configuration, the distance between the metal d and oxygen p-orbital lobes is large. This leads to weak p-d hybridization, favouring Mott-Hubbard insulating behaviour. On the other hand, if the Fermi energy is located above the t_{2g} orbitals, then the next unoccupied d-orbital will be of e_g type. The lobes of the e_g d-orbitals align directly along the crystal field axes, pointing toward the ligands. In this configuration, the e_g and p_σ-orbitals overlap, leading to strong p-d hybridization. As a result, the charge transfer energy Δ is lowered, thus promoting charge transfer insulator behaviour.

1.4.2 Fe_3O_4 and the Verwey Transition

In this section we introduce charge order (CO), a common driving mechanism for metal-to-insulator transitions in mixed-valent transition metal oxides. This mechanism combines aspects of both Mott-Hubbard and charge transfer insulating behaviours, as the mixed-valent nature of these materials results in the presence of both strong intrasite electron-electron correlations and a small charge transfer energy Δ due to hybridization between metal d and oxygen p-orbitals.

Charge order was first discovered in magnetite (Fe_3O_4) by Verwey and Haayman in 1941 [12], who proposed an initial model for its insulating state. However, it was not until 2012 that the true ground state of the insulating phase was established by Senn, Wright and Attfield [13].

Verwey's Model

In 1926, Parks and Kelley [4] reported a metal-to-insulator transition in Fe_3O_4 when they observed a discontinuity at $T_V = 120$ K in heat capacity C_V, indicative of a phase transition. In 1939, Verwey found that Fe_3O_4 also exhibited a sudden two-order-of-magnitude drop in electrical conductivity σ at the same characteristic temperature T_V upon cooling from high to low temperature [2]. Two years later, he proposed a model describing the insulating behavior of the system below T_V, introducing the concept of "charge ordering."

Fe_3O_4 has a spinel structure, defined by the general formula AB_2O_4, where the oxygen atoms are arranged in an FCC lattice containing numerous interstitial sites, partially occupied by A and B metal ions. In this structure, there are two inequivalent Fe crystalline sites, consisting of an A and B-site and represented in Fig. 1.3, where Fe cations are tetrahedrally and octahedrally coordinated, respectively, with surrounding oxygen ligands. One-third of the Fe sites are of the A type, with the remaining two-thirds being of the B type. Above the transition temperature T_V, the A-site ions have a nominal valence of Fe^{3+}, while B-site ions are mixed valence with a 1:1 ratio of Fe^{3+} and Fe^{2+} ions. Band structure calculations predict a quarter filled conduction band for the metal Fe ions [3]. Verwey proposed that on the mixed-valent B site, Fe^{3+} and Fe^{2+} ions are dynamically disordered in the lattice. The motion of the electrons from the dynamical transformation of Fe^{2+} into Fe^{3+} is responsible for the high conductivity of Fe_3O_4 above T_V.

Fe_3O_4 **Crystal Structure [14].**

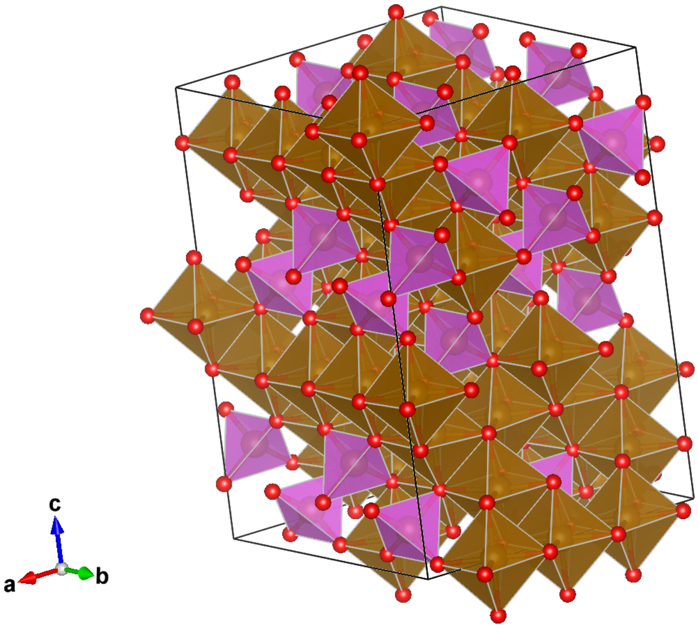

Figure 1.3: A sites are represented by pink tetrahedra, and B sites by orange octahedra. Fe cations occupy both A sites (all Fe^{3+}) and B sites (mixed Fe^{2+} and Fe^{3+}) in this structure. Charge ordering is expected on the 16 inequivalent B sites.

Below T_V, the Fe^{3+} and Fe^{2+} ions order periodically across the lattice, which localizes the electrons involved in the aforementioned dynamical processes [4]. This transition is accompanied by a structural distortion: to accommodate the subsequent lowering of symmetry of the system, the space group of the Fe_3O_4 structure changes from cubic to orthorhombic. The Fe ions arrange in a complex charge-ordering scheme, generally described by the tendency of Fe^{3+} and Fe^{2+} ions to alternately occupy (001) planes, forming chains of same-valence ions along the [110] and [-110] directions, as seen in Fig. 1.4a. In 1956, Anderson noted the high and nonmetallic nature of magnetite's electrical resistivity ρ above T_V until 300 K, with $\rho < 10^{-2}\Omega$ cm and $d\rho/dT < 0$. He attributed this to short-range order, introducing an additional condition to Verwey's model [4]. He argued that in the Fe_3O_4 structure, the Fe ions should be arranged such that two Fe^{2+} and two Fe^{3+} ions form a Fe_4 tetrahedron. When the system goes through the transition, the total charge of this tetrahedron should be conserved.

The new low temperature orthorhombic structure would cause an (002) reflection, otherwise forbidden in the high temperature cubic phase. This was supposedly confirmed by neutron diffraction experiments performed by Hamilton in 1958, which served as experimental evidence to validate the classical Verwey model. However, Shirane et al. later showed that this signal was, in fact, a spurious artifact caused by multiple scattering effects [4]. The results of this study raised questions about the accuracy of the classical Verwey model, thus challenging the overall understanding of the metal-to-insulator transition in Fe_3O_4.

Trimeron Order

The low-temperature ground state of Fe_3O_4 was finally determined, 70 years after Verwey's initial proposal, by Senn, Wright, and Attfield through a comprehensive bond-length analysis [13]. In their study, they extracted characteristic intersite distances by comparing the amplitudes of distortions present in each of the 16 inequivalent B-site FeO_6 octahedra. The two types of distortions chosen for this analysis due to their sensitivity to charge and orbital ordering displacements, were the breathing modes Q_{Rad} and the Jahn-Teller tetragonal distortion Q_{JT}.

The edge sharing geometry of the FeO_6 octahedra allows for direct electronic interactions between the B-sites in 6 distinct directions. In the high-temperature cubic phase, the distances between Fe^{2+} and Fe^{3+} ions located on nearest-neighbor B-sites, denoted $D_{BB}(Fe^{2+}\text{-}Fe^{3+})$, are all equivalent. However, this is not the case in the low-temperature phase, as this distance shows a broad distribution of values throughout the lattice. Electrostatic forces cause electrons in Fe^{2+} to be less tightly bound, resulting in a larger radius, while Fe^{3+} electrons are more tightly bound, resulting in a smaller radius. Therefore, Fe interionic distances are expected to follow the relationship $D_{BB}(Fe^{2+}\text{-}Fe^{2+}) < D_{BB}(Fe^{2+}\text{-}Fe^{3+}) < D_{BB}(Fe^{3+}\text{-}Fe^{3+})$. However, several $D_{BB}(Fe^{2+}\text{-}Fe^{3+})$ distances were found to be shorter than the separation between two Fe^{2+} cations, $D_{BB}(Fe^{2+}\text{-}Fe^{2+})$. The anomalous shortening of these distances suggests the presence of a linear three-site distortion involving $Fe^{3+}-Fe^{2+}-Fe^{3+}$ sites. It was found that the minority-spin t_{2g} electron density from the Fe^{2+} site is significantly delocalized across two adjacent B-site acceptors, typically Fe^{3+} sites. A single charge is therefore delocalized over 3 B-sites, as shown in Fig. 1.4b. The resulting displacements of the acceptor B-sites and surrounding ligands creates a small polaron, called 'trimeron'. These trimerons are ordered along infinite B chains, forming charge density waves defined by the wavevector $q_c = 1/N$. Under these conditions, Anderson's rule stating that each Fe_4 tetrahedron of four neighbouring B-sites should contain two Fe^{2+} and two Fe^{3+}ions is only satisfied for a quarter of the tetrahedra. In this model, although the electron density across the three trimeron sites appears to be uniform, the low-temperature phase can still be classified as a 'charge ordered structure' because the orbitals retain the geometry and occupancies associated with the nominal valence of the B-site, with $d_{xy}^{0.6}d_{xz}^{0}d_{yz}^{0}$ for Fe^{2+} and $d_{xy}^{0.2}d_{xz}^{0.2}d_{yz}^{0.2}$ for Fe^{3+}.

Thus, the classical "charge order" model proposed by Verwey, suggesting a fully ordered low-temperature phase with integer valence Fe B-sites, has not been observed. The condition is relaxed, redefining 'charge order' as charge localization due to some form of spatial ordering of different valence states as the driving mechanism for a metal-to-insulator transition.

Fe_3O_4 **Charge Ordering Schemes [15].**

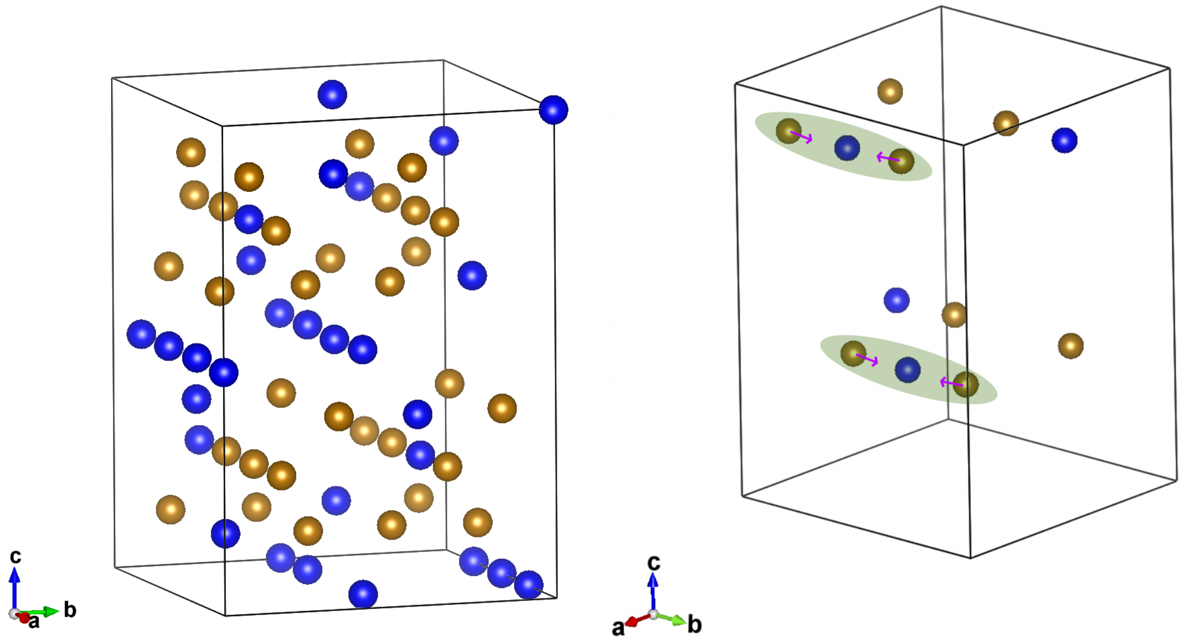

(a) (b)

Figure 1.4: a) Example of a classical (Verwey) charge ordering scheme in Fe_3O_4: Fe^{2+} (blue) and Fe^{3+} (yellow) cations are fully separated, only Fe B-sites are shown for clarity. b) Depiction of two trimeron units (green) and associated atomic displacements (purple arrows), due to electron delocalization over three Fe sites.

Chapter 2

Experimental Investigations of Charge Order

After reviewing key theoretical concepts behind charge order and metal-to-insulator transitions in the previous sections, the following chapter will focus on experimental techniques and indicators used to identify charge order.

2.1 Macroscopic Properties

We now review the primary bulk properties of metals and insulators, followed by reported bulk properties in compounds known to exhibit charge order, commonly referred to as Verwey compounds.

2.1.1 Characteristics of Metals and Insulators

In this subsection, we list several standard macroscopic properties and discuss how they vary between metals and insulators.

We begin with resistivity ρ, often the first quantity measured when studying materials presenting metal-to-insulator transitions. For most pure metals, ρ decreases linearly and monotonically with increasing temperature. At low temperatures, ρ reaches a constant value, known as the residual resistivity ρ_0, dependent only on lattice impurities. As temperature increases, atoms in the lattice vibrate more intensely, leading to more frequent collisions with free electrons. This interaction, known as electron-phonon scattering, results in loss of kinetic energy for the free electrons. In metals, the electrical resistivity is proportional to the magnitude of phonon scattering. Therefore, pure metals have positive temperature coefficients of resistivity. In contrast, insulators tend to have high resistivity values and remain relatively invariant with temperature. In semiconductors, as temperature increases, the localized electrons gain kinetic energy and break their bonds. Therefore, in these materials, resistivity decreases and conductivity increases as temperature rises, resulting in a negative temperature coefficient of resistivity [16].

The Hall Resistivity R_H corresponds to the measure of the transverse voltage generated when an electric current flows through a material in the presence of a perpendicular magnetic field. R_H is inversely proportional to the charge carrier density and the charge mobility. Metals exhibit generally higher carrier densities, leading to low Hall resistivity R_H values. Conversely, the low carrier density in insulators gives high, or in some cases, diverging R_H resistivity, due to the absence of free carriers at low temperatures [17].

Heat capacity $C(T)$ corresponds to the energy required to raise the temperature of a given quantity of material by one degree. In pure metals, specific heat is linearly proportional to temperature below $T \approx 10$ K, then follows a T^3 dependence up to approximately 100 K, and approaches a nearly constant value above this region. In insulators, phonons always dominate; specific heat presents a cubic temperature dependence at low temperatures, whereas at high temperatures, it approaches the classical Dulong-Petit limit, reaching a constant value C_{ph} [18].

The Seebeck coefficient $S(T)$, also known as thermopower, is a measure of voltage generated per unit temperature difference. Microscopically, this corresponds to the entropy carried per unit charge carrier. The sign of the coefficient gives information about the type of carrier responsible for conduction in the material. This is especially useful for understanding semiconductor systems. A negative sign is associated with n-type carriers (excess of electrons), while a positive sign is characteristic of p-type materials (excess of holes). The Seebeck coefficient is inversely proportional to the carrier concentration. In pure metals, $S(T)$ is typically on the order of μV/K, following a cubic temperature dependence at low temperatures and a linear dependence at higher temperatures. Due to low carrier concentrations in insulators, $S(T)$ is generally several orders of magnitude higher than in metals and exhibits a more complex behaviour [19].

Magnetic susceptibility $\chi(T)$ measures the response of magnetic moments present in a material to an applied external magnetic field. In pure metals, free electrons exhibit a Pauli paramagnetic response to the field, resulting in weak, temperature-independent magnetic susceptibility. In insulators, $\chi(T)$ is dominated by localized magnetic moments which give stronger temperature dependence. In the presence of independent magnetic moments, $\chi(T)$ is inversely proportional to temperature and follows the Curie law given by $\chi = C/T$, where C is the Curie constant and T is absolute temperature. If there is strong interaction between magnetic moments in the system, then $\chi(T)$ follows the Curie-Weiss law, described by $\chi = C/(T - \theta)$, where the Weiss constant θ accounts for the strength of the interaction between magnetic moments.

2.1.2 Bulk Characterization Applied to Verwey Compounds

We now discuss commonly observed features in resistivity, heat capacity, magnetic susceptibility, and thermopower in charge-ordered compounds through examples of reported Verwey materials. These bulk techniques are useful for identifying the presence an electronic transition, even if direct probing is still required to establish charge order.

We begin with magnetite Fe_3O_4, which we discussed in the previous chapter for being central to the concept of charge ordering. Heat capacity measurements show a λ-shape anomaly at the phase transition temperature, $T_V \approx 120$K [20]. Fe_3O_4 has a resistivity, $\rho(T) \approx 4$ mΩcm at room temperature, and shows a sharp discontinuity in $\rho(T)$ at the Verwey transition temperature [4]. Although this transition is commonly referred to as a metal-to-insulator transition, in reality $d\rho/dT < 0$ both above and below the transition temperature [21]. Therefore, it would be more accurately described as a conductor-to-insulator transition instead, which is how we define the Verwey transition for the purpose of this study.

The next material of interest is Fe_5O_6, which differs from Fe_3O_4 in both space group and Fe nominal valence: Fe_3O_4 is cubic, presenting a nominal oxidation state of $Fe^{2.67+}$, while Fe_5O_6 is orthorhombic with a $Fe^{2.4+}$ nominal valence. Fe_5O_6 presents an abrupt increase in resistivity below 280 – 290 K, with room temperature values of $\rho(T)$ ≈7 mΩc. Magnetic susceptibility $\chi(T)$ measurements show a distinct minimum at around T≈ 270 K. Heat capacity $c(T)$ shows an increase below 270 K, suggesting the emergence of magnetic moments in the material. Magnetic susceptibility exhibits non-linear behaviour, thus deviating from the expected Curie-Weiss model [22].

Charge order-driven metal-to-insulator transitions have been reported in rare earth (R) perovskite nickelates, with transition temperatures T_V depending on the selected rare earth cations - for an element with a smaller ionic radius, the transition temperature is higher. In these compounds, T_V can be tuned ranging from a fully metallic state at all temperatures for $R =$ La, to values comparable to the transition temperature of Fe_3O_4 at $T_V = 120$ K for $R =$ Pr, to full suppression of the metallic phase for a fully insulating state at all temperatures for $R =$ Lu. The highest transition temperature displayed by these perovskites was observed for $R =$ Eu, with $T_V = 480$ K. In these materials, resistivity shows a sharp several-orders-of-magnitude increase when going from high to low temperature [23].

$CuIr_2S_4$ is a compound that presents a metal-to-insulator transition at $T_V \approx 230$ K. This material shows an abrupt jump in resistivity, where $\rho(T)$ is on the order of 10^0 mΩcm above T_V, and 10^4mΩcm for temperatures below T_V. Additionally, the Seebeck coefficient $S(T)$ remains positive above and below the transition temperature, implying p-type charge carriers [24]. It displays a sharp increase, going from $S(T) \approx 10\ \mu V/\mathrm{K}$ at high temperatures to $S(T) \approx 80\ \mu V/\mathrm{K}$ below T_V. Above T_V, the thermopower behaviour is roughly proportional to temperature, while below T_V it follows a $T^{1.5}$ dependence.

All of the examples mentioned above present a discontinuous increase in the electrical resistivity $\rho(T)$ at the transition temperature T_V, often accompanied by some anomaly in other types of bulk measurements. When investigating charge order, initial analyses involve comparing the material's bulk properties with behaviour predicted by a proposed charge ordering model. However, this comparison can often be misleading, especially in cases where the material shows more complex charge localization schemes, such as stripe or polaron order. Therefore, while bulk property measurements are necessary for establishing the occurrence of a conductor-insulator transition in a material, they are not sufficient to prove the presence of charge order in the system and must be followed by additional diffraction or spectroscopy-based measurements.

2.2 Bond Valence Sums

One of the most common techniques used for identifying charge order is bond valence sum (BVS) analysis. BVS is a method that uses bond lengths between neighbouring atoms to estimate the valence of an ion in a molecule, and by extension, the oxidation state of a crystallographic site and the charge distribution within the lattice.

The theory behind BVS is based on the principle that the valence sum v_i of an ion should be equal to the sum of bond valences around it: $v_i = \sum_j v_{ij}$, where the bond valence is an effective measure of the bond order and strength. Individual bond valences are given by $v_{ij} = \sum_{ij} \exp(R^0_{ij} - d_{ij}/B)$, where B is an empirical constant set to 0.37Å, d_{ij} denotes the bond distance of the central metal site to a considered nearest ion, and R^0_{ij} is a tabulated bond valence parameter specific to the cation-anion pair [25].

In practice, bond valence sums in mixed valent compounds rarely show integer values corresponding to the valences expected from the nominal oxidation states. For instance, in magnetite (Fe_3O_4), predicted Fe^{2+} states show BVS values ranging from 2.41 to 2.57, while Fe^{3+}- like states have BVS values ranging from 2.61 to 2.94 [14]. This is also observed in well-defined charge ordered oxides, such as in the insulating phase of the transition metal perovskite $Ca_2Fe^{3+}Fe^{5+}O_6$, which is a thermoelectric material presenting semiconducting behaviour at 290 K. Below this temperature, Fe^{3+} and Fe^{5+} ions order in the lattice. BVS values associated with the expected Fe^{3+} and Fe^{5+} sites give 3.48 and 4.58, respectively [26]. Therefore, due to orbital overlap and other charge-mixing effects, BVS values are more reliable for comparing oxidation states between sites rather than for determining an absolute oxidation state at any single site.

2.3 Establishing Charge Order by means of XRD, XAS and XANES

The presence of charge order in a system is typically confirmed through more precise or direct measurements like diffraction and spectroscopy based techniques, which probe the local structural and electronic environment of a material. In general, it is difficult to directly observe charge order in a mixed valent compound. In the case of x-ray diffraction, the observed scattering power depends on the total number of electrons on the atom. To directly observe charge order would require distinguishing x-ray scattering intensities between atoms with different oxidation states, and thus differences in intensity on the order of a single electron. Moreover, crystallographic refinements often use the same scattering factors for different ionic states of the same element. Therefore, detecting superlattice peaks due to charge localization is often challenging with x-ray diffraction. Neutron diffraction can determine magnetic structures in magnetically ordered systems, as it can detect individual magnetic moments. However, this technique is not directly sensitive to electronic charge.

Although direct measurements of charge order are limited, the periodic ordering of two valence states in a material can still be established indirectly via x-ray and neutron techniques. This involves detecting changes in peaks associated with structural distortions resulting from charge order, as well as variations in first-shell interatomic distances and in subsequent BVS values [4].

We now review signature features of Verwey compounds observed in XRD, XAS and XANES measurements.

2.3.1 X-Ray Diffraction (XRD)

Using high-energy (synchrotron) X-ray diffraction, Fe_3O_4 shows a structural distortion in the B-site FeO_6 octahedra when transitioning to insulating behaviour below 120 K [13]. Small crystals were used to mitigate microtwinning and multiple scattering effects. In this study, interionic bond lengths were extracted from refinement and used to compare ion displacement values due to breathing modes (Q_{rad}) and Jahn-Teller distortions (Q_{JT}) to BVS values. Results from this analysis determined the presence of a linear three site distortion, referred to as trimeron order.

In Fe_5O_6, a structural transition was observed to accompany the conductor-insulator transition at $T_V \approx 270$ K, using temperature-dependent single-crystal X-ray (synchrotron) diffraction [22]. Above T_V, Fe cations form two linear chains of FeO_6 octahedra. Fe_5O_6 presents an orthorhombic Cmcm (No. 63) space group and contains three distinct Fe sites. BVS analysis of the Fe-O bond lengths gives values of 2.57(6), 2.43(7) and 1.97(4) for the Fe1, Fe2, Fe3 sites, where Fe3 sites have a predicted oxidation state of Fe^{2+}, while Fe1 and Fe2 are mixed Fe^{2+}/Fe^{3+} states. Below the transition temperature T_V, new superlattice peaks are observed, suggesting additional structural order. In the low-temperature phase, the structure is refined in the $P2_1/m$ monoclinic space group. BVS values of the previously mixed Fe1 and Fe2 sites show closer values to Fe^{3+} and Fe^{2+} oxidation states, respectively. Structural models of this behavior determined that new Fe-Fe chemical bonds form between adjacent ions in the linear octahedral chains, leading to dimerization of the Fe chains.

2.3.2 X-ray Absorption Spectroscopy (XAS)

In rare earth perovskite nickelates, short-range charge order was studied on Ni sites using K-edge X-ray absorption spectroscopy on polycrystalline samples [27]. For lighter lanthanides (R = Pr, Nd, Sm, Eu), both metallic and insulating states exhibit an overall orthorhombic structure (Pbnm space group) containing regular NiO_6 octahedra. Focusing on the EXAFS (extended X-ray absorption fine structure) region of the $NdNiO_3$ spectra, a slight increase in some of the Ni-O bond lengths was found when decreasing temperature through the transition. Clear peak splitting was observed in the Fourier transformed spectra. Through comparison between FEFF simulations and the experimental data, it was shown that the low-temperature short-range Ni environment cannot be modeled by a single crystallographic Ni site. Instead, comparable spectra were obtained only when combining two Ni sites with identical backscattering atoms but with slightly different average bond lengths, leading to beating in the amplitude function and splitting in the Fourier transformed signal. Therefore, the coexistence of two inequivalent Ni sites with distinct Ni-O bond lengths was proven, demonstrating modifications in the Ni nearest-neighbours environment due to charge order across the MIT.

2.3.3 X-ray Absorption Near Edge Spectroscopy (XANES)

The Ir spinel compound $CuIr_2S_4$ [28] undergoes a metal-to-insulator transition at $T_V \approx 230$ K, accompanied by a structural distortion to a triclinic space group, as observed in the near-edge features of its X-ray absorption (XAS) and photoemission spectra (XPS). In this compound, Cu ions populate the A-site and are tetrahedrally coordinated by four S ions, while Ir ions occupy the B-site, which is octahedrally coordinated by six S ions. Above the transition temperature T_V, all B-sites are equivalent, with a nominal $\mathrm{Ir}^{3.5+}$ oxidation state. Using photoemission spectroscopy with an X-ray source, two peaks originating from the Ir $4f_{7/2}$ and $4f_{5/2}$ core levels are observed in the metallic phase. When the temperature is decreased below T_V, each peak is split into two components, suggesting Ir^{3+} and Ir^{4+} charge separation. In the XANES region of the K-edge XAS spectra, a new peak appears below T_V, attributed to Ir $5d$ t_{2g}–$5d$ t_{2g} antibonding states formed through hybridization with S $3p$ states, indicative of Ir^{4+}–Ir^{4+} dimerization.

In summary, the most important features confirming the Verwey nature of a mixed-valent compound include an abrupt increase in electrical resistivity ρ at the transition temperature T_V, an anomaly in a second bulk measurement, a change in BVS values of the mixed site below T_V, and structural distortions evident through peak splitting and the appearance of new superlattice peaks.

Chapter 3

$Pb_3Rh_7O_{15}$ Background

Now that we have a better understanding for how Verwey compounds are identified experimentally, we can proceed to the central material investigated in this thesis, $Pb_3Rh_7O_{15}$.

$Pb_3Rh_7O_{15}$ is a $4d$ transition metal compound where the Rh ions exhibit a nominal valence of $Rh^{3.43+}$, corresponding to a 3:4 ratio of Rh^{4+} to Rh^{3+} cations, assuming O^{2-} and Pb^{2+} oxidation states for the O and Pb ions. In 1978, A. Boonstra and C. Mutsaers [29] reported a conductor-to-insulator transition in $Pb_3Rh_7O_{15}$ at $T_V = 185$ K and a band gap of 0.1 eV. This material has been proposed as a candidate for the first $4d$ Verwey-type compound, which remains to be confirmed experimentally, as the low-temperature structure has not yet been solved. In this chapter we summarize previous bulk characterizations of the material and consider the proposed model for the structure below the transition temperature T_V.

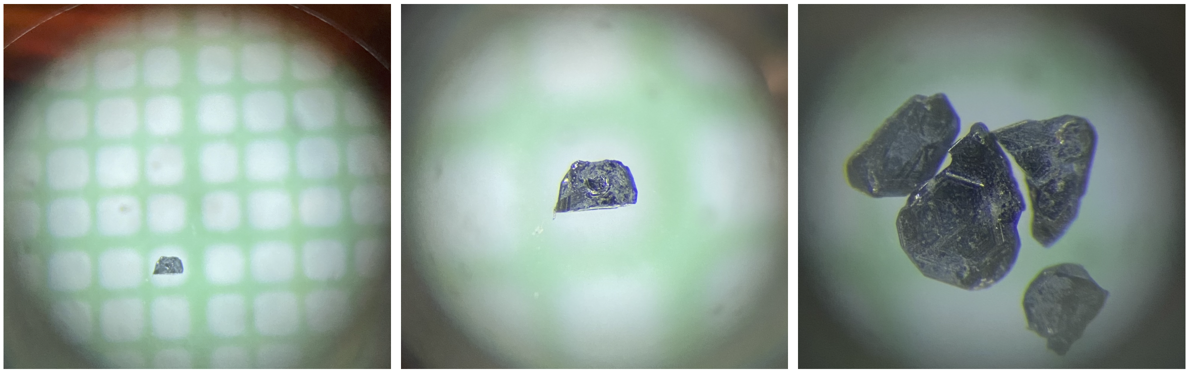

Figure 3.1: $Pb_3Rh_7O_{15}$ single crystals grown and provided by Jiaqiang Yan, a crystal grower at Oak Ridge National Laboratory. As seen from these images, these crystals are black and plate-like, with approximate dimensions of $1 \times 1 \times 0.1$ mm.

3.1 Reported Bulk Measurements

Before we begin our analysis of $Pb_3Rh_7O_{15}$, we list all previously reported macroscopic properties of this material. Measurements were carried out on single crystal and polycrystalline samples, which were grown by dissolving Rh_2O_3 in PbO flux and heating the resulting mixture in air at ambient pressure [30]. Single crystals of $Pb_3Rh_7O_{15}$ are shown in Fig. 3.1, which were obtained from the same batch of crystals used in a pressure-dependent study by Yan Li et al [31], reporting a detailed synthesis description and characterizing the macroscopic properties of this material. Crystals from this batch were used in our measurements described in chapters 4, 5 and 6.

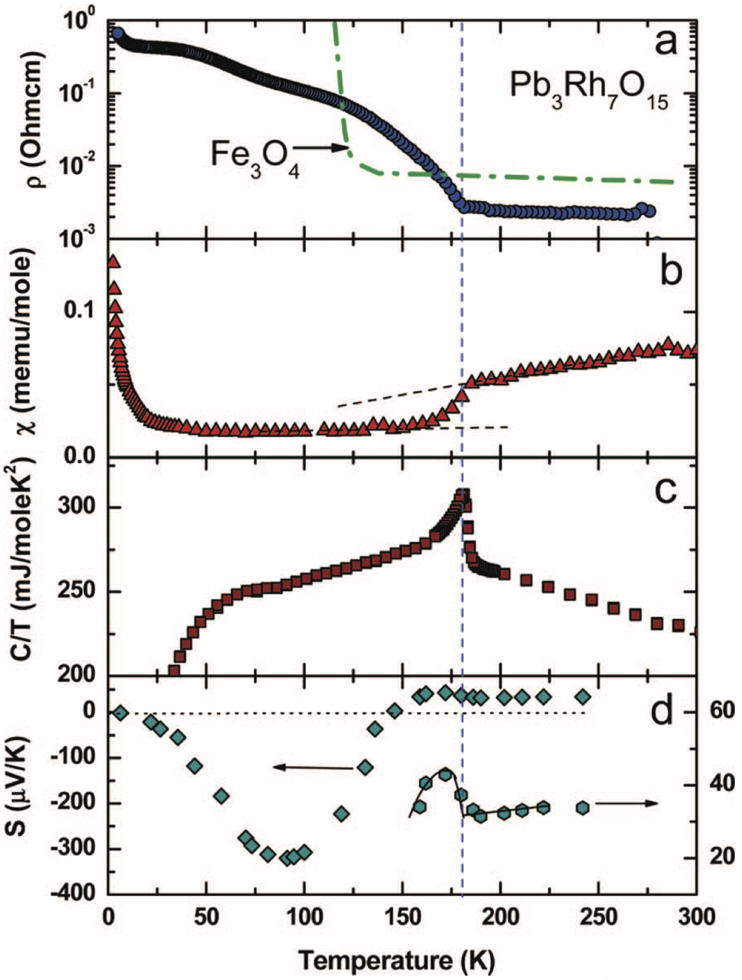

Figure 3.2: Reported $Pb_3Rh_7O_{15}$ Macroscopic Properties [30]: a) electrical resistivity ρ of $Pb_3Rh_7O_{15}$ (both parallel and perpendicular to the c-axis) compared to the resistivity of Fe_3O_4 shown in green, b) magnetic susceptibility χ, c) heat capacity C/T and d) Seebeck coefficient as a function of temperature. In d), the octagon points represent a closer look at the Seebeck data near the transition.

At room temperature, the isotropic electrical resistivity $\rho(T) \approx 1 \times 10^{-3}$ Ω cm. As the temperature decreases, $\rho(T)$ increases ($d\rho/\mathrm{dT} < 0$) [30]: at T_V the resistivity rises suddenly, then plateaus until approximately 70 K, after which it increases again at lower temperatures [31]. The abrupt increase in $\rho(T)$ at T_V is associated with the opening of a band gap. Below T_V, $\rho(T) \approx 10^{-1}$ Ω cm, which is several orders of magnitude less insulating than Fe_3O_4, with low-temperature resistivity values on the order of 10^6 Ω cm. This significant difference in low-temperature resistivity suggests that the charge carriers are less localized in $Pb_3Rh_7O_{15}$ below T_V, which is hypothesized to be due to the more spatially extended $4d$ orbitals in Rh compared to the $3d$ orbitals in Fe, leading to reduced intrasite Coulomb repulsion U [31]. It is interesting to note that both above and below the transition temperature, the slope of the resistivity curve remains negative, suggesting that the system never fully exhibits metallic behaviour. This justifies describing the observed electrical transition in $Pb_3Rh_7O_{15}$ as a conductor-to-insulator rather than a metal-to-insulator transition. As previously mentioned in section 2.1.2, from the comparison with the Fe_3O_4 resistivity shown in Fig. 3.2 a), the slope of $\rho(Fe_3O_4)$ remains negative above T_V as well and does not follow the temperature dependence characteristic for a metal, even though the transition in Fe_3O_4 is often referred to as a metal-to-insulator transition.

Hall resistivity $\rho_{xy}(H)$ measurements yield a linear curve with a positive slope, indicating dominant hole carrier behaviour across the entire temperature range. The extracted carrier density, given by $n = 1/R_H$, increases monotonically from room temperature down to $\approx$ 70 K and presents a minor anomaly at T_V. Mobility, defined by μ=$R_H/\rho e$, shows a rapid decrease at T_V, marked by a change in slope going from high to low temperature. Below $\approx$ 70 K, μ decreases rapidly before reaching a plateau below approximately 30 K [31].

Specific heat measurements show a clear λ-shaped anomaly at T_V, which is typically characteristic of a second order transition [31].

The Seebeck coefficient, measured on a sintered pellet, changes from positive to negative in the "metallic" phase ($T \approx 185$ K) as the temperature decreases, signifying a change from dominant electron to hole charge carrier behaviour on cooling. At the transition temperature $T_V \approx 150$ K, $S(T)$ is exhibits a small but distinct discontinuity [30].

In zero-field cooled and field cooled measurements, magnetic susceptibility $\chi(T)$ curves are identical, showing no signs of hysteresis and thus no complex magnetic transitions. Above the transition temperature T_V, $\chi(T)$ is linear and increases slowly with temperature, which is characteristic metallic behaviour. At the transition temperature $\chi(T)$ decreases abruptly, suggesting a sudden decrease of the density of states [31].

Additional studies have investigated fine-tuning effects on the transition in $Pb_3Rh_7O_{15}$. For instance, when studying doping effects, as Bi is substituted for Pb, the transition at T_V is suppressed and the insulating phase disappears [30].

In a pressure dependent study by Yan Li et al [31], the electrical resistivity ρ of $Pb_3Rh_7O_{15}$ was measured under hydrostatic pressures of up to 8 GPa with a cubic anvil cell apparatus. At $P_C \approx 3$ GPa, the transition was suppressed, with the system exhibiting metallic behaviour below 70 K. This critical pressure was found to be approximately half of the Fe_3O_4 critical pressure, reported as $P_C \approx 6 - 8$ GPa. This difference in pressure scales is presumed to be due to the more spatially extended nature of the $4d$ orbitals in Rh compared to the $3d$ orbitals in Fe in Fe_3O_4, which may contribute to making potential charge localization in $Pb_3Rh_7O_{15}$ more susceptible to destabilization through pressure [31]. As the pressure is increased, the metallic region shrinks gradually until it disappears at pressures above 7 GPa. This phenomenon is thought to be due to "reentrant" charge localization, where charge carriers in $Pb_3Rh_7O_{15}$ return to being localized, resulting in insulating behaviour at high pressures.

Bulk properties of $Pb_3Rh_7O_{15}$ share similarities with the bulk properties exhibited by known Verwey compounds. Some Rh^{4+} and mixed-valent Rh^{3+}/Rh^{4+} rhodates have been reported to exhibit metal-to-insulator transitions, but none show abrupt changes in their macroscopic properties like $Pb_3Rh_7O_{15}$ [30].

3.2 Proposed Charge Order and Structural Distortion

The transition at $T_V \approx 185$ K is hypothesized to be a Verwey-type transition, where the insulating state is due to charge ordering of the Rh^{3+} and Rh^{4+} cations [30].

Charge ordering has been reported in other mixed-valent rhodates such as $(Bi_6O_5)Rh_{12}O_{24}$, where magnetic susceptibility and thermopower measurements, along with BVS analysis were used to establish its presence [32]. In this material, only partial charge ordering of the Rh^{3+} and Rh^{4+} cations is achieved, as most sites remain disordered in the insulating state. $Pb_3Rh_7O_{15}$ is the only known candidate for a classical Verwey-type transition in a rhodate, and, more broadly, in any $4d$ transition metal oxide.

It is generally difficult to determine charge order in rhodates, due to the small difference between the Rh^{3+} and Rh^{4+} ionic radii, which is approximately 0.06 Å. In comparison, the difference between the radii of Fe^{2+} and Fe^{3+} cations is more than twice as large, measuring approximately 0.135 Å [30]. Therefore, charge order in rhodates would cause smaller displacements of the oxygen ligands, leading to more subtle structural distortions.

Reported High Temperature Structure for $Pb_3Rh_7O_{15}$ [33].

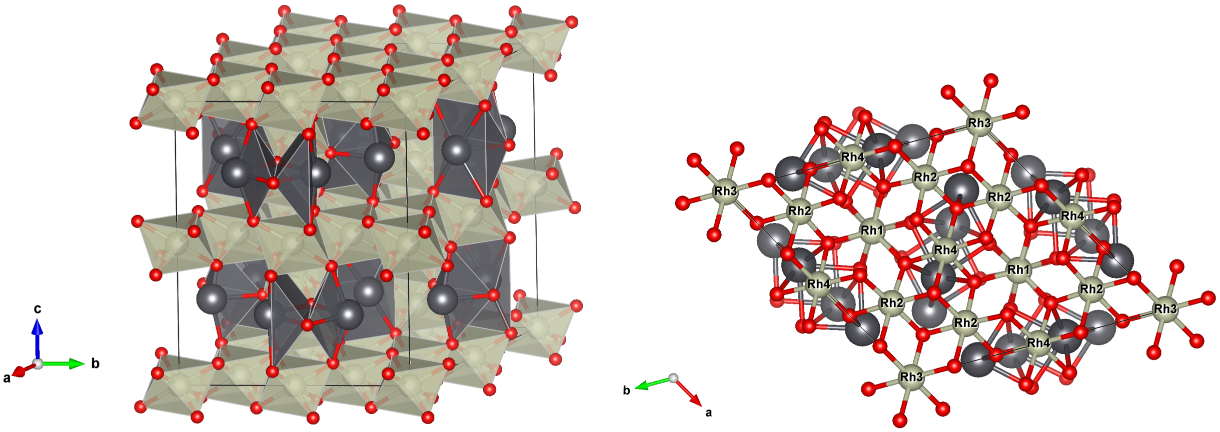

Figure 3.3: Rh - light gray, Pb - dark gray, O - red. Left panel shows the RhO_6 octahedra and RhO planes, interspersed by the PbO planes. Right panel displays all four inequivalent Rh sites, labeled Rh1 to Rh4.

In 2009, Mizoguchi et al. [30] reported a space group change accompanying the conductor-insulator transition in $Pb_3Rh_7O_{15}$, based on single-crystal XRD refinement. Above the transition temperature T_V, $Pb_3Rh_7O_{15}$ has a hexagonal structure in the $P6_3/mcm$ (no.193) space group, with reported lattice parameters of $a = 10.3537$Å and $c = 13.2837$Å at room temperature. The structure consists of alternating RhO planes separated by PbO planes, as shown in Fig. 3.3. Each Rh cation is situated within a RhO_6 octahedron, coordinated by neighbouring oxygen atoms that are shared with adjacent sites. There exist four inequivalent crystallographic Rh sites, identified in the right panel of Fig. 3.3. The octahedra at the Rh2, Rh3 and Rh4 sites share edges to form the RhO planes, which contain periodic hexagonal voids. Meanwhile, the octahedra at the Rh1 sites form face-sharing dimers aligned along the c-axis, located between the RhO planes. These Rh1 octahedra also share oxygen atoms with the interstitial positions in the RhO planes.

Proposed Charge Ordering Scheme in $Pb_3Rh_7O_{15}$.

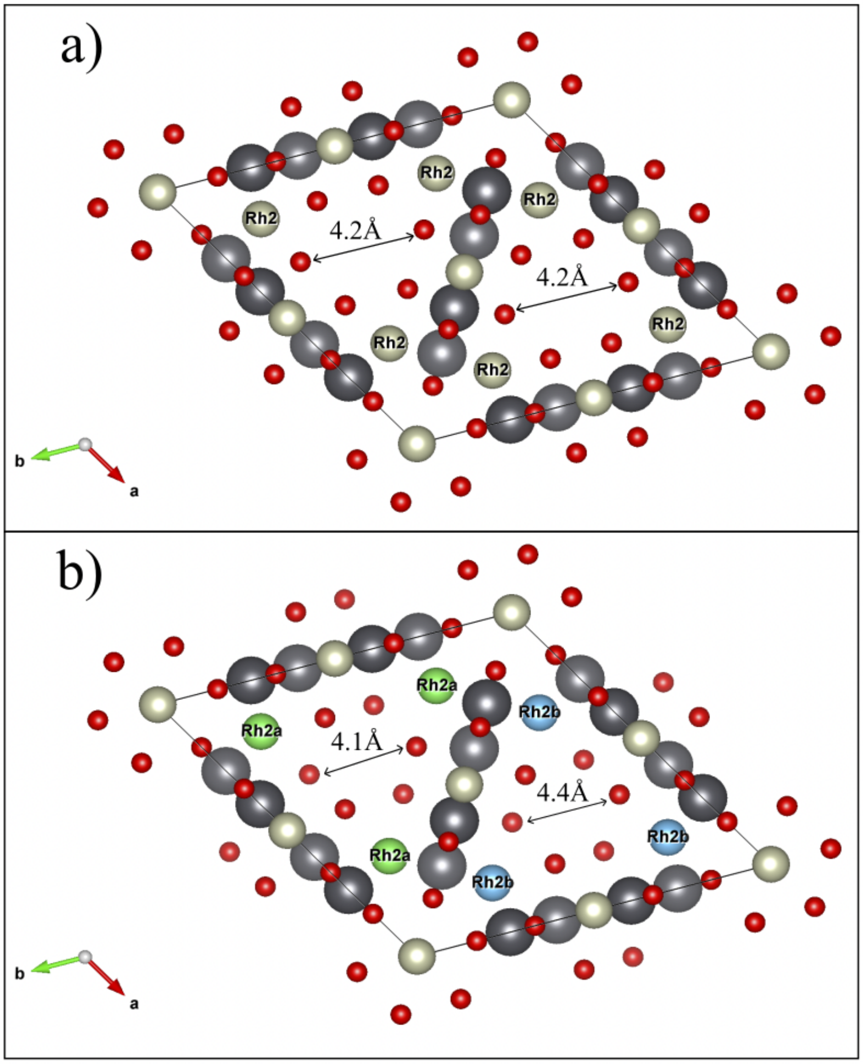

Figure 3.4: Crystal structures reported by Mizoguchi et al. [30] a) Above T_V, the Rh2 site has a nominal oxidation state of $Rh^{3.5+}$. The two hexagonal rings have identical inner diameters of 4.2 Å. b) In the low temperature phase, there are two inequivalent Rh2 sites, with Rh^{4+} and Rh^{3+} cations occupying the green Rh2a and blue Rh2b sites respectively. The hexagonal rings present two distinct inner diameters.

The oxidation state of each Rh site in the high-temperature structure of $Pb_3Rh_7O_{15}$ is predicted using two complementary methods. In the first approach, the high electrical conductivity at room temperature suggests that the oxidation states of the Rh sites are influenced by the modulation of charge carrier density in the crystal lattice [30]. More specifically, this method considers the relative hole occupancy in the $4d$ t_{2g} band of each Rh atom, where Rh^{3+} cations have a filled t_{2g} band with no holes and Rh^{4+} cations have one hole per t_{2g} band. In the RhO layers, the hole concentration is expected to be at a minimum for the sites sharing a maximum number of edges. Therefore, a minimum hole concentration is predicted for the octahedra sharing 6 edges, intermediate for those sharing 5 edges, and maximum for the octahedra sharing 4 edges. Similarly, low hole concentration is anticipated for the face sharing octahedra sites. The second method involves bond valence sum calculations, which give BVS values of 3.14, 3.45, 3.26 and 3.89 for the Rh1, Rh2, Rh3 and Rh4 sites, respectively, supporting the hole concentration arguments. Building on these results, the oxidation states of the Rh sites in $Pb_3Rh_7O_{15}$ above T_V are determined to be Rh^{3+} for the Rh1 and Rh3 sites, Rh^{4+} for Rh4, and $Rh^{3.5+}$ for the Rh2 sites. Therefore, Rh2 is the only expected mixed-valent crystallographic site, where Rh^{3+} and Rh^{4+} cations share an equal probability of occupying the site. In this model, the hexagonal voids are formed by the mixed-valent Rh2 sites, which are thought to be responsible for the conductive state of $Pb_3Rh_7O_{15}$ above T_V.

Single crystal X-ray diffraction measurements at 110 K showed no evidence of a change in space group below T_V. However, attempts to refine the structure in the #193 space group gave unphysical displacement factors for certain atoms, as well as an increase in R values, which does suggest a structural transition at T_V. Mizoguchi et al. proposed that when going through the transition temperature T_V, the bond lengths between the Rh and O ions at the Rh2 sites change, resulting from a modification in the nominal valence of the Rh2 site. Using the bond lengths obtained from the low-temperature refinement, the Rh2 site, which had a single BVS value of 3.45 in the high-temperature phase, now presents distinct BVS values of 3.36 and 3.85. Based on these results, it is proposed that below T_V, the $Rh^{3.5+}$ cations at the Rh2 site separate into two distinct sites with nominal oxidation states of Rh^{3+} and Rh^{4+}, leading to a charge-ordered insulating state, as depicted in Fig. 3.4. The decoupling of the Rh2 site into Rh2a and Rh2b sub-sites causes a decoupling of the two hexagonal rings, as they no longer exhibit identical inner diameters of 4.2 Å. The smaller ring, of inner diameter 4.1 Å is surrounded by Rh^{4+} cations from the Rh2a sites, while the larger ring, of inner diameter 4.4 Å is formed by the Rh^{3+} cations of the Rh2b sites.

To accommodate this lowering of symmetry, the $P\overline{6}c2$ space group (no.188) was selected to describe the low temperature structure of $Pb_3Rh_7O_{15}$. However, refinement in this space group reportedly resulted in negative displacement factors for several atoms. As a result, the authors of the study suggested that the real space group remains undetermined and is likely to possess lower symmetry. No low-temperature structure CIF files, reported structural parameters, or atomic coordinates have been published to supplement this work. For simulation purposes, we generated a CIF file based on the published high-temperature structure data and the previously mentioned details regarding the low-temperature $Pb_3Rh_7O_{15}$ structure. To achieve this, we converted the atomic coordinates and Wyckoff positions of each crystallographic site from the $P6_3/mcm$ space group to the $P\overline{6}c2$ space group. We then displaced the O atoms such that the hexagonal ring formed by the Rh^{4+} cations exhibits an inner diameter of 4.090(12) Å and the hexagonal ring surrounded by the Rh^{3+} cations has an inner diameter of 4.429(16) Å. BVS analysis of the resulting Rh-O bond lengths yielded values close to reported bond valence sums: 3.82 (calculated) vs. 3.85 (reported) for the Rh2a site, and 3.40 vs. 3.36 for the Rh2b site.

Using the published high-temperature and generated low-temperature CIF files, we simulated several types of 1D powder spectra: XRD powder diffraction in Vesta, neutron powder diffraction in PowderCell, and 1D-PDF in ADDIE SimulatePDF, all displayed in Fig. 3.5. XRD and neutron powder spectra were calculated using wavelengths of $\lambda = 1.54$ Å and $\lambda = 2.21$ Å, respectively, based on Bragg's law: $n\lambda = 2d \sin\theta$, where n is an integer, d is the interplanar spacing, and θ is the scattering angle. The pair distribution function (1D-PDF) calculates the probability of finding a pair of atoms with a separation distance of r. This technique is also known as "total scattering", as it considers both Bragg scattering and diffuse scattering. The final spectrum $g(r)$ is the Fourier transform of the scattering pattern obtained in reciprocal space given by: $g(r) = \frac{1}{4\pi r^2}\frac{dN}{dr}$, where $g(r)$ is the pair distribution function, $\frac{dN}{dr}$ corresponds to the number of atoms in a specified distance range, r is the separation distance between a pair of atoms [34].

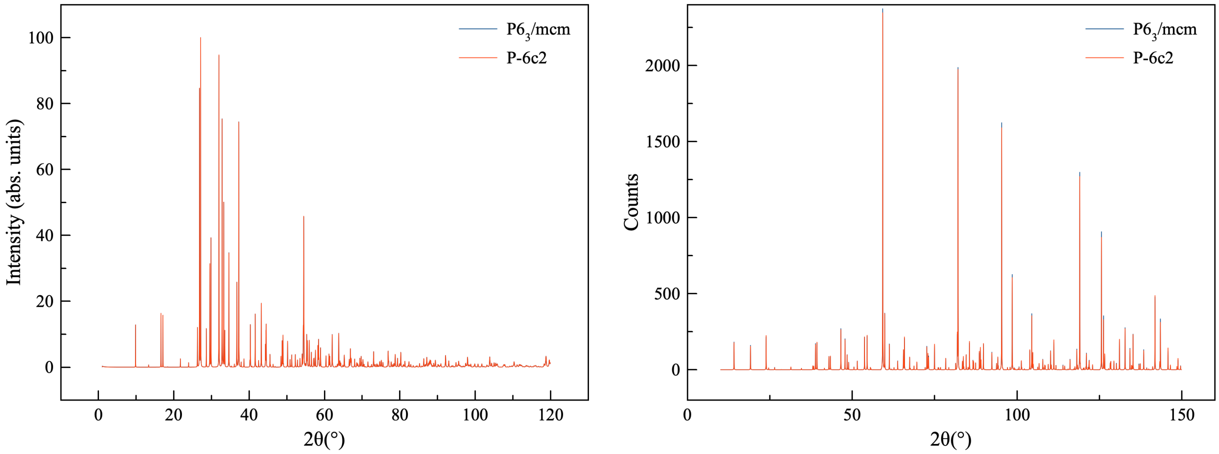

(a) XRD (1.54 Å)

(b) NPD (2.21 Å)

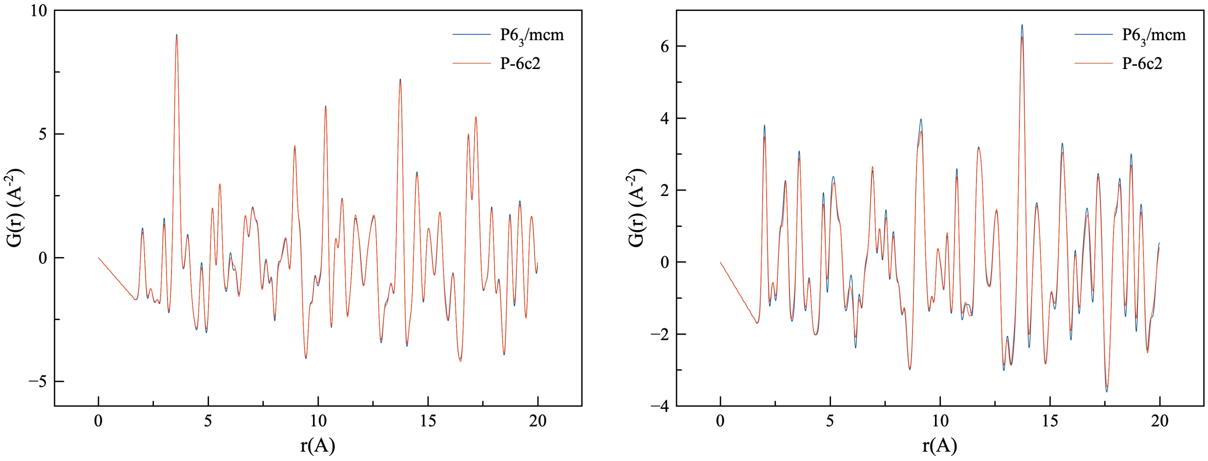

(c) 1D PDF (X-rays)

(d) 1D PDF (Neutrons)

Figure 3.5: Diffraction Patterns calculated from Proposed $Pb_3Rh_7O_{15}$ High and Low-Temperature Structures: a) Simulated X-ray powder diffraction pattern using Vesta. b) Neutron powder diffraction pattern calculated using PowderCell. Simulations of 1D pair distribution functions (PDF) by X-rays (c) and neutrons (d) using ADDIE SimulatePDF.

For all simulated spectra, no additional peaks are observed between the high and low temperature data, and only minor peak intensity variations on the order of single counts. The largest intensity variations appear in the 1D-PDF neutron spectra; however, even with these changes, no additional peaks are observed between the high and low-temperature data. This motivates the need for additional single crystal measurements, which we perform through a combination of single crystal X-ray diffraction, high dynamic range reciprocal space mapping (HDRM), 3D-Δ PDF analysis and XAS measurements.

Based on previous studies, there is no conclusive experimental evidence establishing charge order as the driving mechanism of the reported conductor-insulator transition in $Pb_3Rh_7O_{15}$. The foundational argument of this model relies on bond valence sums, which are calculated from the bond lengths between Rh and O atoms in the first Rh coordination shell. However, as noted earlier, no satisfactory low-temperature structure refinement has been reported in the literature. Therefore, the low-temperature structure of $Pb_3Rh_7O_{15}$ must be solved to validate or invalidate the proposed ordering scheme.

Chapter 4

Average Structure Analysis using Single Crystal XRD

In this chapter, we present our single crystal X-ray diffraction (XRD) results, along with our subsequent BVS and symmetry analyses, which we use to solve the average low-temperature structure of $Pb_3Rh_7O_{15}$ and assess the proposed charge ordering scheme.

4.1 Experiment

All experiments described in this chapter were performed at the McMaster Analytical X-ray Diffraction Facility (MAX) at McMaster University. Single crystal XRD measurements were conducted on a black, plate-like $Pb_3Rh_7O_{15}$ crystal with dimensions of $0.05 \times 0.04 \times 0.02$ mm^3, using a Bruker Apex-II CCD diffractometer with Mo$K\alpha$ radiation ($\lambda = 0.71073$ Å). Data was collected at 297 K and 110 K, where the lower temperature was achieved using a He cryostream. For all refinements, the structure was solved with the XT [35] structure solution program and refined with the XL [36] refinement package using Least Squares minimisation, with Olex2 as the graphical interface [37].

The high-temperature structure (297 K) was solved in the $P6_3/mcm$ (no.193) space group using the Intrinsic Phasing method, with lattice parameters $a = 10.3514(9)$ Å and $c = 13.280(2)$ Å. The final R_1 value was 0.112 ($I > 2\sigma(I)$) and wR_2 was 0.0209.

The low-temperature structure was refined in three different space groups using the same data collected at 110 K. In all refinements, the same lattice parameters were found, with $a = 10.3485(8)$ Å, $c = 13.269(2)$ Å and $V = 1230.7(3)$Å^3. In the first refinement, the crystal was solved in the $P6_3/mcm$ space group (same structure observed above the electronic transition) using the Charge Flipping method, which yielded a final R_1 value of 0.0475 ($I > 2\sigma(I)$) and wR_2 of 0.1371. Next, the structure was refined in the $P\overline{6}c2$ (no.188) space group (reported space group by Mizoguchi et al.), using the Intrinsic Phasing method, resulting in values for R_1 of 0.0488 ($I > 2\sigma(I)$) and wR_2 of 0.1332. Finally, the structure was refined in the $P6_3cm$ (no.185) space group (selected by free refinement), also using the Intrinsic Phasing method. Twinning was observed, defined by the scale factors of 0.63564 and 0.36436, which reduced the final R_1 value to 0.0273 ($I > 2\sigma(I)$) and wR_2 to 0.0723.

The crystallographic parameters for the high-temperature $P6_3/mcm$, low-temperature

$P\overline{6}c2$ and $P6_3cm$ refinements are listed in Tab. 4.1.

	HT $P6_3/mcm$	**LT** $P\overline{6}c2$	**LT** $P6_3cm$
empirical formula	$Pb_3Rh_7O_{15}$	$Pb_3Rh_7O_{15}$	$Pb_3Rh_7O_{15}$
formula weight	1581.94	1581.94	1581.94
T (K)	297(2)	110(2)	110(2)
wavelength (Å)	0.71073	0.71073	0.71073
radiation type	MoKα	MoKα	MoKα
cryst syst	hexagonal	hexagonal	hexagonal
IT number	193	188	185
a (Å)	10.3514(9)	10.3485(8)	10.3485(8)
c (Å)	13.280(2)	13.269(2)	13.269(2)
V (Å^3)	1232.3(3)	1230.7(3)	1230.7(3)
Z	4	4	4
D (g cm^{-3})	8.527	8.538	8.538
μ (mm^{-1})	50.026	50.093	50.093
F(000)	2724	2724	2724
cryst size (mm^3)	0.05 × 0.04 × 0.02	0.05 × 0.04 × 0.02	0.05 × 0.04 × 0.02
θ range (°)	2.272-30.499	2.72-62.798	2.272-62.798
index ranges	$-14 < h < 14$ $-14 < k < 14$ $-18 < l < 18$	$-25 < h < 25$ $-25 < k < 25$ $-32 < l < 33$	$-25 < h < 25$ $-25 < k < 25$ $-32 < l < 33$
reflns collected	97884	432748	452476
independent reflns	715 ($R_{int} = 0.0690$) ($R_\sigma = 0.0172$)	6888 ($R_{int} = 0.1101$) ($R_\sigma = 0.0210$)	7044 ($R_{int} = 0.1057$) ($R_\sigma = 0.0221$)
reflections with $[I > 2\sigma(I)]$	713	6559	6717
completeness to θ_{max} (%)	100	100	99.9
max and min absorption	0.189 and 0.434	0.188 and 0.434	0.188 and 0.434
data/ restraints/ params	715/0/51	6888/0/78	7044/1/89
GOF on F^2	1.168	1.403	1.09
final R indices $[I > 2\sigma(I)]$	$R_1 = 0.0112$ $wR_2 = 0.0208$	$R_1 = 0.0488$ $wR_2 = 0.1326$	$R_1 = 0.0273$ $wR_2 = 0.0713$
R indices (all data)	$R_1 = 0.0112$ $wR_2 = 0.0208$	$R_1 = 0.0506$ $wR_2 = 0.1332$	$R_1 = 0.0289$ $wR_2 = 0.0723$
peak and hole	1.284 -1.699 e Å^{-3}	13.186 -13.120 e Å^{-3}	3.024 -6.486 e Å^{-3}

Table 4.1: Data collection and refinement parameters for high and low temperature refinements of the same $Pb_3Rh_7O_{15}$ single crystal.

4.2 Refinement Results and Discussion

The lattice parameters of the refined high-temperature structure are similar to the lattice parameters of the high-temperature structure reported by Mizoguchi et al. (refined: $a = 10.3485(8)$ Å, $c = 13.269(2)$ Å vs. reported: $a = 10.3537$ Å and $c = 13.2837$ Å). Moreover, the structure was refined in the same $P6_3/mcm$ space group, which gave lower values of R_1 and wR_2 than the reported parameters (refined: $R_1 = 0.112$, $wR_2 = 0.0209$ vs. reported: $R_1 = 0.0173$, $wR_2 = 0.0392$), indicating higher quality of our sample and XRD data. When refining the low-temperature structure in the same $P6_3/mcm$ space group, the R_1 value increased to 0.0475. This increase was also observed by Mizoguchi et al., who reported a new R_1 value of 0.0433, suggesting a change in the space group below the transition temperature T_V. However, when the low-temperature structure was refined in the previously reported $P\overline{6}c2$ space group, the R_1 value increased to 0.0488, providing a worse refinement than the original high temperature structure. This makes a difference from the previously reported refinement, where the R_1 value dropped to 0.0409. Additionally, the refinement reported in this space group exhibited unphysical displacement parameters. Similarly, our refinement in $P\overline{6}c2$ led to several initial unsuccessful attempts and warnings for unsolved atomic positions. In fact, the low-temperature structure could only be refined in this space group when the XT refinement package was constrained to solve the structure in $P\overline{6}c2$, which also applied to the low-temperature refinement in $P6_3/mcm$. When left unconstrained, the $P6_3cm$ space group was selected instead, resulting in a refinement with a significantly lower R_1 value of 0.0273. In this refinement, a twin was observed, which contributed to lowering R_1; however, even without accounting for this, R_1 remains below 0.04.

The structures solved through these refinements are described in Tab. 4.2, 4.3, and 4.4, which list the atomic coordinates and isotropic displacement parameters for the high-temperature $P6_3/mcm$, low-temperature $P\overline{6}c2$ and $P6_3cm$ space groups, respectively.

Atomic Coordinates and Equivalent Isotropic Displacement Parameters for $Pb_3Rh_7O_{15}$ at 297K.

Atom	**Wyckoff**	x	y	z	**U(eq)**^{1}
Rh1	6g	0.33333	0.66667	0.35130	0.00476
Rh2	6g	-0.16835	0.66329	0.50000	0.00485
Rh3	8h	0.00000	1.00000	0.50000	0.00571
Rh4	12i	0.00000	0.50000	0.50000	0.00472
Pb1	2b	0.00000	0.60500	0.25000	0.01258
Pb2	6f	0.00000	0.73636	0.75000	0.01002
O1	12k	0.00000	0.66630	0.57880	0.00670
O2	12k	-0.16930	0.83070	0.57725	0.00770
O3	24l	0.15829	0.66566	0.41865	0.00780
O4	12j	0.17780	0.52030	0.25000	0.00660

Table 4.2: ^{1}(Å^{2}10^3). U(eq) is defined as 1/3 of the trace of the orthogonalised U_{IJ} tensor. Structure refined in $P6_3/mcm$ space group, $a = 10.3514(9)$ Å, $c = 13.280(2)$ Å.

Atomic Coordinates and Equivalent Isotropic Displacement Parameters for $Pb_3Rh_7O_{15}$ at 110K: $P\overline{6}c2$.

Atom	**Wyckoff**	***x***	***y***	***z***	**U(eq)**^{1}
Rh1a	2c	0.33333	0.66667	0.50000	0.00350
Rh1b	4i	0.66667	0.33333	0.64707	0.00260
Rh2a	6j	0.16484	0.32968	0.50000	0.00290
Rh2b	6j	0.33320	0.16659	0.50000	0.00290
Rh3	4g	0.00000	0.00000	0.34961	0.00320
Rh4	6j	0.50175	0.49825	0.50000	0.00310
Pb01	6k	0.33352	0.06189	0.75000	0.00620
Pb02	6k	0.33356	0.40259	0.75000	0.00480
O1	12l	0.33210	0.33220	0.57860	0.00410
O2a	12l	0.17530	0.17410	0.41680	0.00940
O2b	6k	-0.00920	0.14650	0.25000	0.00520
O3a	12l	0.33310	0.49690	0.42320	0.00440
O3b	12l	0.49180	0.15930	0.58010	0.00380
O4	6k	0.51070	0.32380	0.75000	0.00550

Table 4.3: ^{1}(Å^{2}10^3). U(eq) is defined as 1/3 of the trace of the orthogonalised U_{IJ} tensor. Structure refined in $P\overline{6}c2$ space group, $a = 10.3485(8)$ Å, $c = 13.269(2)$ Å.

Atomic Coordinates and Equivalent Isotropic Displacement Parameters for $Pb_3Rh_7O_{15}$ at 110K: $P6_3cm$.

Atom	**Wyckoff**	***x***	***y***	***z***	**U(eq)**^{1}
Rh1a	4b	0.33333	0.66667	0.70841	0.00308
Rh1b	4b	0.33333	0.66667	0.50575	0.00302
Rh2	12d	0.16825	0.83134	0.35820	0.00307
Rh3	2a	0.00000	1.00000	0.35747	0.00341
Rh4	6c	0.00000	0.49994	0.35884	0.00303
Pb1	6c	0.39510	1.00000	0.61323	0.00563
Pb2	6c	0.00000	0.73579	0.60784	0.00487
O1a	6c	0.00000	0.66640	0.43720	0.00440
O1b	6c	0.00000	0.33400	0.27920	0.00480
O2a	6c	0.17080	1.00000	0.43460	0.00570
O2b	6c	0.00000	0.83130	0.28120	0.00490
O3a	12d	0.33370	0.83890	0.43630	0.00490
O3b	12d	0.15570	0.66510	0.27380	0.00490
O4	12d	0.47960	0.82280	0.60750	0.00530

Table 4.4: ^{1}(Å$^2 \times 10^3$). U(eq) is defined as 1/3 of the trace of the orthogonalised U_{IJ} tensor. Structure refined in $P6_3cm$ space group, $a = 10.3485(8)$ Å, $c = 13.269(2)$ Å.

The high-temperature refinement, as shown in 4.1a, yields the same high-temperature structure described by Mizoguchi et al. One unit cell contains three RhO and two PbO planes, where the RhO planes are formed by edge-sharing RhO_6 octahedra. As in the reported structure, these 2D RhO sheets present periodic hexagonal voids, of inner diameter 4.210(5) Å, similar to the reported value of 4.217(9) Å. Between the RhO planes, at these interstitial positions, lie Rh dimers formed by two face-sharing RhO_6 octahedra aligned along the c-axis, which are also present in the reported refinement. Finally, this structure presents the expected four crystallographic Rh sites.

The low-temperature $P\overline{6}c2$ refinement produces the structure shown in Fig. 4.1b. Here, one unit cell also contains two PbO and three RhO planes; however, the Rh4 and Pb1 sites are missing on the Rh2a (left) side in the ab-plane. Additionally, the Rh1 site is differentiated into two distinct Rh1a (left) and Rh1b (right) sites, leading to a total of six inequivalent Rh sites. The Rh1a sites are single RhO_6 octahedra situated at one of the two interstitial positions within the RhO ab-plane, filling the hexagonal void that was present in the high-temperature structure. The Rh1b sites form dimers located in the same position as the Rh1 sites in the high-temperature structure, on the right side of the ab-plane. Therefore, one hexagonal void remains, with an inner diameter of 4.190(17) Å, which is slightly reduced compared to its diameter in the high-temperature structure. These results contradict the proposed model for the low-temperature structure in this space group, which predicts two hexagonal rings: one with a reduced inner diameter of 4.1 Å on the left side and a larger inner diameter of 4.4 Å on the right.

Structures Obtained from Single Crystal XRD Refinement.

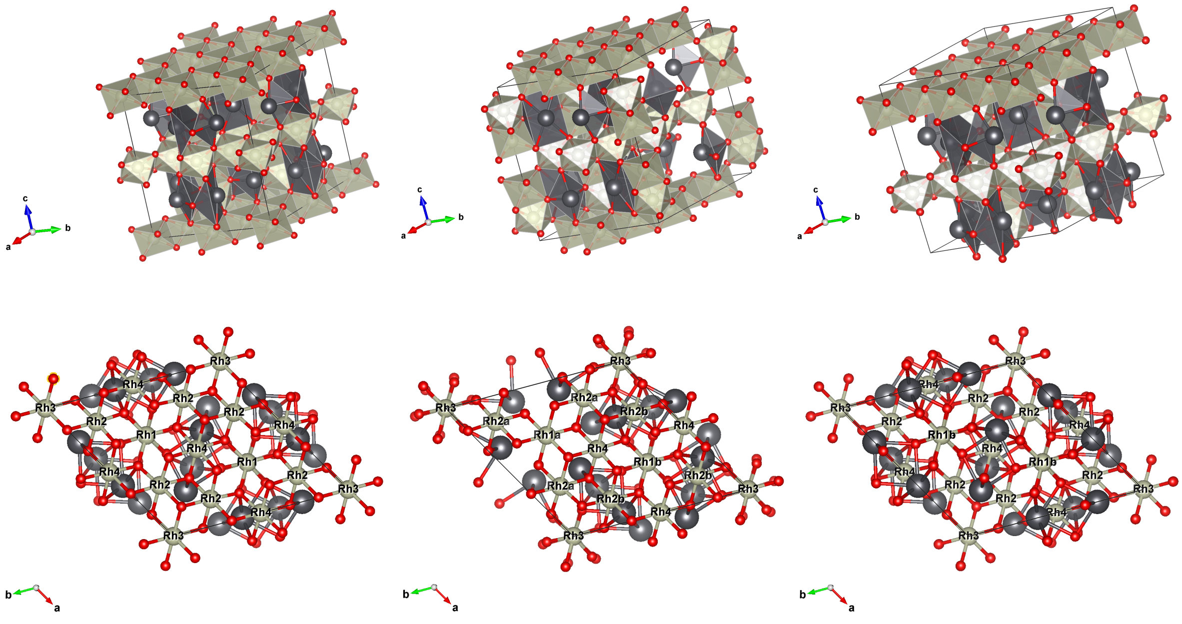

(a) HT: $P6_3/mcm$ (b) LT: $P\overline{6}c2$ (c) LT: $P6_3cm$

Figure 4.1: Rh - light gray, Pb - dark gray, O - red. Top: Polyhedral representation of the refined structures, highlighting the RhO and PbO layers. Bottom: ab-planes with crystallographic Rh sites, labeled Rh1 to Rh4.

The structure in $P6_3cm$, shown in Fig. 4.1c and produced by the low-temperature refinement with lowest R values, exhibits two RhO and two PbO planes in one unit cell. In this structure, the *ab*-plane in a RhO sheet possesses similar atomic sites as the high-temperature structure. Two hexagonal rings are present, both with an inner diameter of 4.0449(4) Å, contradicting the proposed model for the low-temperature structure of $Pb_3Rh_7O_{15}$. Moreover, the Rh1 site differentiates into two inequivalent sites, Rh1a and Rh1b, resulting in a total of five crystallographic Rh sites. The Rh1a and Rh1b sites form a face-sharing octahedral dimer between the RhO layers, with Rh1a above and Rh1b below the PbO plane.

4.2.1 Symmetry and BVS Analysis

Following the initial overview of the structures obtained from our single-crystal XRD refinement, we proceed with a more in-depth geometrical analysis to understand the specificities of each space group. This is achieved through symmetry analysis, where we consider the smallest non-repeating element in the unit cell, referred to as the asymmetric unit. The graphical interface Mercury was used to visualize and compare the symmetry elements present in each of the three space groups. The summary of this analysis is presented in Tab. 4.5, listing the number of symmetry operations by type for each space group. As evident from the breakdown, the $P6_3/mcm$ space group possesses the highest symmetry, with a total of 137 symmetry operations, compared to 63 for $P\overline{6}c2$ and 38 for $P6_3cm$. This aligns with the predictions made by Mizoguchi et al., postulating that the real space group of the low-temperature structure would possess lower symmetry than $P\overline{6}c2$.

From this analysis, the most notable difference in the $P\overline{6}c2$ space group, compared to the other two, is the absence of a mirror or glide plane that splits the *ab*-plane in two, as shown in Fig. 4.2. This allows for the decoupling of the two sides of the *ab*-plane and subsequent differentiation of Rh2 into the Rh2a and Rh2b sites, which describes the central geometric mechanism behind the ordering of the Rh^{3+} and Rh^{4+} cations in the structure. These specific mirror and glide planes remain in the $P6_3cm$ space group, preserving equivalent sites on both sides of the unit cell and thus preventing differentiation of the Rh2 mixed-valent site.

Symmetry Element	$P6_3/mcm$	$P\overline{6}c2$	$P6_3cm$
Inversion	27	0	0
2-fold screw	41	21	6
2-fold proper rotation	25	15	0
3-fold proper rotation	6	6	6
3-fold rotoinversion	4	0	0
6-fold screw	4	0	4
6-fold rotoinversion	6	6	0
Mirror plane	7	2	5
Glide plane	17	13	17

Table 4.5: Symmetry Element Comparison by Space Group.

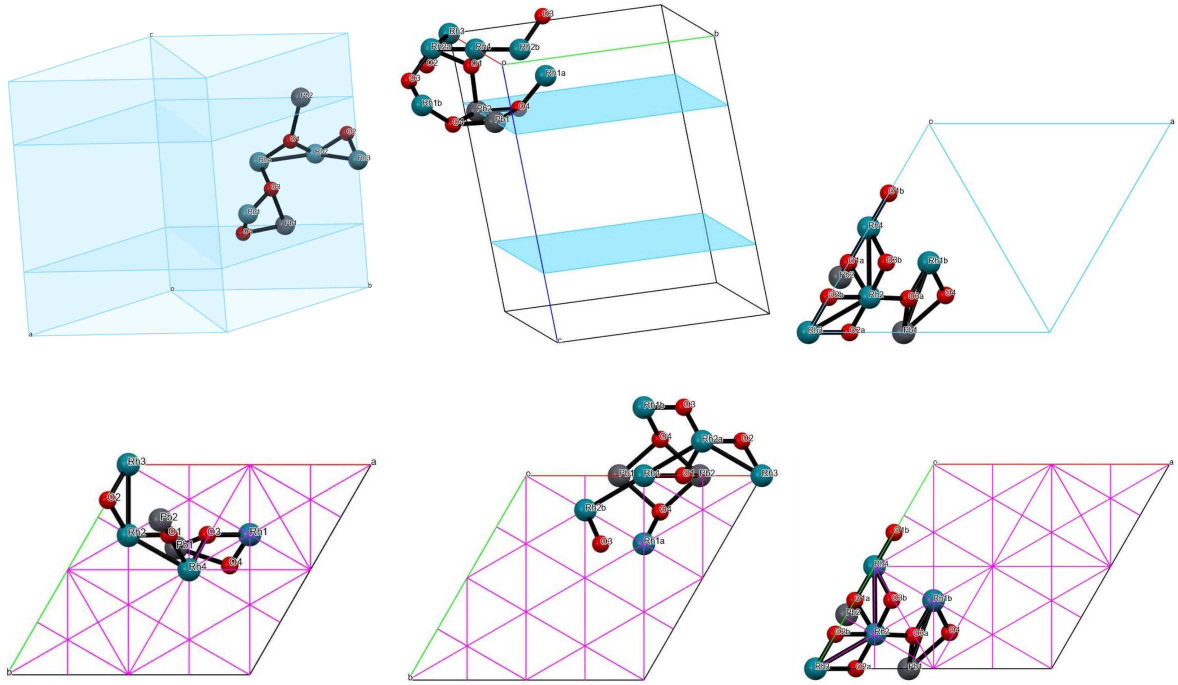

(a) $P6_3/mcm$ (b) $P\overline{6}c2$ (c) $P6_3cm$

Figure 4.2: Mirror (top, blue) and glide plane (bottom, magenta) symmetry element comparison between $P6_3/mcm$, $P\overline{6}c2$, and $P6_3cm$ space groups.

Expanding upon our qualitative symmetry analysis, we now move onto a more quantitative approach using the Bond Valence Sum (BVS) method. As discussed in Section 2.2, BVS calculations are based on the interionic distances in the first coordination shell of an atom. Tab. 4.6 lists the bond lengths between the Rh and O ions for each inequivalent Rh site in the high-temperature $P6_3/mcm$, low-temperature $P\overline{6}c2$ and $P6_3cm$ space groups. Using these bond lengths, the BVS values were calculated for all Rh sites in these refined structures, which are listed in Tab. 4.7.

BVS analysis of the Rh sites in the refined high-temperature structure yields comparable values to the bond valence sums of the reported high-temperature structure. Specifically, the calculated BVS value for Rh2 is 3.42, similar to the reported value of 3.45, thus confirming the Rh^{3+}/Rh^{4+} mixed-valent nature of the Rh2 site above the transition temperature T_V. The low-temperature $P6_3cm$ bond valence sums show a single value of 3.44 for the Rh2 site, suggesting a mixed Rh^{3+}/Rh^{4+} state below the transition temperature T_V. The BVS values reflect some differentiation of the Rh1 site, with 3.11 for Rh1a and 3.17 for Rh1b; however this difference is not large enough to suggest a deviation from the nominal Rh$_3^+$ valence at this site. In the $P\overline{6}c2$ refinement, no significant difference is observed between the BVS values of the two decoupled Rh2 sites: 3.41 for Rh2a and 3.48 for Rh2b. In fact, this contradicts the proposed model, which anticipates a higher oxidation state at the Rh2a site compared to Rh2b, with suggested BVS values of 3.89 for Rh2a and 3.26 for Rh2b.

It is important to note that when calculating the bond valence sum of a site, the choice of bond valence parameter R_{ij}^0 can often affect the final result. The values of $R(\text{III}) = 1.8$ and $R(\text{IV}) = 1.844$ were chosen for the Rh$^{3+} -$ O and Rh$^{4+} -$ O cation-anion pairs, respectively.

In the supplement to their work, Mizoguchi et al. justify using these parameters over the typical value of $R(\mathrm{III}) = 1.791$ [38] and other available Rh(IV) values in literature, as they are not found to be consistent with experimental results. Instead, the selected R^0_{ij} values for their BVS analysis were obtained using software developed by Brown [39], which is based on empirical data. For consistency, these are the R^0_{ij} values used in our BVS analysis as well. Since R^0_{ij} depends on the cation-anion pair, final BVS values can be adjusted closer to Rh^{3+} or Rh^{4+} valences, by choosing $R(\mathrm{III})$ or $R(\mathrm{IV})$ based on preliminary assumptions of nominal site valence. For the high-temperature $P6_3/mcm$ and low-temperature $P6_3cm$ structures, using either parameter when calculating the BVS values of the Rh2 sites gives values suggesting a mixed-valent state (HT $P6_3/mcm$: BVS(R(III)) = 3.42, BVS(R(IV)) = 3.49; LT $P6_3cm$: BVS(R(III))= 3.44, BVS(R(IV)) = 3.51). In the low-temperature $P\overline{6}c2$ structure, the choice of bond valence parameter does affect the final BVS values of the Rh2 sub-sites. However, for the same R^0_{ij}, the differences between the BVS values of Rh2a and Rh2b are not significant: using R(III), BVS(Rh2a) = 3.41, BVS(Rh2b) = 3.48; using R(IV), BVS(Rh2a) = 3.84, BVS(Rh2b) = 3.92.

Rh-O Bond Lengths (Å) in HT $P6_3/mcm$, LT $P\overline{6}c2$ and LT $P6_3cm$ Refined Structures of $Pb_3Rh_7O_{15}$.

HT $P6_3/mcm$	**LT** $P\overline{6}c2$	**LT** $P6_3cm$
Rh1-O3 2.0160 ×3	Rh1a-O3a 2.0300 ×6	Rh1a-O3b 2.0250 ×3
Rh1-O4 2.0635 ×3	Rh1b-O4 2.0790 ×3	Rh1a-O4 2.0610 ×3
	Rh1b-O3b 2.0120 ×3	Rh1b-O3a 2.0050 ×3
		Rh1b-O4 2.0690 ×3
Rh2-O1 2.0197 ×2	Rh2a-O1 2.0100 ×2	Rh2-O1a 2.0170
Rh2-O2 2.0178 ×2	Rh2a-O2a 2.0000 ×2	Rh2-O1b 2.0230
Rh2-O3 1.9878 ×2	Rh2a-O3a 2.0130 ×2	Rh2-O2a 2.0070
	Rh2b-O1 2.0111 ×2	Rh2-O2b 2.0190
	Rh2b-O3a 2.0072 ×2	Rh2-O3a 1.9690
	Rh2b-O3b 1.9871 ×2	Rh2-O3b 2.0020
Rh3-O2 2.0310 ×6	Rh3-O2a 2.0160 ×3	Rh3-O2a 2.0420 ×3
	Rh3-O2b 2.0490 ×3	Rh3-O2b 2.0180 ×3
Rh4-O1 2.0140 ×2	Rh4-O1 2.0260 ×2	Rh4-O1a 2.0140
Rh4-O3 1.9957 ×4	Rh4-O3a 2.0150 ×2	Rh4-O1b 2.0160
	Rh4-O3b 1.9760 ×2	Rh4-O3a 1.9820 ×2
		Rh4-O3b 2.0090 ×2

Table 4.6: HT=297K, LT=110K. Bond lengths used for calculating BVS values of the different Rh sites.

Temperature	**Space Group**	Rh **site**	**Average** Rh-O **bond length (Å)**	**BVS**
297K	$P6_3/mcm$	Rh1	2.04	3.15
		Rh2	2.01	3.42
		Rh3	2.03	3.22
		Rh4	2.00	3.92
110K	$P6_3cm$	Rh1a	2.04	3.11
		Rh1b	2.04	3.17
		Rh2	2.01	3.44
		Rh3	2.03	3.22
		Rh4	2.00	3.92
110K	$P\bar{6}c2$	Rh1a	2.03	3.21
		Rh1b	2.05	3.10
		Rh2a	2.01	3.41
		Rh2b	2.00	3.48
		Rh3	2.03	3.21
		Rh4	2.01	3.89

Table 4.7: Summary of average bond length distances and bond valence sums (BVS) for high and low temperature refinements of $Pb_3Rh_7O_{15}$.

In summary, our qualitative symmetry analysis, which demonstrates the presence of mirror and glide planes coupling the two sides of the *ab*-plane in the low-temperature refinement with lowest R values, and our quantitative BVS analysis, which shows that Rh2 BVS values remain around 3.5 across all refinements, provide no indication of differentiation of the Rh2 site that would suggest an ordering of Rh^{3+} and Rh^{4+} cations.

4.2.2 Reciprocal Space Mapping

Single crystal XRD refinement is sensitive to changes in the average structure of the crystal. This technique is suitable for testing the hypothesized charge ordering model, as it proposes a specific modification in the average structure of the crystal. If we consider more complex charge ordering schemes involving short-range correlations, such as electron delocalization over additional sites or dynamic temporal changes, diffuse scattering patterns in reciprocal space become relevant.

When there is no disorder present in a crystal, only Bragg peaks appear in reciprocal space due to constructive interference from the regular periodicity in the structure. If there is disorder along one direction, ie. between planes, this would lead to deconstructive interference along this direction. Therefore, scattering can only occur within the ordered planes. In reciprocal space, the resulting diffuse scattering appears as 2D sheets, perpendicular to the direction of disorder. If a structure presents disorder along two directions, ie. disorder within periodically arranged planes, scattering can only occur along the direction of order. This is seen as 1D-rods in reciprocal space, perpendicular to the disordered planes. Finally, if a crystal exhibits three dimensional short-range order in direct space, this would produce broad, low-intensity peaks in reciprocal space [40].

Fig. 4.3 presents MAX3D images of the high and low-temperature datasets collected by the detector, visualized in reciprocal space. The Bragg peaks are shown along the high-symmetry directions (where h and k are equivalent due to hexagonal symmetry of the crystal) and appear as distinct, high-intensity points. From these images, there seems to be no evidence of rod or sheet-like behaviour. However, due to the high scattering power of Pb, these datasets contain high background, which was removed to reveal the Bragg peaks. In doing so, the low counts are filtered, reducing the likelihood of observing diffuse scattering. This motivates the need for measurements at a synchrotron beamline, specifically designed for the detection and analysis of diffuse scattering.

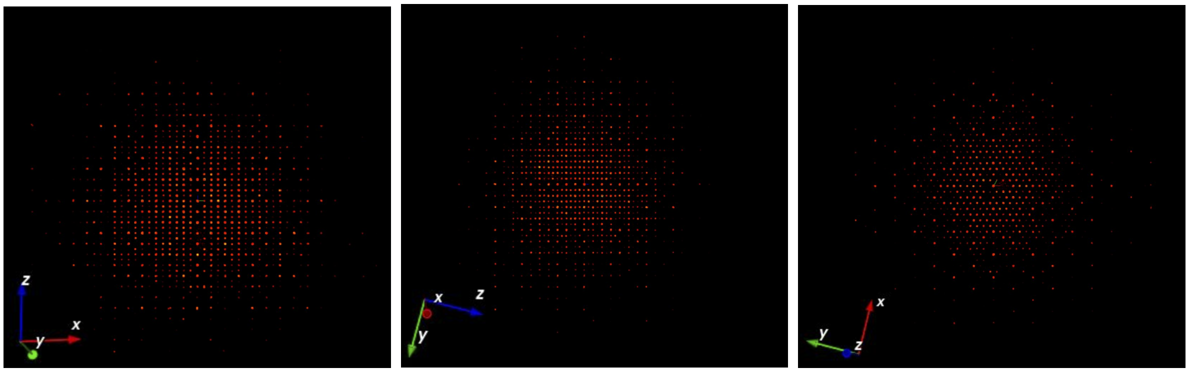

(a) HT KL plane (b) HT HL plane (c) HT HK plane

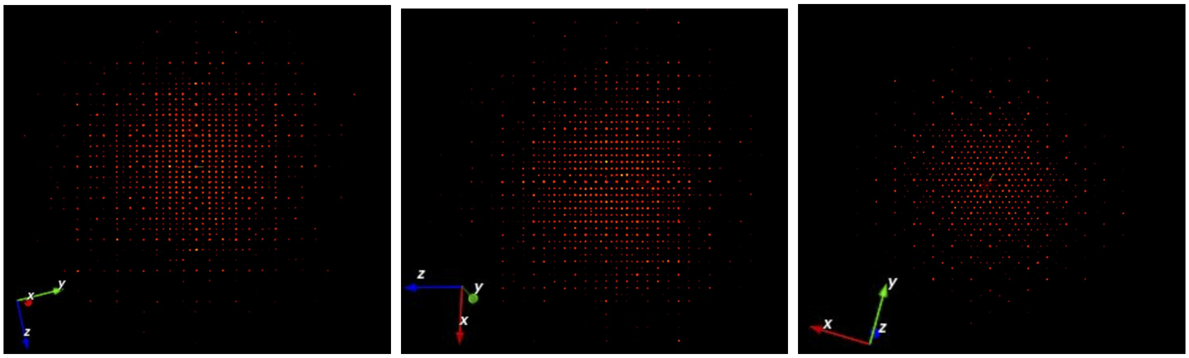

(d) LT KL plane (e) LT HL plane (f) LT HK plane

Figure 4.3: Reciprocal space maps obtained using MAX3D for the high-temperature (top) and low-temperature (bottom) structures along the H, K, and L directions. The axes correspond to the equivalent directions in direct space. Peaks are observed at all integer H, K, L positions, as no systematic absences are observed in primitive space groups.

Chapter 5

Local Structure Analysis using HDRM

Results from our single crystal XRD analysis showed no evidence of changes in the average structure of $Pb_3Rh_7O_{15}$ to support the proposed charge ordering scheme. As discussed in Chapter 2, established charge order in Verwey compounds often exhibits complex behaviour, such as stripe or polaron order. Thus, for broader considerations of charge order in $Pb_3Rh_7O_{15}$, we examine the short-range correlations present in the system.

In this chapter, we consider local structural changes in $Pb_3Rh_7O_{15}$ using High Dynamic Range Reciprocal Space Mapping (HDRM), which is a technique optimized for studying diffuse scattering. We present results from subsequent reciprocal space and 3D-Δ PDF analyses, investigating short-range structural correlations in the sample and allowing us to broaden our search for charge order in the insulating phase of $Pb_3Rh_7O_{15}$.

5.1 Experiment

This experiment was conducted at CHESS (Cornell High Energy Synchrotron Source), which is a high-intensity X-ray source located at Cornell University, Ithaca. The synchrotron produces high-energy X-ray beams with an energy range of 5 keV to 200 keV, enabling the study of bulk materials, while its high flux allows for the detection of weak signals.

A $Pb_3Rh_7O_{15}$ single crystal was mounted on a MiTeGen™ mount. HDRM was carried out at the CHESS ID4B QM^2 (Quantum Mapping for Quantum Materials) beamline, which has capabilities enabling characterization of quantum materials in Q-space across many length scales and temperature ranges, therefore spanning entire phase diagrams. The energy range available at QM^2 is 6 keV to 70 keV. An energy of 50 keV was selected for our measurements using a fully tunable diamond <111> Double Crystal Monochromator (DCM). The beamline has an energy resolution of $dE/E \approx 10^{-4}$ and spot size of 200 microns x 500 microns. Data was collected using a psi-circle goniometer, specifically a six-circle Huber diffractometer with four sample and two detector-orientation axes (4S+2D). The independent motion of the sample and detector orientations gives nine degrees of freedom, which can define any vertical diffraction plane. Measurements were taken between 100 K and 300 K, where temperature control was achieved with a closed-cycle helium cryostat using a single-stream flow. QM^2 uses a 6-megapixel Pilatus3 area detector (Pilatus 6M), which counts single photons and has a pixel size of 172×172 μm^2, a 2463×2527 pixel array, a 423.6×434.6 mm^2 active area, a 100 Hz frame rate, a 20-bit/pixel dynamic range, a count rate of 10 ph/s/pixel, and a readout time of 0.95 ms. Each map was collected through 30-minute scans with a 360° phi rotation at 2–3 chi values.

High Dynamic Range Mapping (HDRM) [41] is a technique that images wide regions of reciprocal space, measuring scattering intensity at approximately 30 million distinct Q positions per second. The high-energy, high-flux beam produces intense Bragg peaks in reciprocal space, useful for crystal structure refinement, as well as weaker features from superstructures associated with spin and/or charge order, and slowly modulated scattering due to phonons and short-range order. This technique involves using state-of-the-art detectors with low noise, single-photon sensitivity, high maximum count rate, millions of pixels, and high frame rates. Hence, HDRM is ideally optimized for the characterization of local structures and short-range order from diffuse scattering in single crystal samples and thin films.

5.2 Reciprocal Space Analysis

We begin with describing our qualitative analysis of the processed data collected by the area detector. To create a full 3D representation of reciprocal space, for each temperature point, the datasets were stacked using the known high-temperature space group $P6_3/mcm$. We conducted a systematic investigation of the HK and HL (and KL) planes at various temperatures, spanning above, below, and through the transition temperature T_V. Our search focused on periodic changes in the Bragg peaks, including shifts, splittings, and absences, as indicators of a structural transition. We also looked for superlattice peaks, which would signal superstructures, as well as weak, broad peaks and rod or sheet-like behaviour, characteristic of diffuse scattering.

The detected signal was initially plotted on a logarithmic scale, allowing observation of the entire range of scattered intensity, reaching up to 10^5 counts. This scale is suitable for viewing the highest intensity structural peaks in reciprocal space, as they are seen as distinct, high-intensity points. Fig. 5.1 shows examples of 2D HKL cuts at 100 K vs 300 K, specifically HK planes at $L = 0, 1, 2, 3$. For all investigated HK and HL planes, including the examples shown as well as planes with non-integer H, K, and L values, no periodic differences in the Bragg peaks were observed between the high and low-temperature datasets, apart from intensity variations qualitatively associated with the Debye-Waller factor, which gives higher intensities at lower temperatures. This confirms our observations from in-house XRD measurements, indicating no noticeable changes in the average structure of $Pb_3Rh_7O_{15}$.

The signal was then plotted on a linear scale, with the maximum intensity capped at 30 counts. This scale facilitates viewing weak features due to diffuse scattering effects. Fig. 5.2 shows the same examples of HK planes on this scale. In all inspected HK and HL planes, broad peaks at integer HKL positions are observed, suggesting the presence of short-range structural correlations in the sample. However, these peaks exhibit no periodic differences between the two temperatures, aside from variations that can be qualitatively attributed to the Debye-Waller factor and thermal phonons (not shown here). Moreover, no rod or sheet-like scattering is observed at this scale either.

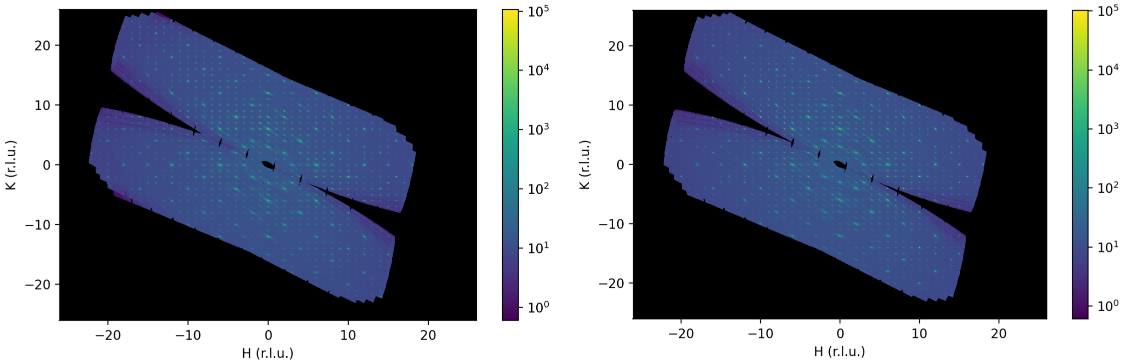

(a) 100K L=0 (b) 300K L=0

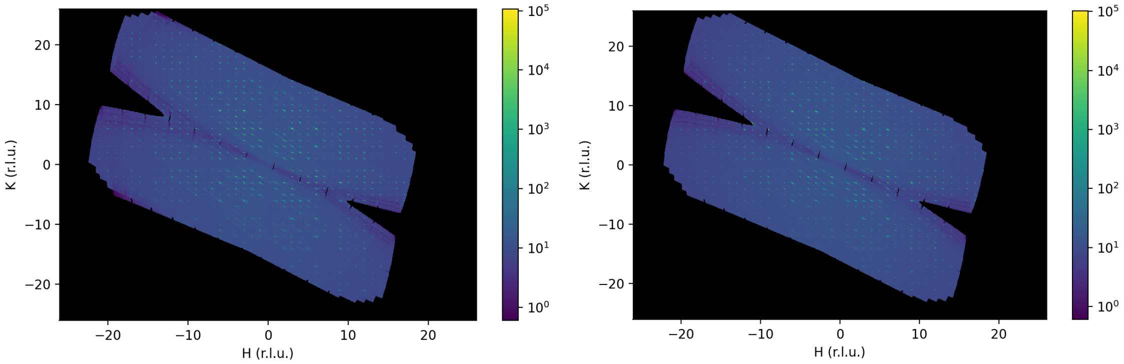

(c) 100K L=1 (d) 300K L=1

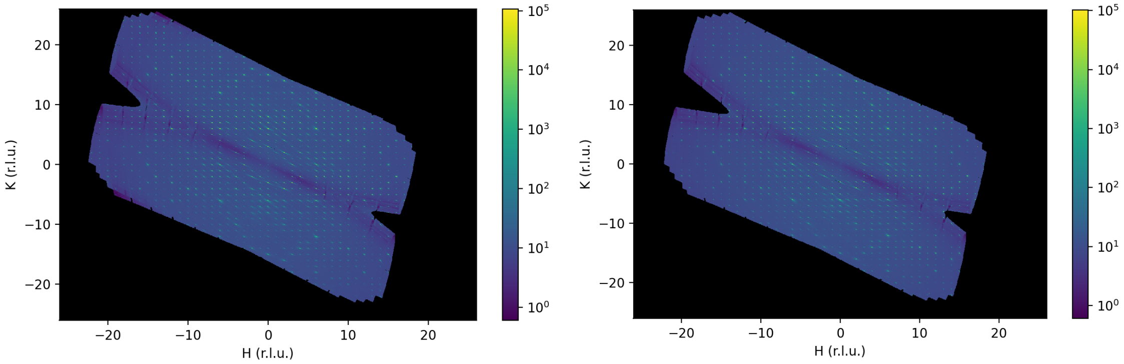

(e) 100K L=2 (f) 300K L=2

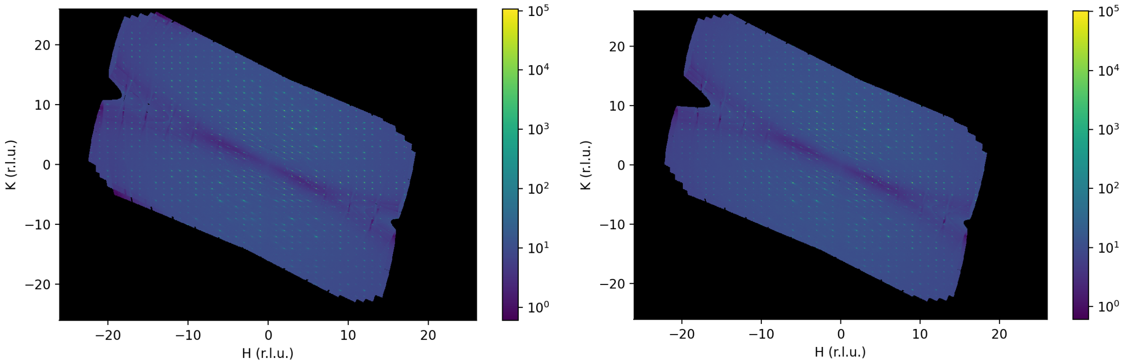

(g) 100K L=3 (h) 300K L=3

Figure 5.1: Comparison between HDRM 2D cuts at 100K and 300K (Log Scale).

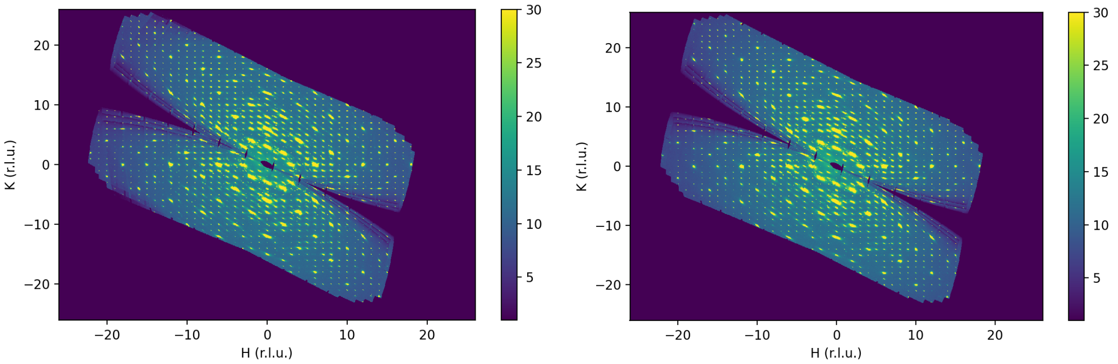

(a) 100K L=0 (b) 300K L=0

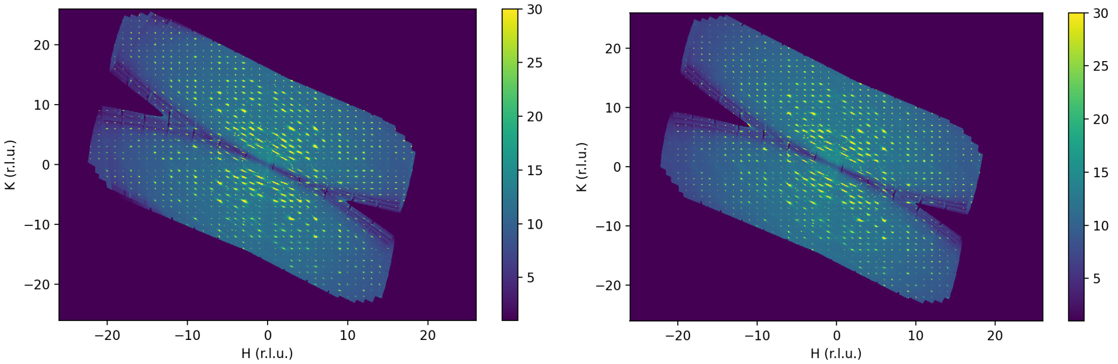

(c) 100K L=1 (d) 300K L=1

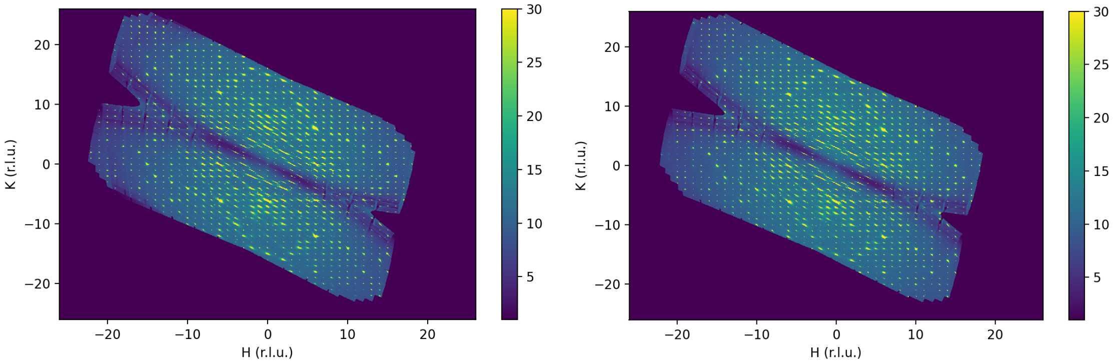

(e) 100K L=2 (f) 300K L=2

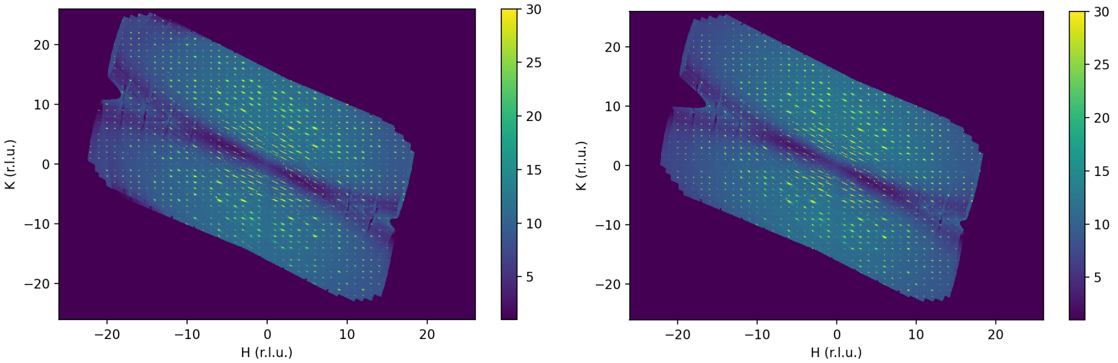

(g) 100K L=3 (h) 300K L=3

Figure 5.2: Comparison between HDRM 2D cuts at 100K and 300K (linear scale, 30 counts).

For a more quantitative comparison of features in reciprocal space at different temperatures, we integrated the intensity over specific peaks to obtain 1D linecuts. The choice of peaks was guided by the simulated powder diffraction results, shown in Fig. 5.3, calculated using our refined high-temperature $P6_3/mcmc$ and low-temperature $P6_3cm$ and $P\overline{6}c2$ structures from Chapter 4. From these patterns and comparisons, no new peaks are observed between the high and low-temperature structures. The largest intensity differences tend to result from slight shifts in 2θ at the peaks, found at $2\theta \approx 26.86°$, $27.16°$, $32.03°$, $32.86°$, $37.28°$, $54.56°$, corresponding, respectively, to the $P6_3/\mathrm{mcm}$ HKL reflections of 004, 211, 114, 302, 222, 421. When comparing the two low-temperature structures, the differences are subtle, with the spectra showing no new peaks, only slight shifts in 2θ or variations in relative intensity, often on the order of a single count. The most "significant" differences in intensity between $P\overline{6}c2$ and $P6_3cm$ are observed at $2\theta \approx 18.38°$, $26.47°$, $26.83°$, $38.05°$, $65.8°$, which are respectively associated to the $P6_3/\mathrm{mcm}$ HKL reflections of 111, 113, 004, 115 and 119.

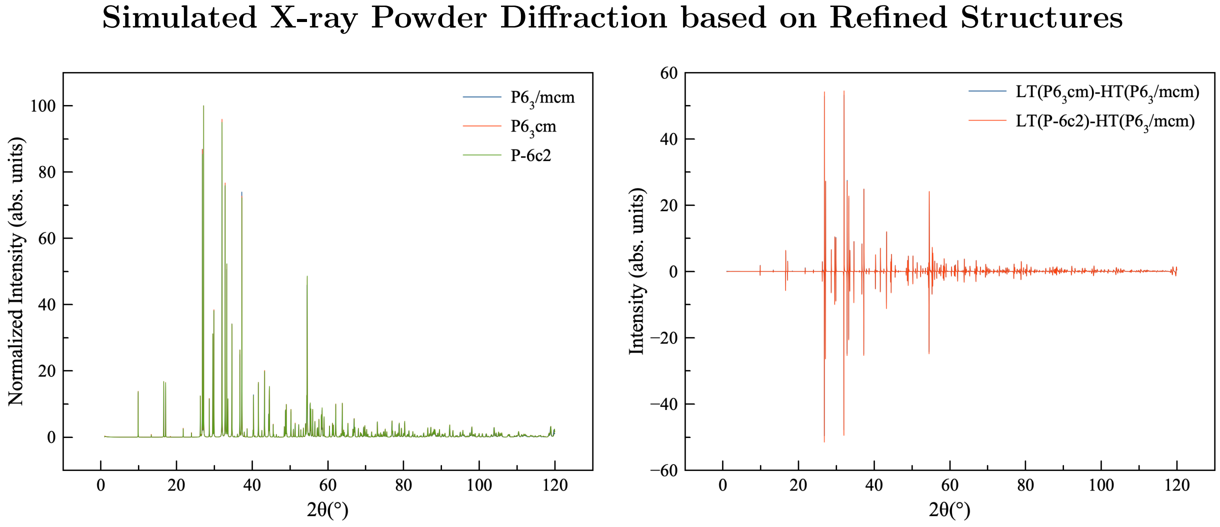
Simulated X-ray Powder Diffraction based on Refined Structures

(a) (b)

Figure 5.3: a) Simulated X-ray powder diffraction spectra using Vesta for high (297K) and low (110K) temperature structures of $Pb_3Rh_7O_{15}$. b) Subtraction of high temperature spectrum from the low temperature spectra.

Fig. 5.4 shows the integrated intensity of the (004) diffraction peak, chosen as an example that is predicted to present significant differences in the high and low-temperature diffraction patterns. From the simulated spectra, the lowest temperature is expected to have highest intensity. Moreover, the calculated reflection values give $2\theta = 26.8317°$ and $2\theta = 26.8544°$ in the high and low-temperature space groups, respectively, which would result in a shift to the right in reciprocal space as the temperature is decreased. However, no systematic, temperature-dependent shift in 2θ or variation in intensity is observed in the plotted data.

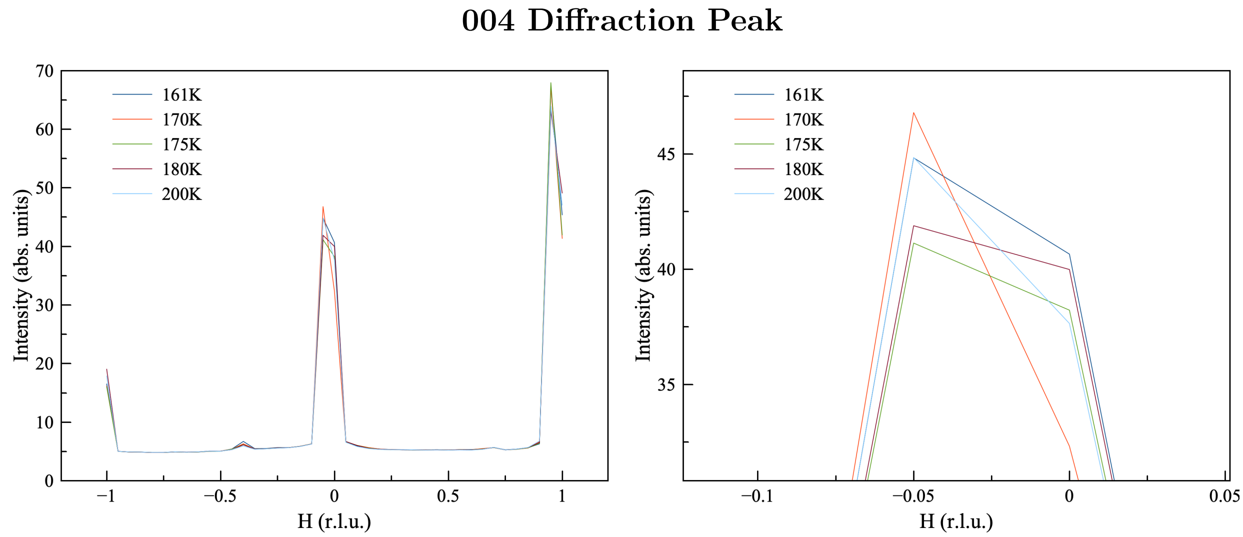

004 Diffraction Peak

(a) (b)

Figure 5.4: a) Intensity of (004) diffraction peak, integrated along K and L at different temperatures spanning the transition. b) Close-up of the (004) peak.

Fig. 5.5 shows the (111) reflection, an example of a weak diffraction peak presenting a slight intensity difference in the two low-temperature powder diffraction spectra. The peak in $P\overline{6}c2$ is predicted to have similar scattering intensity as the peak in $P6_3/mcm$, whereas in $P6_3cm$, it is expected to have slightly higher intensity. For both low-temperature spectra, $2\theta = 18.3894°$, compared to $2\theta = 18.3828°$ in the high-temperature $P6_3/mcm$ pattern, which should result in a subtle shift of the peak to the right in reciprocal space below the transition temperature T_V. Instead, as observed in the (004) peak, no systematic differences are apparent based on whether the temperature is above or below the transition.

For both of these peaks, as well as all other reflections listed in this section, no temperature dependent differences in reciprocal space are observed, which could be due to limitations in resolution, as made evident by the insufficient point density seen in Fig. 5.4 and Fig. 5.5. The simulated diffraction profiles show that the differences between the spectra of the high and low-temperature structures manifest as slight peak shifts in 2θ and subtle variations in relative intensities. Due to the high intensity of the incident X-ray beam, the Bragg peaks become saturated. Therefore, synchrotron measurements are less optimized for measuring relative peak intensities than in-house single crystal XRD. However, the combination of low noise with high sensitivity to low counts makes HDRM measurements well-suited for detecting diffuse scattering. Despite these capabilities, the HKL datasets indicate no obvious signs of transition-driven structural distortions due to short-range correlations, suggesting that any differences, if present, would be subtle.

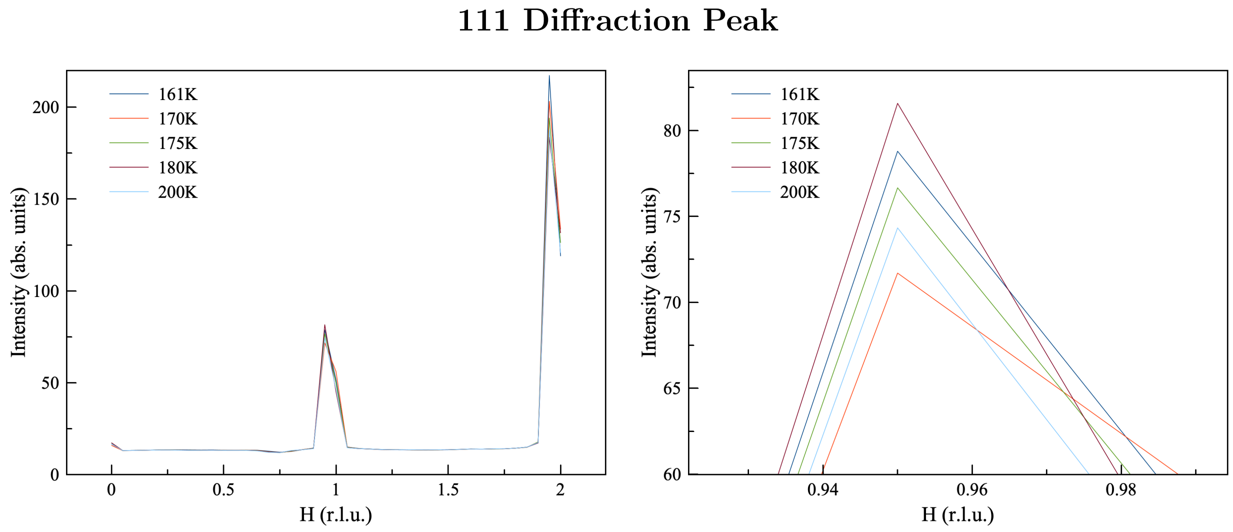

(a)
(b)

Figure 5.5: a) Intensity of (111) diffraction peak, integrated along *K* and *L* at different temperatures spanning the transition. b) Close-up of the (111) peak.

5.3 3D-Δ PDF Analysis

The final analysis method we turn to for investigating the local structural environment in $Pb_3Rh_7O_{15}$ is the three-dimensional difference pair distribution function (3D-Δ PDF), a powerful technique for studying diffuse scattering. This method is relatively new, with its development previously limited by insufficient data resolution and computational power.

5.3.1 Background Theory

3D-Δ PDF is based on the "punch and fill" principle, which refers to removing Bragg peaks from the total scattering pattern, therefore removing scattering due to the average structure, and then "filling" the resulting voids by extrapolating surrounding weak scattering signals. This pattern is then Fourier transformed to reveal diffuse scattering in direct space, i.e., features of the real structure that are not described by the average structure [42]. The resulting 3D-Δ PDF maps show intensities as a function of separation distances from the origin of the unit cell in direct space. Positive values in 3D-Δ PDF maps are associated with a higher probability of finding scattering densities separated by their corresponding interatomic vector than in the average structure; negative values indicate lower probabilities. The longest separation vector gives the correlation length of local order, which corresponds to the length and direction that a local feature influences its surrounding environment. The magnitude of the observed 3D-Δ PDF intensities reflects the strength of pair correlations, which depends on a combination of factors involving the scattering power of the elements in the atomic pair, the multiplicity of the separation vector, and the contrast between the average structure and its weak features.

5.3.2 Results

3D-Δ PDF maps were examined at various temperatures between 100 K and 300 K. To calculate the 3D-Δ PDF intensities, the Bragg peaks were removed from the total scattering using a punch radius of 0.2 Å in real space, corresponding to a radius of $(2\pi)/0.2$ Å^{-1} in reciprocal space. The resulting 3D-Δ PDF maps display PDF intensities in direct space as a function of number of unit cells. The origin in these maps corresponds to the origin of the unit cell, which remains unchanged above and below T_V due to the shared hexagonal symmetry of the high and low-temperature space groups.

Fig. 5.6 shows the fully integrated 3D-Δ PDF intensities along the z and y directions for several temperatures spanning the transition. All signals share peaks at the same separation distances and exhibit similar peak intensities and lineshapes. Upon closer examination of the peaks, subtle intensity variations become apparent; however, these changes appear to be random, showing no systematic dependence on whether the temperature is above or below T_V. Plotting these collapsed intensities reveals no obvious initial differences between the datasets at different temperatures.

Fig. 5.7 presents examples of 2D-Δ PDF cuts at 100 K and 300 K, with $z = 0, 1, 2, 3$. Fig. 5.7a and Fig. 5.7b show diffuse scattering along the (110) axis, however the pattern as well as the correlation length remain the same for both 100 K and 300 K. Relating this signal to the refined structure and proposed charge ordering scheme, one might expect some temperature-dependent differences on either side of this axis. These differences would be anticipated at $|x| < 1$, corresponding to the approximate position of the mixed-valent Rh2 sites. However, no such differences are observed. Moreover, no temperature-dependent periodic distinctions are observed in any of the other investigated planes, at varying temperatures and non-integer z-values. This confirms our previous observations from reciprocal space analyses.

Integrated 3DΔ-PDF Intensity Comparison at Different Temperatures

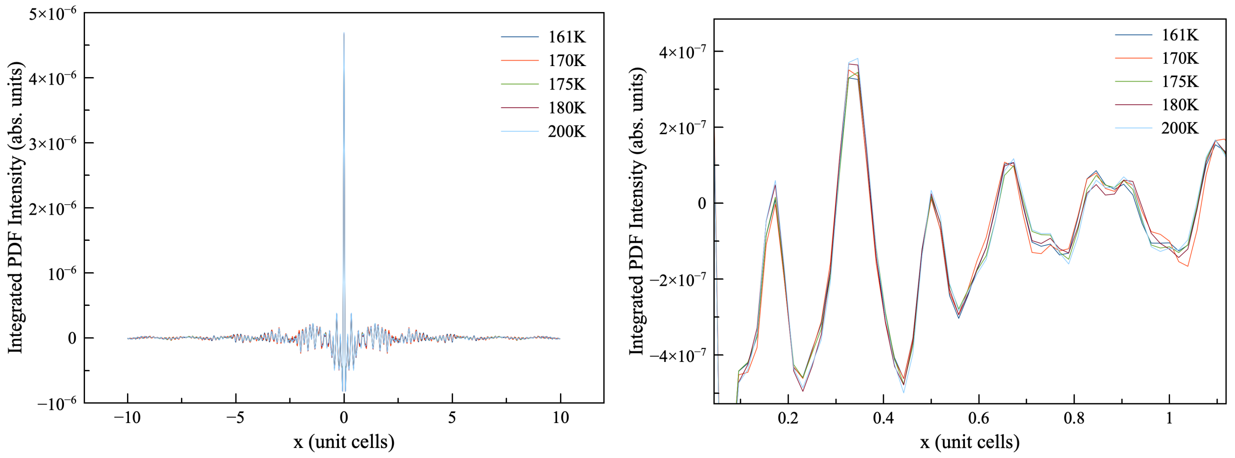

(a) (b)

Figure 5.6: a) 3D-Δ PDF intensities at different temperatures, integrated along z and y directions. b) Close-up of the first unit cell, highlighting the most notable differences observed across the temperature datasets spanning the transition.

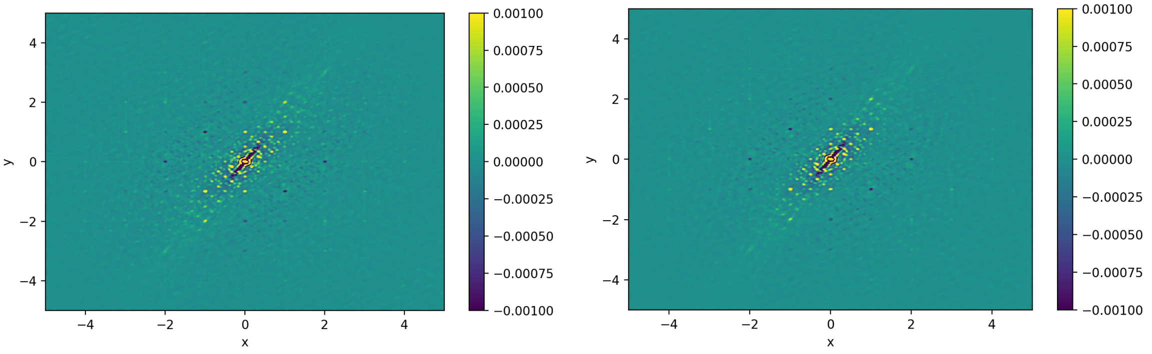

(a) 100K z=0 (b) 300K z=0

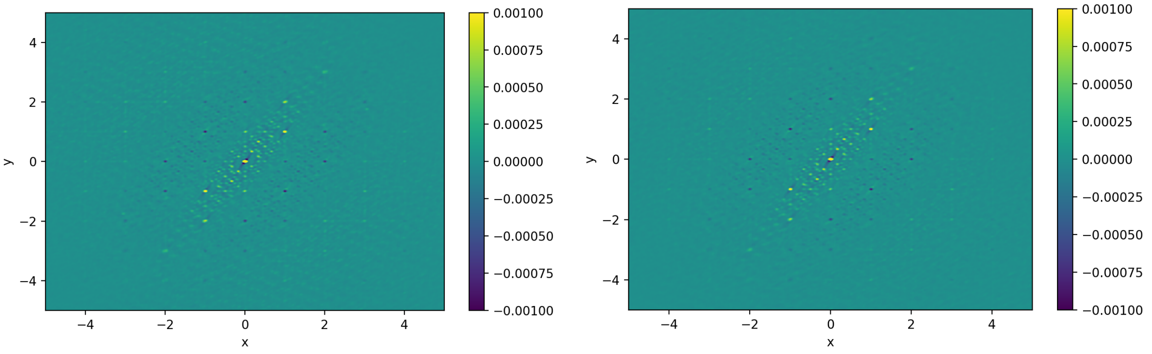

(c) 100K z=1 (d) 300K z=1

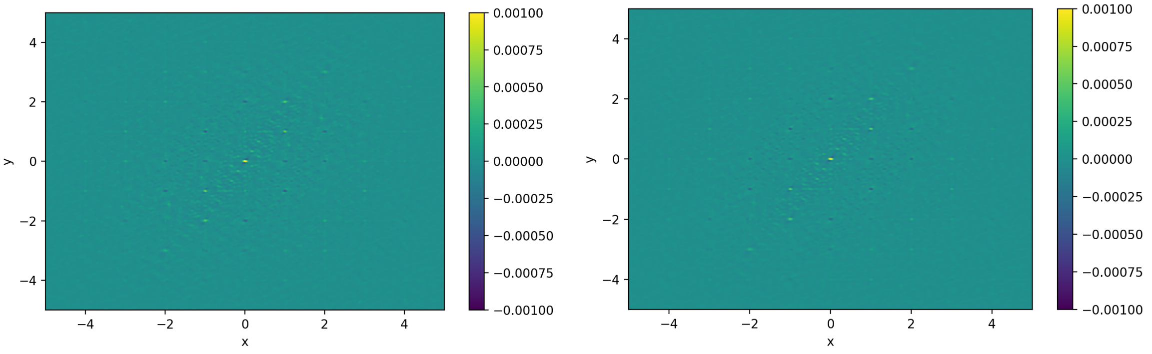

(e) 100K z=2 (f) 300K z=2

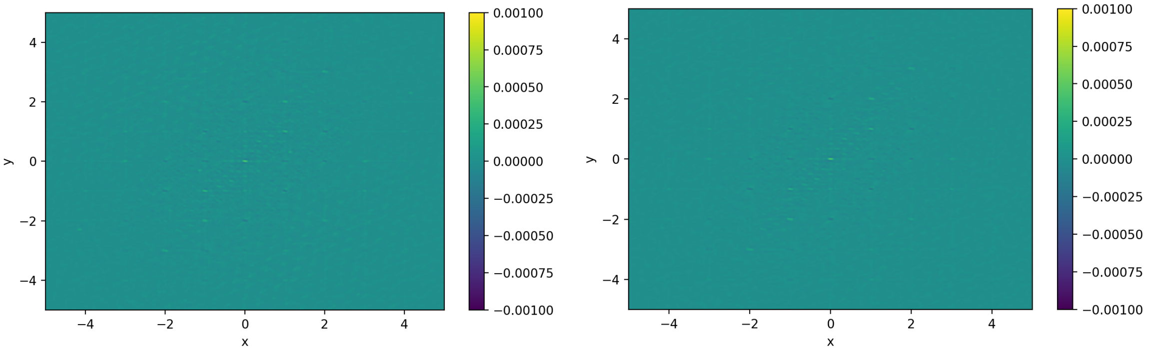

(g) 100K z=3 (h) 300K z=3

Figure 5.7: Comparison Between 3D-Δ PDF 2D Cuts at 100K and 300K.

In summary, our HDRM analyses show no evidence of diffuse scattering specific to the insulating phase of $Pb_3Rh_7O_{15}$. Therefore, this technique provides no additional structural evidence suggesting electron delocalization or more complex charge ordering behaviour in the local structural environment of the system.

Chapter 6

Local Electronic Environment Analysis using XAS

Following our average and local structural analyses in chapters 4 and 5, we continue investigating charge ordering in $Pb_3Rh_7O_{15}$ by studying the average electronic structure of the Rh cations using X-ray absorption spectroscopy (XAS). In this chapter, we present results from our XAS experiment at the PIPOXS beamline, as well as our subsequent analysis, which includes mathematical fitting and FDMNES modeling of the spectra.

6.1 XAS Background Theory

X-ray absorption spectroscopy is a technique used to characterize the chemical composition, electronic structure, and site symmetry of a wide range of compounds. XAS is an element-specific technique, determined by the selection of the incident X-ray energy. It is typically performed at synchrotron sources, which provide a broad range of X-ray energies suitable for most elements in the periodic table. The basic principle of XAS involves using the incident X-ray energy to excite an element's core-level electrons from their ground states to their unoccupied excited states, relying on transitions associated with X-ray absorption [43]. In the XAS spectrum, this appears as a sharp increase in absorption at a specific X-ray photon energy, characteristic of the absorbing element. This energy is referred to as the absorption edge and corresponds to the energy required to eject a core electron into an excited state or the continuum, while the sharp feature immediately above this energy is known as the white line. The region of the spectrum near the absorption edge is known as the X-ray absorption near-edge structure (XANES) region. When the electron to be excited originates from the $1s$ core level, the absorption edge is referred to as the K-edge and corresponds to the transition from the $1s$ orbital to the lowest unoccupied np orbital. If the incident energy is tuned to excite electrons from the $2s$ or $2p$ levels, this corresponds to the L absorption edges, where electrons transition to the first available np or nd levels, respectively. Therefore, XAS provides information about the local electronic environment of a specific element by probing the density and geometry of the unoccupied electronic states closest to the Fermi energy.

The range extending approximately 1 keV beyond the absorption edge is known as the extended fine structure region (EXAFS). At these higher energies, the absorption spectrum is due to the backscattering of the emitted photoelectrons with the ions located in the first coordination shell of the cation from which the photoelectrons originate. Therefore, the EXAFS region is sensitive to the local structural environment of the element of interest. However, EXAFS require a higher signal-to-noise ratio than XANES scans, as the size of the variations in the spectrum due to these backscattering effects can be comparable to the noise in the data. Even under optimal conditions, it remains a complimentary technique to refinement. For these reasons, this technique lies beyond the scope of our current work.

It is important to note that XAS is an element-specific, not a site-specific, technique, as the incident energy excites metal cations at all crystallographic sites within the lattice. Consequently, the resulting energy spectrum reflects the average of all local electronic environments of the metal cations. In the context of charge order, searching for differences in the energy spectrum above and below the transition temperature corresponds to detecting changes in the local environments of the metal cations that contribute to variations in this average.

Additionally, the XAS spectrum is sensitive to the oxidation state of the element, which is seen as an energy shift in in the rising edge of the white line. In a higher oxidation state, electrons are more tightly bound to the core, which increases the absorption energy required to excite an electron from an orbital. Conversely, in lower oxidation states, the opposite is true, as the increased negative charge surrounding the core reduces the absorption energy, shifting the white line to lower energies.

Traditionally, XAS measurements are collected in transmission mode, where the intensity of the XAS signal is given by the normalized difference between the incident and the transmitted beam intensities over a range of absorption energies. In this setup, core-hole lifetime broadening is significant and causes smearing of features in the XANES region of the spectrum. This energy broadening is reduced when the X-ray absorption spectrum is measured indirectly using the intensity of the emitted X-ray fluorescence, tuned to a specific emission line. The resulting spectra, referred to as high-energy resolution fluorescence-detected XANES (HERFD-XANES) [44] offer higher resolution than the spectra obtained in transmission mode, allowing for better detection of subtle features.

6.2 Experiment

Our analysis of the local electronic environment of Rh in $Pb_3Rh_7O_{15}$ is based on results from HERFD-XAS measurements performed at the PIPOXS (Photon-In, Photon-Out X-ray Spectroscopy) beamline at CHESS, which is dedicated to studying the geometric and valence electronic structures of quantum materials. In our experiment, the incident X-ray energy was set to the Rh K-absorption edge, at 23.22 keV.

As shown in Fig. 6.1, the electronic structure of Rh is described by the $[\mathrm{Kr}]4d^8 5s^1$ configuration. The K-edge energy corresponds to the transition of the innermost core $1s$ electron to the first available np state, which is the $5p$ orbital in Rh.

The choice of this edge is justified by two main arguments. Firstly, p orbitals are not strongly involved in bonding interactions; instead, the energy and density of the unoccupied np states depend on the local geometry and electrostatic effects in the first coordination shell of the metal cations. Therefore, these states are highly sensitive to variations in the oxidation

Rh **Electronic Structure.**

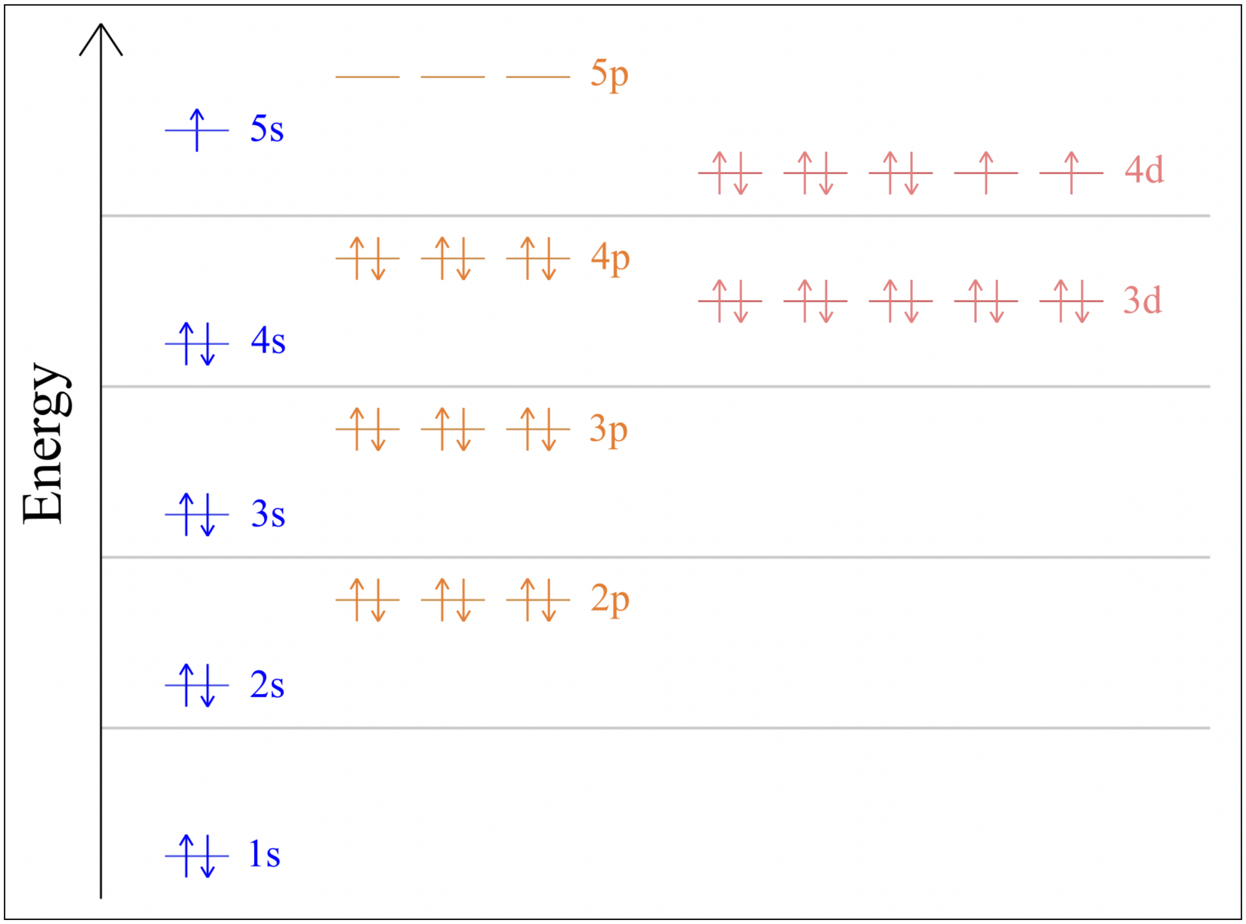

Energy not to scale. Electronic structure of ^{45}Rh shown as [Kr]$4d^8 5s^1$. The $4d$ orbitals are lower in energy than the $5s$ orbital, giving Rh^{3+} and Rh^{4+} the configurations [Kr]$4d^6$ and [Kr]$4d^5$, respectively, shown below.

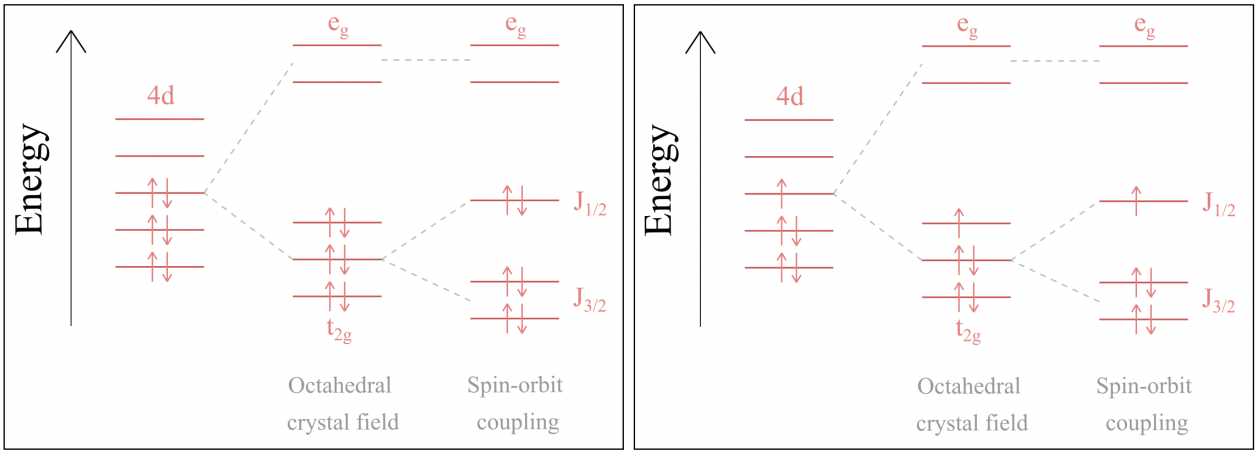

(a) $4d^6$-orbital configuration of Rh^{3+}

(b) $4d^5$-orbital configuration of Rh^{4+}

Figure 6.1: Splitting of the $4d$ orbitals of Rh^{3+} and Rh^{4+} into e_g and t_{2g} manifolds due to the octahedral crystal field, with additional splitting of the t_{2g} levels in the presence of spin-orbit coupling.

states of surrounding atoms, making the K-edge ideal for detecting charge order. In contrast, the L-edges involve transitions to the *nd* orbitals, which participate in covalent bonding and hybridization. These effects result in larger contributions to the XAS spectrum, which could potentially obscure subtle features due to charge order.

The second reason for this choice of absorption energy is related to experimental considerations. The PIPOXS beamline operates in the hard X-ray regime, with an available energy range of 4.0 keV to 58 keV. The Rh K-edge lies within this range, with an absorption energy of approximately 23.22 keV [45], whereas all L-edges are at approximately 3 keV [45], situated within the tender X-ray regime and below the energy capabilities of the beamline.

6.2.1 PIPOXS Experimental Setup

A single $Pb_3Rh_7O_{15}$ crystal was secured in an aluminum holder using Kapton tape loaded with boron nitride powder (BN). The crystal was positioned near the aluminum frame for thermal contact, with the boron nitride ensuring thermal equilibrium within the holder. The sample environment consisted of a Displex cryostat, providing temperature control via a coldfinger. Measurements were performed at various temperatures between 20 K and 300 K. A Si(311) monochromator with a 7.0 keV to 58 keV energy selection range was used for continuous monochromator "flyscanning". This novel technique allowed for rapid data collection despite the necessary removal of focusing Rh coated mirrors. For a greater resolution of 1 eV, measurements were conducted in HERFD-XAS mode at the Rh Kα1 emission energy, with an incident energy ranging from 23.21 keV to 23.24 keV, which was calibrated using pure Rh metal. The resulting fluorescence was detected using a Pilatus 100K detector.

6.2.2 Results

The first results we present establish the average oxidation state of Rh in the $Pb_3Rh_7O_{15}$ single crystal sample. Fig. 6.2 shows a comparison between the HERFD-XAS spectra of $Pb_3Rh_7O_{15}$, Rh_2O_3 and Sr_2RhO_4. The two latter compounds exhibit, respectively, Rh^{3+} and Rh^{4+} nominal valences, and therefore serve as reference samples for these oxidation states. As mentioned previously in this section, information about the oxidation state of the metal cation can be extracted from the absorption energy at the leading edge of the white line feature, rather than from its peak position. This is seen in Fig. 6.2c, which presents an energy difference of approximately 3 eV between the leading edges of the Rh_2O_3 and Sr_2RhO_4 spectra. As expected, the lower Rh^{3+} oxidation state presents a lower absorption energy compared to Rh^{4+}. The leading edge associated with $Pb_3Rh_7O_{15}$ lies between these energies, thus confirming the mixed-valent nature of the compound.

The next set of measurements are shown in Fig. 6.3, which consists of Resonant X-ray Elastic Scattering (RXES) planes collected above and below the transition temperature T_V, at 300 K and 100 K. These RXES planes display signal intensity as a function of incident energy (XAS) and emitted energy (XES). XES refers to the energy emitted as electrons transition from higher to lower energy states, filling the core hole resulting from the initial energy excitation. XES is therefore used to study the relaxation processes following photon

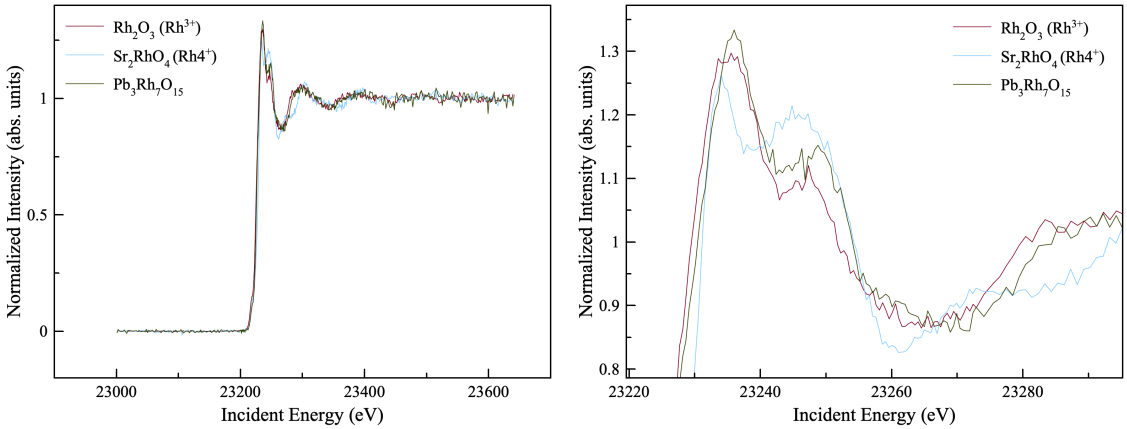

(a) Full data range.

(b) Closer look at white line features.

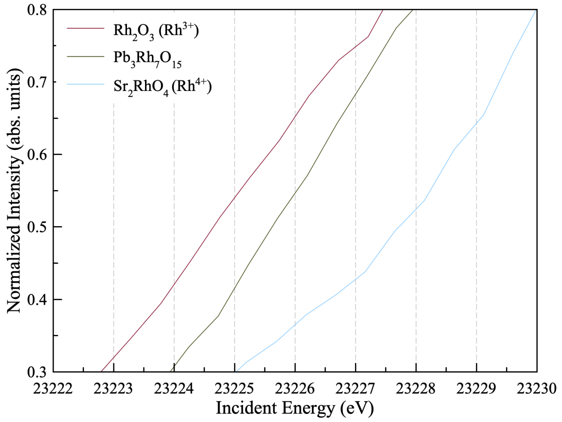

(c) Leading edges of the three spectra.

Figure 6.2: Comparing HERFD-XAS spectrum of $Pb_3Rh_7O_{15}$ to spectra of the Rh^{3+} and Rh^{4+} reference samples, Rh_2O_3 and Sr_2RhO_4.

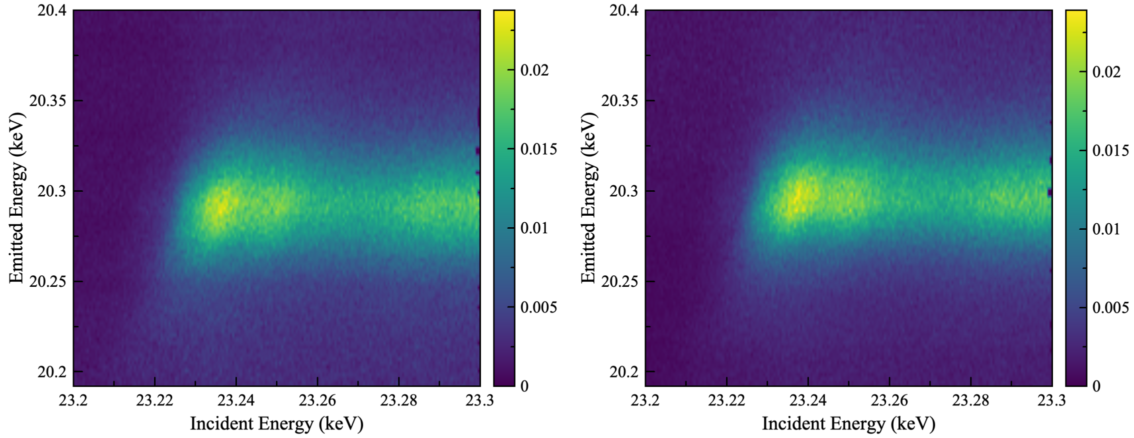

(a) 100K

(b) 300K

Figure 6.3: RXES Planes of $Pb_3Rh_7O_{15}$ at 100K and 300K.

absorption, which also provides information about the local electronic environment of the metal cation. In both Fig. 6.3a and Fig. 6.3b, the lobe at the lowest incident energy corresponds to the white line due to the transition of electrons from the 1s to 5p orbitals. The following intensity features are fine structure contributions, which have comparable intensities to the white line - a characteristic of the K-edge.

These figures offer an initial qualitative comparison between the $Pb_3Rh_7O_{15}$ energy spectra above and below the transition temperature. At this resolution, the two planes exhibit similar intensities and energy spread, with no apparent differences in their overall features. For greater resolution, subsequent HERFD-XAS measurements were performed over a similar absorption energy range, fixed at the most intense emission energy, shown here to be at approximately 20.3 keV. Fig. 6.4 presents examples of selected temperatures above and below T_V of these $Pb_3Rh_7O_{15}$ HERFD-XAS spectra. For each temperature, the energy profile comprises approximately ten averaged runs, which were normalized using Athena. In Fig. 6.4a, a comparison of the full range of the spectra shows no evident temperature dependent differences in the extended structure.

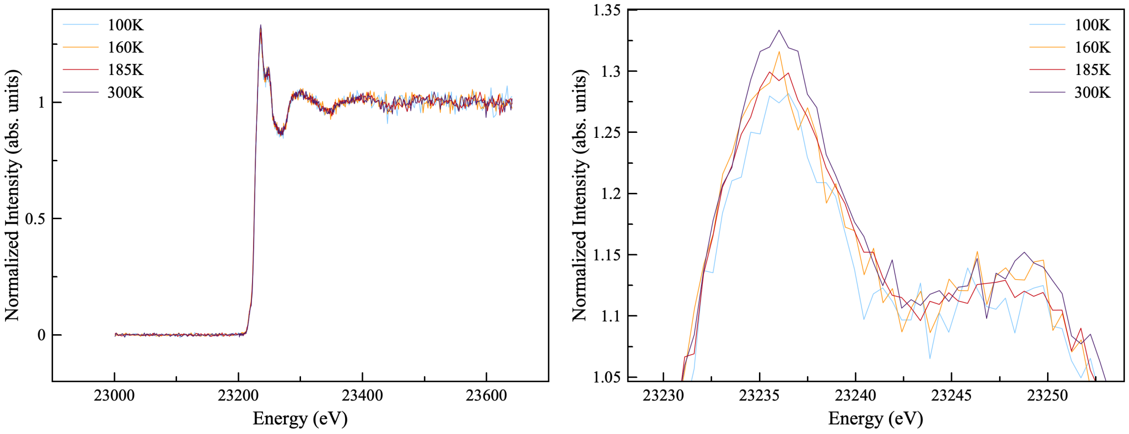

(a) Full spectrum range.

(b) Closer look at the white line features.

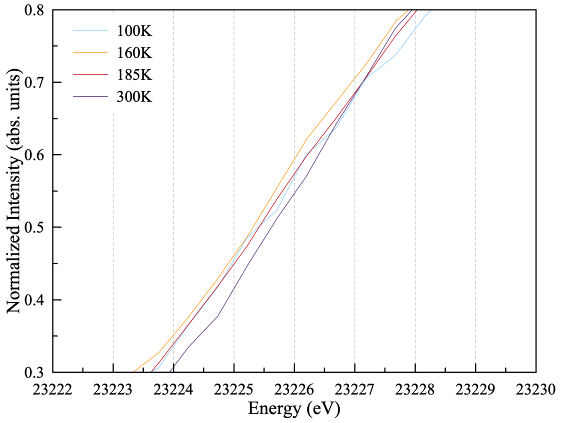

(c) Leading edges at each temperature, on the same scale used in Fig. 6.2c.

Figure 6.4: Temperature Comparison of $Pb_3Rh_7O_{15}$ HERFD-XAS Spectra.

In Fig. 6.4b, a closer look at the XANES region reveals noise in the data, as well as differences in peak intensity between datasets. However, these variations do not show any systematic dependence on the temperature relative to T_V. Finally, Fig. 6.4c presents no significant differences in the leading edge energies either, as the observed variations fall below the 1 eV resolution limit of the signal.

Following these qualitative comparisons, a quantitative analysis of the HERFD-XAS spectra was performed using mathematical fitting, as shown in Fig. 6.5. Specifically, the energy step was fit using an *arctan* function, setting the pre-edge intensity to 0 and the post-edge intensity to 1. The function was then adjusted to baseline the data. The isolated XANES region was fit using a combination of Lorentzian and Gaussian functions. These were chosen since Lorentzians are commonly used to describe white line features associated with electron transitions, while Gaussians are also used to account for broadening effects due to instrumental resolution. The lowest energy peak, corresponding to the white line, exhibits asymmetry, a characteristic feature of K-edge absorption spectra. This was fit using the sum of a Lorentzian and Gaussian. The second peak, corresponding to the lowest energy fine-structure feature, was fit using a Gaussian. The sum of these three functions determines the final fit used to model all temperature datasets, referred to as the Fit Sum in Fig. 6.5. Among all the temperature datasets studied, the lowest coefficient of determination R^2 was

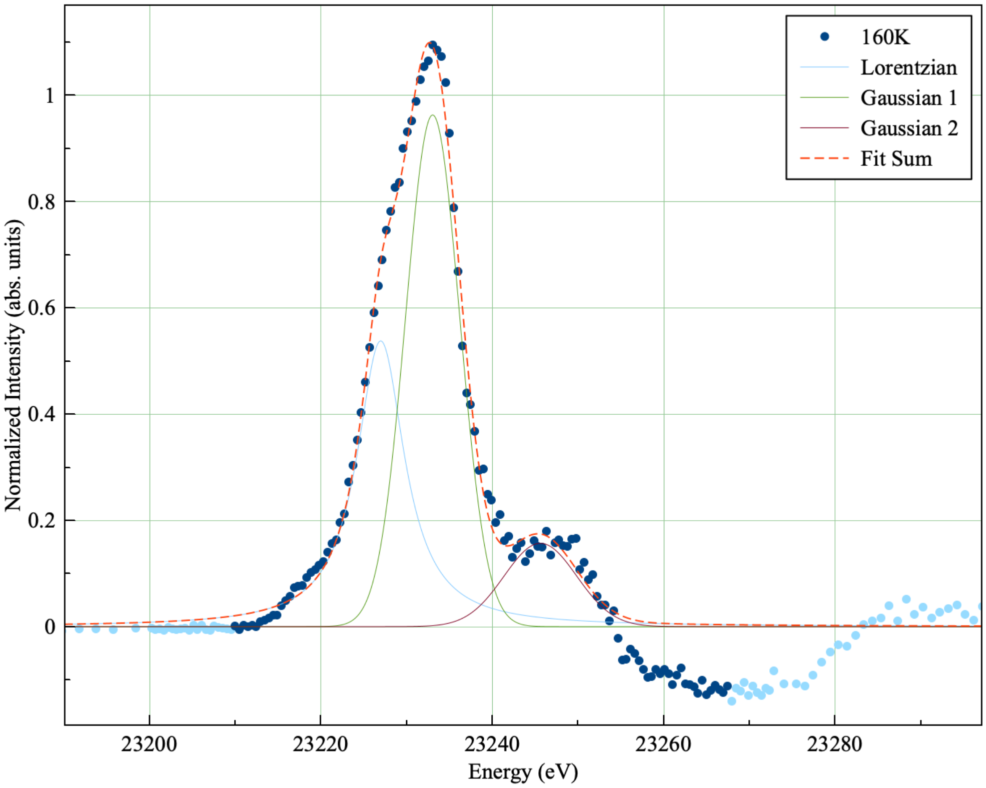

Figure 6.5: Fitting $Pb_3Rh_7O_{15}$ HERFD-XAS Spectra. Example showing fitting of spectrum corresponding to $Pb_3Rh_7O_{15}$ 160K dataset, using one Lorentzian and two Gaussians functions.

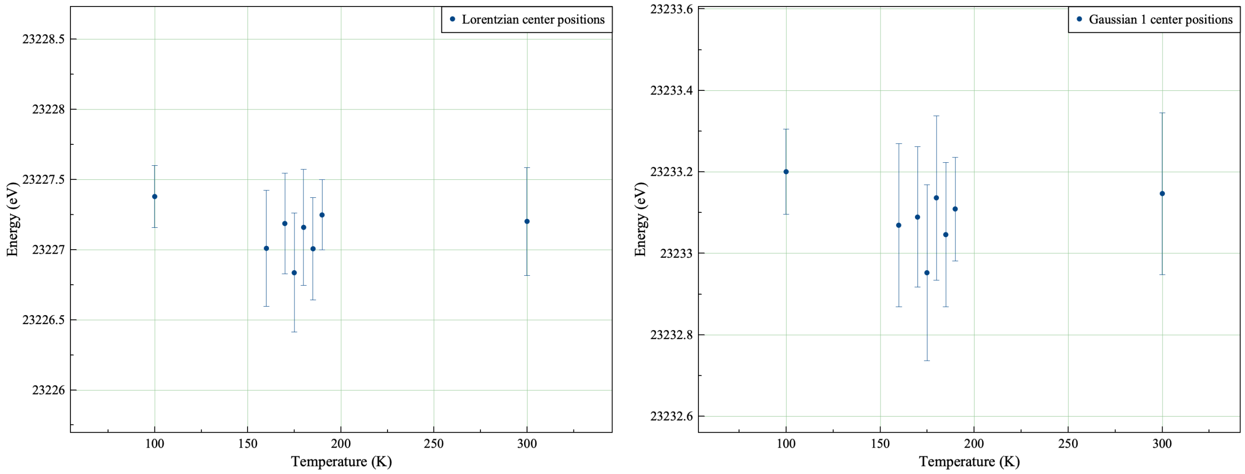

(a) Lorentzian (b) Gaussian 1

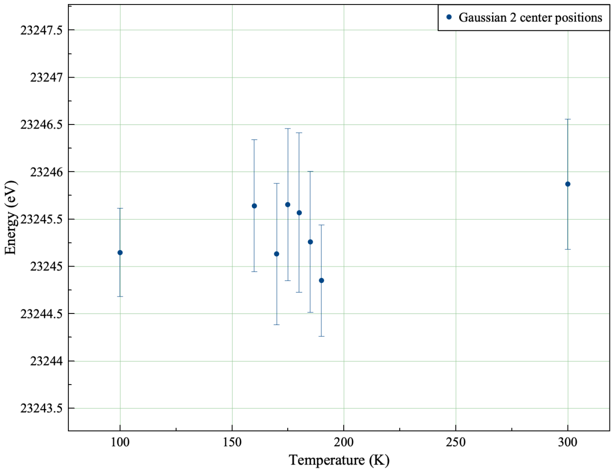

(c) Gaussian 2

Figure 6.6: Temperature Comparison of Extracted Fit Parameters. Center Positions of Lorentzian (a), Gaussian 1 (b) and Gaussian 2 (c) functions.

found to be 0.9676 with an adjusted R^2 value of 0.9654, for the $T = 175$ K dataset, while the highest R^2 value was 0.9933, with an adjusted R^2 value of 0.9928 at $T = 100$ K. For all fits, R^2 and adjusted R^2 values are similar, suggesting that the obtained models describe the data accurately without overfitting and that the associated independent parameters are meaningful predictors of the observed spectral features. Consequently, the extracted parameters from these fits provide a reliable basis for comparison between temperature datasets. In our analysis, the selected parameters are the peak positions, with associated uncertainties, of each function included in the fit sum. Fig. 6.6 compares these extracted center positions across all temperature datasets. No significant temperature-dependent differences are observed for any of the three peaks, supporting our qualitative analyses.

6.3 FDMNES

6.3.1 Theory

FDMNES (Finite Difference Method Near Edge Structure) [46] is a computational code commonly used for simulating single-photon processes, such as X-ray absorption (XAS) and X-ray emission spectroscopy (XES), near elemental K and L-absorption edges. This code is based on first-principles methods derived from density functional theory (DFT). It is capable of calculating transition cross sections between core and unoccupied electron states for all chemical elements, ranging from hydrogen to the heavier actinides.

The local environment of the absorbing atom is considered through a cluster approach, where the calculation volume is defined by a sphere with a radius typically ranging from 4 Å to 7 Å. The FDMNES intensity is calculated for atoms in their surrounding cluster. The total signal is obtained by summing over all equivalent sites, as determined by the characteristic symmetry operations of the corresponding space group, followed by summing over all inequivalent crystallographic sites. Relative energy shifts resulting from different oxidation states are accounted for automatically.

The calculation can be performed using the finite-difference method (FDM) or multiple-scattering theory (MST). In FDM, the spatial domain is divided into a grid, allowing for spatial derivatives to be approximated as finite differences, therefore facilitating high precision calculations. Meanwhile, in MST, potentials are approximated as muffin-tin potentials, resulting in significantly shorter compilation times.

6.3.2 Results

Through trial and error, the simplest FDMNES model describing the XAS $Pb_3Rh_7O_{15}$ spectrum at the K-absorption edge was found to be determined by the parameters listed in the first column of Tab. 6.1. In this model, defined by a minimum number of input parameters, the muffin-tin potential approximation is applied, and spin-orbit coupling and relativistic effects are not considered. The structural information about the compound is extracted from the cif files used in our previous analyses. These include the published high-temperature $P6_3/mcm$ structure from the Mizoguchi group, our rendition of the proposed $P\overline{6}c2$ structure, and our $P6_3/mcm$ and $P6_3cm$ high and low-temperature refinements.

The spectra from these four structures, simulated using this model, are shown in Figs 6.7a. and 6.7b. When compared across the full range, the spectra exhibit a broadly similar appearance, however a closer examination of the XANES region reveals slight variations between datasets. Both high-temperature spectra share similar lineshapes and intensities. However, the low-temperature $P\overline{6}c2$ spectrum predicts a higher intensity and less distinct separation between the two peaks immediately after the absorption edge compared to the $P6_3cm$ spectrum. Moreover, the spectra resulting from the proposed structures show greater variation, where the low-temperature structure exhibits a higher intensity and leading edge energy compared to the high-temperature structure. This is not observed in the experimental data, shown in Figs. 6.7e and 6.7f, where no significant difference is seen in the leading edge energies or peak intensities, as discussed in Section 6.2.2, which contradicts the relationship observed between the high and low-temperature spectra for the proposed structures.

Model 1: No Spin-orbit	**Model 2: Spin-orbit Included**
Empirical formula: Rh K-edge	Empirical formula: Rh K-edge
Cluster Radius = 6.00 Å	Cluster Radius = 6.00 Å
Dipole component	Dipole component
Quadrupole component	Quadrupole component
Non-relativistic	Relativistic
Non-magnetic	Non-magnetic with spin-orbit
MST (Green)	MST (Green)
$D_{\text{maxpot}} = 2.500$ Å	$D_{\text{maxpot}} = 2.500$ Å
Self-consistent	Self-consistent
Max number of iterations = 100	Max number of iterations = 100

Table 6.1: Selected FDMNES input parameters for models without and with spin-orbit coupling.

When comparing the spectra calculated from our refinements to the normalized PIPOXS data, an energy shift in the highest intensity peak, corresponding to the first peak after the absorption edge, becomes apparent. Specifically, this peak is 6.275 eV higher in energy in the high-temperature FDMNES spectrum than in the 300 K HERFD-XAS spectrum, and 6.017 eV higher in the low-temperature FDMNES spectrum than in the 100 K spectrum. When spin-orbit coupling is added to the FDMNES model, as described in the second column of Tab. 6.1, the energy difference is reduced to 3.795 eV between the two high-temperature spectra and 3.567 eV between the low-temperature profiles. Figs. 6.7c and 6.7a compare the spectra of the four structures calculated using this new model. All profiles show greater distinction between the two peaks immediately after the absorption edge. As observed in the first FDMNES model, the high-temperature spectra remain similar to each other. The $P\overline{6}c2$ profile once again deviates from the other spectra, exhibiting a higher leading edge energy and intensity, along with less distinction between the two peaks. Finally, as noted in the no spin-orbit model, the refinement spectra closely resemble one another, predicting no significant difference between the average local electronic environment of the Rh cations above and below T_V.

Fig. 6.8 compares the spin-orbit and no-spin-orbit FDMNES spectra calculated from our refined structures ($P6_3/mcm$ above T_V and $P6_3cm$ below T_V) with the 100 K and 300 K HERFD-XAS spectra. In these figures, the FDMNES spectra are artificially shifted to align with the peak position of the experimental data, facilitating comparisons of lineshape and intensity. From this analysis, the spin-orbit FDMNES model most closely resembles the experimental data for both high and low temperatures, as it produces a spectrum with white line and fine structure features that are more distinct due to their more accurate relative intensities. This result, along with the smaller energy difference between the simulated and experimental spectra, suggests that spin-orbit coupling should be considered. However, some discrepancies remain between the spin-orbit FDMNES and experimental spectra (3 eV shift, underestimated first peak intensity, etc.). For a more accurate description of the experimental data, additional input parameters should be incorporated into the FDMNES calculation. This may suggest the presence of additional effects and mechanisms beyond charge order that

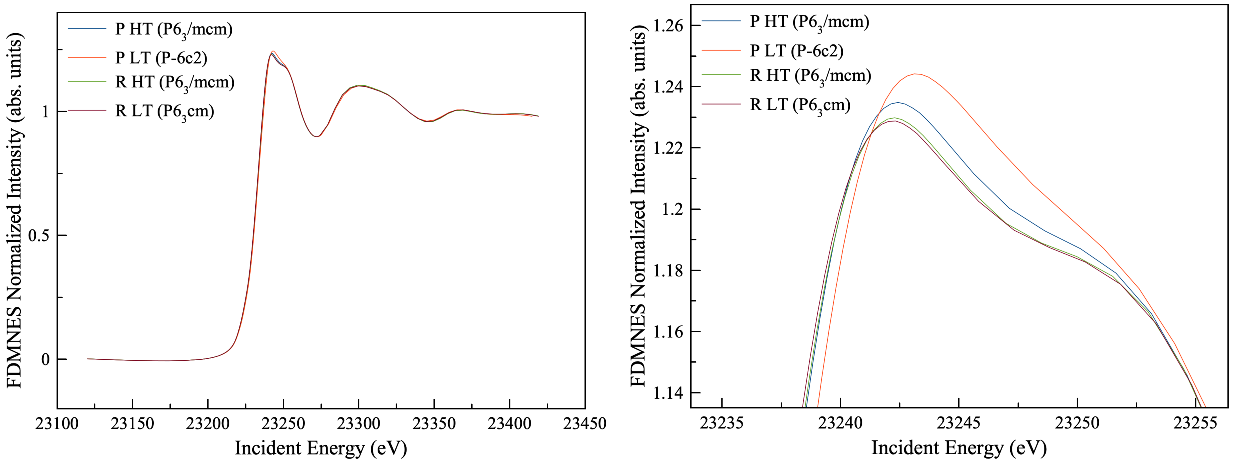

(a) FDMNES (No SO), full data range. (b) FDMNES (No SO), white line features.

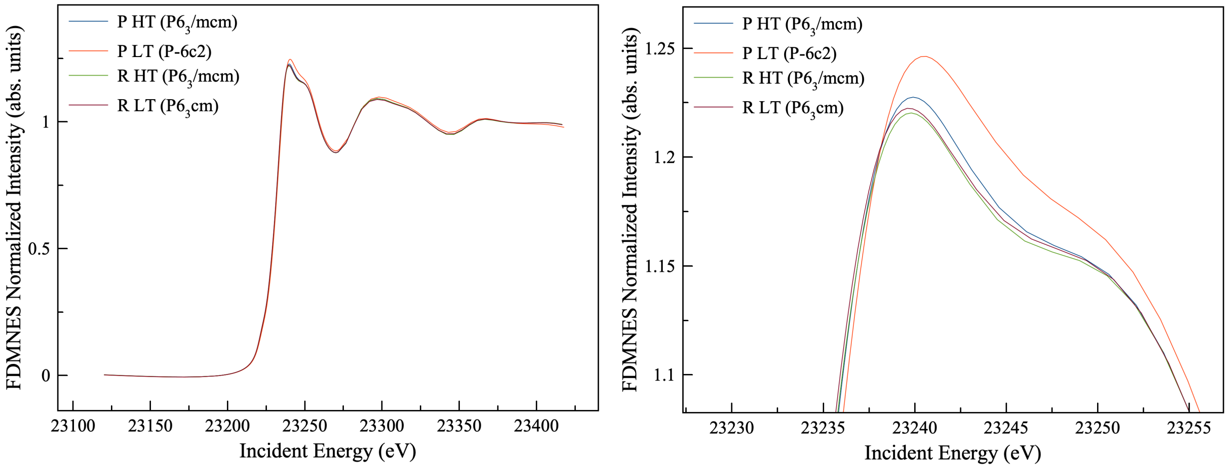

(c) FDMNES (SO), full data range. (d) FDMNES (SO), white line features.

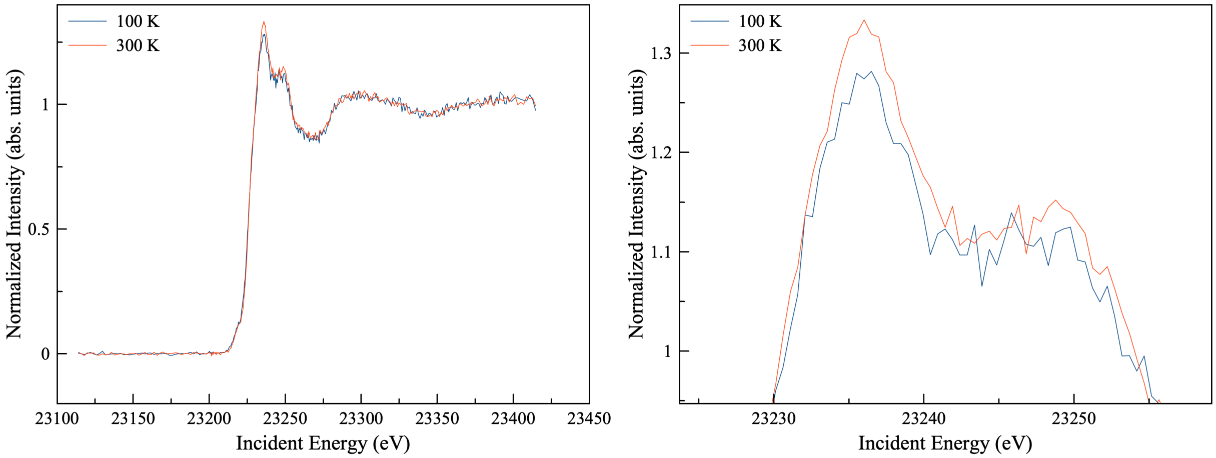

(e) HERFD-XAS, full data range. (f) HERFD-XAS, white line features.

Figure 6.7: Comparison between FDMNES Models, with (SO) and without (No SO) spin-orbit coupling, for Proposed (P) and Refined (R) Structures.

may be important in the $Pb_3Rh_7O_{15}$ system.

In summary, our local electronic environment analysis confirmed the mixed-valence nature of $Pb_3Rh_7O_{15}$ at temperatures above T_V through HERFD-XAS spectra comparison with $Rh^{3+]}$ and Rh^{4+} reference samples and showed no evidence of a structural transition at T_V. FDMNES simulations show XAS spectra calculated from the $P6_3cm$ structure resemble our experimental low-temperature data more closely than spectra based on the proposed $P\overline{6}c2$ structure, supporting our conclusions from our single crystal XRD refinement.

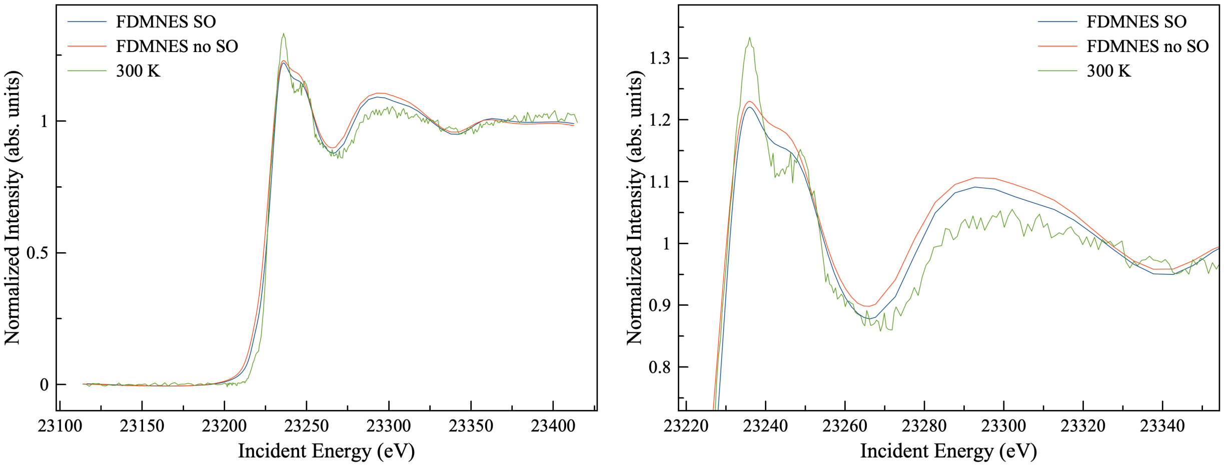

(a) HT, full data range.

(b) HT, zoomed-in view.

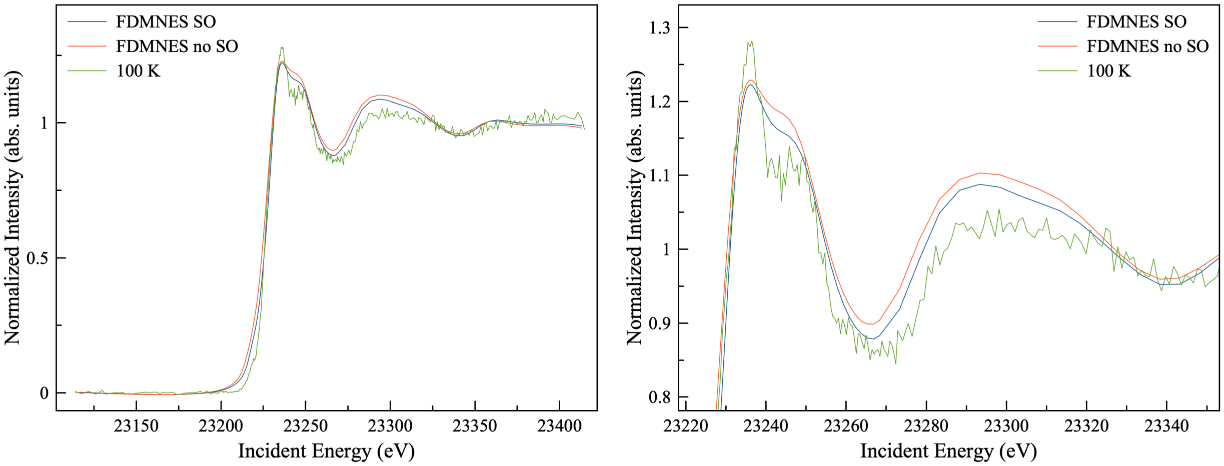

(c) LT, full data range.

(d) LT, zoomed-in view.

Figure 6.8: Comparison of FDMNES models, with (SO) and without (No SO) spin-orbit coupling, with HERFD-XAS spectra for structures above and below T_V.

Chapter 7

Conclusion

This work investigated the conductor-to-insulator transition in $Pb_3Rh_7O_{15}$. From bulk measurements, the existence of this transition has been known for over 40 years; however, the underlying mechanism responsible for this behaviour remains to be experimentally proven. The nominal valence of $Pb_3Rh_7O_{15}$ indicates a mixed Rh^{3+} and Rh^{4+} oxidation state of the Rh cations, which we confirmed using XAS. Hence, a logical first hypothesis for the driving mechanism in this system is charge ordering, which has been observed to cause conductor-to-insulator transitions in other mixed-valent systems, known as Verwey compounds.

In $Pb_3Rh_7O_{15}$, it has been proposed that charge ordering occurs on a specific crystallographic site below the transition temperature T_V. To stabilize this phase, the conductor-to-insulator transition is accompanied by a structural distortion, characterized by a change in space group from the established high-temperature $P6_3/mcm$ to a proposed low-temperature $P\bar{6}c2$ structure. Results from our average structural analysis using single-crystal XRD confirm the presence of a structural transition; however, the low-temperature space group was determined to be $P6_3cm$. Our subsequent geometrical analysis (based on space group symmetry) and bond valence sum (BVS) analysis (based on refined bond lengths) show that the mixed-valent nature of the crystallographic site persists below T_V, contradicting the proposed charge ordering scheme. Following these measurements, we expanded our search for charge order in $Pb_3Rh_7O_{15}$ by considering local ordering and short-range correlations in our local structural analysis, which involved searching for diffuse scattering through HDRM and 3D-Δ PDF analyses. Results showed no evidence of temperature-dependent variations related to the transition temperature. We then investigated the average local electronic environment of the Rh cations through qualitative RXES and quantitative HERFD-XAS analyses. Comparisons of raw data and extracted fit parameters across different temperature datasets revealed no systematic differences. FDMNES models based on our refined structures predicted no significant differences between the high and low-temperature XAS spectra. Meanwhile, simulated spectra based on the proposed structures predicted differences that were not observed in the experimental data. Therefore, consolidating all experimental techniques described in this work, results consistently show no evidence of charge order in $Pb_3Rh_7O_{15}$, challenging its proposed classification as a Verwey compound.

Discrepancies between FDMNES and HERFD-XAS spectra revealed that spin-orbit coupling should be considered in FDMNES calculations and suggested the presence of additional interactions in the system that could contribute to the driving mechanism of the studied transition in $Pb_3Rh_7O_{15}$. These results raise new questions, which can guide future work related to this compound: What other competing interactions are present in the system, and how does the established structural transition influence these interactions and the observed conductor-to-insulator transition? Future experiments could include Rh L-edge XAS to directly probe valence electrons, potential hybridization, and spin-orbit coupling effects, as well as O K-edge XAS to investigate *pd*-hybridization effects and structural distortions of the O ligands in the octahedral cage surrounding the Rh cations. Moreover, results from L-edge RIXS measurements could provide information about changes in the insulating gap and crystal field splitting.

References

[1] P. P. Edwards, R. L. Johnston, C. N. R. Rao, D. P. Tunstall, and F. Hensel. "The Metal-Insulator Transition: A Perspective". In: *Philosophical Transactions: Mathematical, Physical and Engineering Sciences* 356.1735 (1998), pp. 5–22. ISSN: 1364503X, 14712962. URL: http://www.jstor.org/stable/54951.

[2] M. Imada, A. Fujimori, and Y. Tokura. "Metal-insulator transitions". In: *Rev. Mod. Phys.* 70 (4 Oct. 1998), pp. 1039–1263. DOI: 10.1103/RevModPhys.70.1039. URL: https://link.aps.org/doi/10.1103/RevModPhys.70.1039.

[3] F. Gebhard. *The Mott Metal-Insulator Transition Models and Methods.* 3rd ed. Springer, 1962.

[4] J. García and G. Subías. "The Verwey Transition - a new perspective". In: *J. Phys.: Condens. Matter* 16 (Feb. 2004), R145–R178. DOI: 10.1088/0953-8984/16/7/R01. URL: https://iopscience.iop.org/article/10.1088/0953-8984/16/7/R01.

[5] S. Streltsov and D. Khomskii. "Orbital physics in compounds of transition metals: new trends". In: *Physics-Uspekhi* 60 (Aug. 2017). DOI: 10.3367/UFNe.2017.08.038196.

[6] G. Jackeli and G. Khaliullin. "Mott Insulators in the Strong Spin-Orbit Coupling Limit: From Heisenberg to a Quantum Compass and Kitaev Models". In: *Phys. Rev. Lett.* 102 (1 Jan. 2009), p. 017205. DOI: 10.1103/PhysRevLett.102.017205. URL: https://link.aps.org/doi/10.1103/PhysRevLett.102.017205.

[7] V. I. Anisimov, I. S. Elfimov, N. Hamada, and K. Terakura. "Charge-ordered insulating state of Fe_3O_4 from first-principles electronic structure calculations". In: *Phys. Rev. B* 54 (7 Aug. 1996), pp. 4387–4390. DOI: 10.1103/PhysRevB.54.4387. URL: https://link.aps.org/doi/10.1103/PhysRevB.54.4387.

[8] J. Zaanen, G. A. Sawatzky, and J. W. Allen. "Band gaps and electronic structure of transition-metal compounds". In: *Phys. Rev. Lett.* 55 (4 July 1985), pp. 418–421. DOI: 10.1103/PhysRevLett.55.418. URL: https://link.aps.org/doi/10.1103/PhysRevLett.55.418.

[9] J. H. de Boer and E. J. W. Verwey. "Semi-conductors with partially and with completely filled 3d-lattice bands". In: *Proceedings of the Physical Society* 49.4S (Aug. 1937), p. 59. DOI: 10.1088/0959-5309/49/4S/307. URL: https://dx.doi.org/10.1088/0959-5309/49/4S/307.

[10] F. Lechermann, W. Körner, D. F. Urban, and C. Elsässer. "Interplay of charge-transfer and Mott-Hubbard physics approached by an efficient combination of self-interaction correction and dynamical mean-field theory". In: *Phys. Rev. B* 100 (11 Sept. 2019), p. 115125. DOI: 10.1103/PhysRevB.100.115125. URL: https://link.aps.org/doi/10.1103/PhysRevB.100.115125.

[11] D. I. Khomskii. "Mott–Hubbard vs charge-transfer insulators". In: *Transition Metal Compounds*. Cambridge University Press, 2014, pp. 94–119.

[12] E. Verwey and P. Haayman. "Electronic conductivity and transition point of magnetite ("Fe3O4")". In: *Physica* 8.9 (1941), pp. 979–987. ISSN: 0031-8914. DOI: https://doi.org/10.1016/S0031-8914(41)80005-6. URL: https://www.sciencedirect.com/science/article/pii/S0031891441800056.

[13] M. Senn, J. Wright, and J. Attfield. "Charge Order and Three-Site Distortions in the Verwey Structure of Magnetite". In: *Nature* 481 (Dec. 2011), pp. 173–6. DOI: 10.1038/nature10704. URL: https://www.nature.com/articles/nature10704.

[14] H. Mizoguchi, A. Ramirez, T. Siegrist, L. Zakharov, A. Sleight, and M. Subramanian. "Possible Verwey-type transition in $Pb_3Rh_7O_{15}$". In: *Chemistry of Materials* 21 (2009). Inorganic Crystal Structure Database (ICSD 420582), pp. 2300–2305. DOI: 10.1021/cm900697s.

[15] G. Perversi, J. Cumby, E. Pachoud, J. P. Wright, and J. P. Attfield. "The Verwey structure of a natural magnetite". In: *Chem. Commun.* 52 (27 2016), pp. 4864–4867. DOI: 10.1039/C5CC10495E. URL: http://dx.doi.org/10.1039/C5CC10495E.

[16] N. W. Ashcroft and N. D. Mermin. *Solid State Physics*. Holt-Saunders, 1976.

[17] D. W. Koon and T. G. Castner. "Hall effect near the metal-insulator transition". In: *Phys. Rev. B* 41 (17 June 1990), pp. 12054–12070. DOI: 10.1103/PhysRevB.41.12054. URL: https://link.aps.org/doi/10.1103/PhysRevB.41.12054.

[18] S. Sciver. "Low-Temperature Materials Properties". In: Springer, Nov. 2012, pp. 17–58. ISBN: 978-1-4419-9978-8. DOI: 10.1007/978-1-4419-9979-5_2.

[19] G. Prunet, F. Pawula, G. Fleury, E. Cloutet, A. Robinson, G. Hadziioannou, and A. Pakdel. "A review on conductive polymers and their hybrids for flexible and wearable thermoelectric applications". In: *Materials Today Physics* 18 (2021), p. 100402. ISSN: 2542-5293. DOI: https://doi.org/10.1016/j.mtphys.2021.100402. URL: https://www.sciencedirect.com/science/article/pii/S2542529321000638.

[20] E. F. Westrum and F. Grønvold. "Magnetite (Fe3O4) Heat capacity and thermodynamic properties from 5 to 350 K, low-temperature transition". In: *The Journal of Chemical Thermodynamics* 1.6 (1969), pp. 543–557. ISSN: 0021-9614. DOI: https://doi.org/10.1016/0021-9614(69)90015-9. URL: https://www.sciencedirect.com/science/article/pii/0021961469900159.

[21] Y. Yu, Y. Cui, J. He, W. Mao, and J. Chen. "Metal-to-insulator transitions in 3d-band correlated oxides containing Fe compositions". In: *International Journal of Minerals, Metallurgy and Materials* 31.1 (2024), pp. 48–59.

[22] S. V. Ovsyannikov et al. "A Room-Temperature Verwey-type Transition in Iron Oxide, Fe5O6". In: *Angewandte Chemie International Edition* 59.14 (2020), pp. 5632–5636. DOI: https://doi.org/10.1002/anie.201914988. eprint: https://onlinelibrary.wiley.com/doi/pdf/10.1002/anie.201914988. URL: https://onlinelibrary.wiley.com/doi/abs/10.1002/anie.201914988.

[23] M. Tyunina, M. Savinov, O. Pacherova, et al. "Small-polaron transport in perovskite nickelates". In: *Scientific Reports* 13 (Apr. 2023), p. 12493. DOI: 10.1038/s41598-023-39821-z. URL: https://doi.org/10.1038/s41598-023-39821-z.

[24] A. T. Burkov, T. Nakama, M. Hedo, K. Shintani, K. Yagasaki, N. Matsumoto, and S. Nagata. "Anomalous resistivity and thermopower of the spinel-type compounds $CuIr_2S_4$ and $CuIr_2Se_4$". In: *Phys. Rev. B* 61 (15 Apr. 2000), pp. 10049–10056. DOI: 10.1103/PhysRevB.61.10049. URL: https://link.aps.org/doi/10.1103/PhysRevB.61.10049.

[25] J. L. Manson. "The Chemical Bond in Inorganic Chemistry: the Valence Bond Model By I. David Brown (McMaster University). Oxford University Press: New York. 2002. ISBN 0-19-850870-0." In: *Journal of the American Chemical Society* 124.42 (2002), pp. 12633–12633. DOI: 10.1021/ja025226b. eprint: https://doi.org/10.1021/ja025226b. URL: https://doi.org/10.1021/ja025226b.

[26] A. Zahid, A. Iftikhar, K. Banaras, and K. Imad. "Robust Half-Metallicity and Magnetic Properties of Cubic Perovskite CaFeO3". In: *Chinese Physics Letters* 30.4 (Apr. 2013), p. 047504. DOI: 10.1088/0256-307X/30/4/047504.

[27] C. Piamonteze, H. C. N. Tolentino, A. Y. Ramos, N. E. Massa, J. A. Alonso, M. J. Martínez-Lope, and M. T. Casais. "Short-range charge order in $R\mathrm{NiO}_3$ perovskites (R = Pr, Nd, Eu, Y) probed by x-ray-absorption spectroscopy". In: *Phys. Rev. B* 71 (1 Jan. 2005), p. 012104. DOI: 10.1103/PhysRevB.71.012104. URL: https://link.aps.org/doi/10.1103/PhysRevB.71.012104.

[28] H. Sato, T. Matsumoto, K. Maeda, Y. Taguchi, N. Kawamura, and H. Ishibashi. "Metal-insulator transition in $CuIr_2S_4$ observed by Cu $K\alpha$ resonant x-ray emission spectroscopy". In: *Phys. Rev. B* 106 (15 Oct. 2022), p. 155151. DOI: 10.1103/PhysRevB.106.155151. URL: https://link.aps.org/doi/10.1103/PhysRevB.106.155151.

[29] A. Boonstra and C. Mutsaers. "Small values of the temperature coefficient of resistance in lead rhodate thick films ascribed to a compensation mechanism". In: *Thin Solid Films* 51.3 (1978), pp. 287–296. ISSN: 0040-6090. DOI: https://doi.org/10.1016/0040-6090(78)90290-0. URL: https://www.sciencedirect.com/science/article/pii/0040609078902900.

[30] H. Mizoguchi, A. P. Ramirez, T. Siegrist, L. N. Zakharov, A. W. Sleight, and M. A. Subramanian. "Possible Verwey-Type Transition in $Pb_3Rh_7O_{15}$". In: *Chemistry of Materials* 21.11 (2009), pp. 2300–2305. DOI: 10.1021/cm900697s. eprint: https://doi.org/10.1021/cm900697s. URL: https://doi.org/10.1021/cm900697s.

[31] Y. Li, Z. Sun, J.-W. Cai, J.-P. Sun, B.-S. Wang, Z.-Y. Zhao, Y. Uwatoko, J.-Q. Yan, and J.-G. Cheng. "Pressure-Induced Charge-Order Melting and Reentrant Charge Carrier Localization in the Mixed-Valent Pb3Rh7O15*". In: *Chinese Physics Letters* 34.8 (July 2017), p. 087201. DOI: 10.1088/0256-307X/34/8/087201. URL: https://dx.doi.org/10.1088/0256-307X/34/8/087201.

[32] H. Mizoguchi, W. Marshall, A. Ramirez, A. Sleight, and M. Subramanian. "Partial charge ordering in the mixed-valent compound (Bi6O5)Rh83+Rh44+O24". In: *Journal of Solid State Chemistry* 180.12 (2007), pp. 3463–3468. ISSN: 0022-4596. DOI: https://doi.org/10.1016/j.jssc.2007.09.031. URL: https://www.sciencedirect.com/science/article/pii/S0022459607004082.

[33] H. Mizoguchi, A. Ramirez, T. Siegrist, L. Zakharov, A. Sleight, and M. Subramanian. "Possible Verwey-type transition in $Pb_3Rh_7O_{15}$". In: *Chemistry of Materials* 21 (2009). Inorganic Crystal Structure Database (ICSD 420582), pp. 2300–2305. DOI: 10.1021/cm900697s.

[34] S. J. L. Billinge. "The rise of the X-ray atomic pair distribution function method: a series of fortunate events". In: *Philosophical Transactions of the Royal Society A: Mathematical, Physical and Engineering Sciences* 377.2147 (2019). DOI: 10.1098/rsta.2018.0413. eprint: https://royalsocietypublishing.org/doi/pdf/10.1098/rsta.2018.0413. URL: https://royalsocietypublishing.org/doi/abs/10.1098/rsta.2018.0413.

[35] G. Sheldrick. "SHELXT - Integrated space-group and crystal-structure determination". In: *Acta Crystallographica Section A* 71 (2015), pp. 3–8.

[36] G. Sheldrick. "A short history of SHELX". In: *Acta Crystallographica Section A* 64 (2008), pp. 112–122.

[37] O. Dolomanov, L. Bourhis, R. Gildea, J. Howard, and H. Puschmann. "OLEX2: A complete structure solution, refinement and analysis program". In: *Journal of Applied Crystallography* 42 (2009), pp. 339–341.

[38] N. E. Brese and M. O'Keeffe. "Bond-valence parameters for solids". In: *Acta Crystallographica Section B* 47.2 (Apr. 1991), pp. 192–197. DOI: 10.1107/S0108768190011041. URL: https://doi.org/10.1107/S0108768190011041.

[39] I. D. Brown and D. Altermatt. "Bond-valence parameters obtained from a systematic analysis of the Inorganic Crystal Structure Database". In: *Acta Crystallographica Section B* 41.4 (Aug. 1985), pp. 244–247. DOI: 10.1107/S0108768185002063. URL: https://doi.org/10.1107/S0108768185002063.

[40] T. R. Welberry and B. D. Butler. "Diffuse X-ray Scattering from Disordered Crystals". In: *Chemical Reviews* 95.7 (1995), pp. 2369–2403. DOI: 10.1021/cr00039a005. eprint: https://doi.org/10.1021/cr00039a005. URL: https://doi.org/10.1021/cr00039a005.

[41] K. E. Nygren, D. C. Pagan, J. P. C. Ruff, E. Arenholz, and J. D. Brock. "Cartography in 7-Dimensions at CHESS: Mapping of Structure in Real Space, Reciprocal Space, and Time Using High-Energy X-rays". In: *Synchrotron Radiation News* 33.6 (2020), pp. 11–16. DOI: 10.1080/08940886.2020.1841491. eprint: https://doi.org/10.1080/08940886.2020.1841491. URL: https://doi.org/10.1080/08940886.2020.1841491.

[42] T. Weber and A. Simonov. “The three-dimensional pair distribution function analysis of disordered single crystals: Basic concepts”. In: *Zeitschrift für Kristallographie* 227 (May 2012), pp. 238–247. DOI: 10.1524/zkri.2012.1504.

[43] M. R. Gogate and R. J. Davis. “X-ray Absorption Spectroscopy of an Fe-Promoted Rh/TiO2 Catalyst for Synthesis of Ethanol from Synthesis Gas”. In: *ChemCatChem* 1.2 (2009), pp. 295–303. DOI: https://doi.org/10.1002/cctc.200900104. eprint: https://chemistry-europe.onlinelibrary.wiley.com/doi/pdf/10.1002/cctc.200900104. URL: https://chemistry-europe.onlinelibrary.wiley.com/doi/abs/10.1002/cctc.200900104.

[44] B. M. “HERFD-XAS and valence-to-core-XES: new tools to push the limits in research with hard X-rays?” In: *Phys. Chem. Chem. Phys.,* 16 (2014), pp. 13827–13837. DOI: 10.1039/C4CP00904E.

[45] J. A. BEARDEN. “X-Ray Wavelengths”. In: *Rev. Mod. Phys.* 39 (1 Jan. 1967), pp. 78–124. DOI: 10.1103/RevModPhys.39.78. URL: https://link.aps.org/doi/10.1103/RevModPhys.39.78.

[46] A. Y. R. O. Bunău and Y. Jolya. “The FDMNES code”. In: *International Tables for Crystallography* I.6.6 (2024), pp. 752–757. DOI: https://doi.org/10.1107/S1574870720003304. URL: https://onlinelibrary.wiley.com/iucr/itc/Ia/qx0012/.